

การเตรียมและการชิมของออกซิเจนผ่านเมมเบรนเพอร์อฟสไกต์เฟสคู่



นางสาวอิสราวดี ทิพย์ดวง

สถาบันวิทยบริการ

จุฬาลงกรณ์มหาวิทยาลัย

วิทยานิพนธ์นี้เป็นส่วนหนึ่งของการศึกษาตามหลักสูตรปริญญาวิทยาศาสตรมหาบัณฑิต

สาขาปิโตรเคมีและวิทยาศาสตร์พอลิเมอร์

คณะวิทยาศาสตร์ จุฬาลงกรณ์มหาวิทยาลัย

ปีการศึกษา 2548

ISBN 974-14-1996-1

ลิขสิทธิ์ของจุฬาลงกรณ์มหาวิทยาลัย

PREPARATION AND OXYGEN PERMEATION OF DUAL-PHASE  
PEROVSKITE MEMBRANES



Miss Itsarawadee Thipdaung

สถาบันวิทยบริการ  
จุฬาลงกรณ์มหาวิทยาลัย

A Thesis Submitted in Partial Fulfillment of the Requirements  
for the Degree of Master of Science Program in Petrochemistry and Polymer Science

Faculty of Science  
Chulalongkorn University

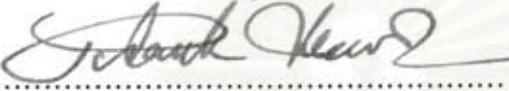
Academic Year 2005

ISBN 974-14-1996-1

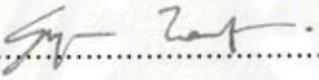
Thesis Title                    PREPARATION AND OXYGEN PERMEATION OF  
DUAL-PHASE PEROVSKITE MEMBRANES  
By                                    Miss Itsarawadee Thipdaung  
Field of Study                    Petrochemistry and Polymer Science  
Thesis Advisor                    Oravan Saganruang, Ph.D.


---

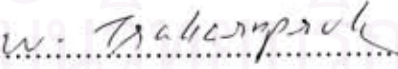
Accepted by the Faculty of Science, Chulalongkorn University in  
Partial Fulfillment of the Requirements for the Master's Degree


  
..... Dean of the Faculty of Science  
(Professor Piamsak Menasveta, Ph.D.)

THESIS COMMITTEE

  
..... Chairman  
(Associate Professor Supawan Tantayanon, Ph.D.)

  
..... Thesis Advisor  
(Oravan Saganruang, Ph.D.)

  
..... Member  
(Associate Professor Wimonrat Trakarnpruk, Ph.D.)

  
..... Member  
(Assistant Professor Warinthorn Chavasiri, Ph.D.)

อิสราวดิ ทิพย์ดวง : การเตรียมและการซึมของออกซิเจนผ่านเมมเบรนเพอโรฟสไกต์เฟสคู่  
(PREPARATION AND OXYGEN PERMEATION OF DUAL-PHASE  
PEROVSKITE MEMBRANES) อาจารย์ที่ปรึกษา : อ.ดร. อรวรรณ สงวนเรือง  
80 หน้า. ISBN 974-14-1996-1

สังเคราะห์สารเพอโรฟสไกต์ออกไซด์ชนิด  $\text{La}_{0.3}\text{Sr}_{0.7}\text{Al}_{0.2}\text{Fe}_{0.8}\text{O}_{3-\delta}$  (LSAF),  $\text{Ba}_{0.5}\text{Sr}_{0.5}\text{Co}_{0.8}\text{Fe}_{0.2}\text{O}_{3-\delta}$  (BSCF),  $\text{La}_{0.6}\text{Sr}_{0.4}\text{Co}_{0.8}\text{Fe}_{0.2}\text{O}_{3-\delta}$  (LSCF) และ  $\text{La}_{0.6}\text{Sr}_{0.4}\text{CoO}_{3-\delta}$  (LSC) ด้วยวิธีซิเทรตประยุกต์และวิธีเตรียมแบบสารละลาย ตรวจสอบโครงสร้างผลึกของเพอโรฟสไกต์ด้วยเทคนิคการเลี้ยวเบนของรังสีเอ็กซ์ จากนั้นเตรียมเมมเบรนเพอโรฟสไกต์เฟสคู่ของ LSAF-BSCF, LSAF-LSCF และ LSAF-LSC โดยการผสม LSAF กับ BSCF, LSCF หรือ LSC ตามลำดับ ด้วยอัตราส่วน 12:1-12:4 โดยน้ำหนัก ทำการเผาซินเทอร์ที่อุณหภูมิ 1,200-1,400 องศาเซลเซียสเป็นเวลา 5-10 ชั่วโมง การวิเคราะห์ด้วย XRD (X-ray diffraction) แสดงการเกิดเฟสที่เป็นเพอโรฟสไกต์แบบคิวบิก ตรวจสอบอิทธิพลของเวลาและอุณหภูมิในการเผาซินเทอร์รวมถึงปริมาณของ BSCF, LSCF และ LSC ที่มีต่อพื้นผิวด้วยเทคนิค SEM (Scanning Electron Microscopy) เมมเบรนเพอโรฟสไกต์เฟสคู่ที่ผ่านการเผาซินเทอร์ที่ 1,400 องศาเซลเซียส เป็นเวลา 6 ชั่วโมง มีขนาดอนุภาคใหญ่กว่าการซินเทอร์ที่ภาวะอื่น ๆ เพอโรฟสไกต์เฟสคู่ทุกชนิดมีขนาดอนุภาคใหญ่ที่สุดเมื่อเพอโรฟสไกต์เฟสคู่มีอัตราส่วน 12:4 ศึกษาสมบัติการดูดซับแก๊สออกซิเจนของสารประกอบเพอโรฟสไกต์เฟสคู่โดยใช้เทคนิค TGA (Thermogravimetric Analysis) และ  $\text{O}_2$ -TPD (Temperature Program Desorption of Oxygen) ผลของ TGA แสดงว่าเพอโรฟสไกต์เฟสคู่ของ LSAF-LSC ที่มีอัตราส่วน 12:4 โดยน้ำหนัก มีปริมาณการดูดซับแก๊สออกซิเจนสูงกว่า LSAF, เพอโรฟสไกต์เฟสคู่ชนิด LSAF-BSCF และ LSAF-LSCF จากผลของ  $\text{O}_2$ -TPD พบว่าปริมาณรวมของออกซิเจนที่หลุดจากโครงสร้างของ LSAF-BSCF มีค่าน้อยกว่า LSAF ขณะที่ LSAF-LSCF อัตราส่วน 12:2 และ LSAF-LSC อัตราส่วน 12:4 ปริมาณการดูดซับแก๊สออกซิเจนสูงกว่าอัตราส่วนอื่น ๆ ดังนั้น อัตราเร็วของการซึมผ่านของออกซิเจนเพิ่มขึ้นได้โดยการผสม LSAF กับ LSCF หรือ LSC

สาขาวิชา...มิโทเรเคมีและวิทยาศาสตร์พอลิเมอร์... ลายมือชื่อนิสิต... อิสราวดิ ทิพย์ดวง  
ปีการศึกษา...2548... ลายมือชื่ออาจารย์ที่ปรึกษา... อรวรรณ สงวนเรือง

##4772575123 : MAJOR PETROCHEMISTRY AND POLYMER SCIENCE  
 KEYWORD: PEROVSKITE / DUAL-PHASE MEMBRANE

ITSARAWADEE THIPDAUNG : PREPARATION AND OXYGEN  
 PERMEATION OF DUAL-PHASE PEROVSKITE MEMBRANES.  
 THESIS ADVISOR: ORAVAN SANGUANRUANG, Ph.D., 80 pp. ISBN  
 974-14-1996-1

The perovskite oxides of  $\text{La}_{0.3}\text{Sr}_{0.7}\text{Al}_{0.2}\text{Fe}_{0.8}\text{O}_{3-\delta}$  (LSAF),  $\text{Ba}_{0.5}\text{Sr}_{0.5}\text{Co}_{0.8}\text{Fe}_{0.2}\text{O}_{3-\delta}$  (BSCF),  $\text{La}_{0.6}\text{Sr}_{0.4}\text{Co}_{0.8}\text{Fe}_{0.2}\text{O}_{3-\delta}$  (LSCF) and  $\text{La}_{0.6}\text{Sr}_{0.4}\text{CoO}_{3-\delta}$  (LSC) were synthesized by a modified citrate method and solution method. The crystal structure of single-phase perovskite powder was characterized by X-ray diffraction (XRD). LSAF-BSCF, LSAF-LSCF and LSAF-LSC dual-phase membranes were prepared by mixing the powder of LSAF with BSCF, LSCF and LSC, respectively with ratio 12:1-12:4 by weight. The dual-phase membranes were sintered around 1,200-1,400°C for 5-10 hours. The XRD analysis showed the formation of cubic perovskite phase. Influence of sintering time, sintering temperature and amount of BSCF, LSCF and LSC on the morphology of dual-phase membranes were examined by using scanning electron microscopy (SEM). The result exhibited that the grain size of the dual-phase membranes after sintering at 1,400°C for 6 hours is larger than that of the other conditions. All dual-phase perovskites with ratio 12:4 had the largest grain size. The oxygen desorption property of dual-phase perovskite was investigated by thermogravimetric analysis (TGA) and temperature program desorption of oxygen ( $\text{O}_2$ -TPD). TGA results demonstrated that the amount of oxygen desorption of LSAF-LSC dual-phase with ratio 12:4 by weight had higher value compared to those of LSAF and the other ratios of dual-phase of LSAF-BSCF and LSAF-LSCF. The  $\text{O}_2$ -TPD data revealed the total amount of oxygen liberated from composite LSAF-BSCF is less than the pure phase of LSAF. The LSAF-LSCF with ratio 12:2 and LSAF-LSC with ratio 12:4 showed the high oxygen desorption than those of the other ratios. Therefore, the oxygen permeation flux of LSAF could be increased by mixing LSAF with LSCF and LSC.

Field of study Petrochemistry and Polymer science Student's signature Itsarawadee Thipdaung  
 Academic year.....2005..... Advisor's signature Oravan Sanguanruang

## ACKNOWLEDGEMENTS

The author is deeply appreciated to her family for their love, support and encouragement during her the whole period of her study.

The author wishes to express greatest gratitude to her advisor, Dr.Oravan Sanguanruang, for her valuable advice, kind assistance, and encouragement throughout the course of this research. In addition, the author would like to special thank to Associate Professor Dr. Supawan Tantayanon, Associate Professor Dr. Wimonrat Trakarnpruk, and Assistant Professor Dr. Warinthorn Chavasiri for serving as the chairman and members of her thesis committee, respectively, for their valuable suggestions and comments.

Appreciation is extended to the Materials Chemistry and Catalysis Research Unit (MATCAT) for financial support during study and provision of experimental facilities. Acknowledgement is also extended to Program of Petrochemistry and Polymer Science, Department of Chemistry, Faculty of Science and Graduate School, Chulalongkorn University for granting financial support to fulfill this study.

This thesis could not complete without generous help of the staff members of the Materials Chemistry and Catalysis Research Unit. Special thank is forwarded to my best friends for their love, assistance and encouragement. Without them, the author would have never been able to achieve this goal.

# CONTENTS

	<b>PAGE</b>
<b>ABSTRACT (IN THAI)</b> .....	iv
<b>ABSTRACT (IN ENGLISH)</b> .....	v
<b>ACKNOWLEDGEMENT</b> .....	vi
<b>CONTENTS</b> .....	vii
<b>LIST OF FIGURES</b> .....	xi
<b>LIST OF SCHEMES</b> .....	xiv
<b>LIST OF TABLES</b> .....	xv
<b>LIST OF ABBREVIATIONS</b> .....	xvi
<b>CHAPTER I INTRODUCTION</b> .....	1
1.1 Background.....	1
1.2 Literature review.....	3
1.3 The objectives of the thesis.....	9
<b>CHAPTER II THEORY</b> .....	10
2.1 Structure of perovskites .....	10
2.1.1 Crystal structure .....	10
2.1.2 Tolerance factors in perovskites .....	11
2.1.3 Nonstoichiometry in perovskites .....	12
2.2 Physical properties.....	13
2.2.1 Mixed ionic-electronic conductors.....	13
2.2.2 Magnetic properties .....	15
2.3 Dense perovskite membranes for oxygen separation.....	15
2.3.1 Perovskite membrane concepts.....	15
2.3.2 Oxygen permeation through a mixed-conducting membrane.....	17
2.4 Perovskite synthesis.....	19
2.4.1 Gas phase reaction.....	20
2.4.2 Solid-state reaction.....	20

## CONTENTS (Cont.)

	PAGE
2.4.3 Solution reaction.....	20
2.5 Perovskite membrane preparation.....	21
2.5.1 Solution reaction synthesis of perovskites.....	21
2.5.2 Powder sizing.....	23
2.5.3 Powder compacting by uniaxial pressing.....	24
2.5.4 Sintering.....	24
<b>CHAPTER III EXPERIMENT.....</b>	<b>27</b>
3.1 Chemicals.....	27
3.2 Synthesis of LSAF3728 and BSCF5582 perovskite powders by modified citrate method.....	28
3.3 Synthesis of LSCF6482 and LSC64 perovskite powders by solution method.....	29
3.4 Preparation of dual-phase perovskite.....	30
3.5 Perovskite membrane preparation.....	30
3.6 The sintering of the perovskite oxides.....	31
3.7 Characterization of the perovskite oxides.....	32
3.7.1 X-ray diffractometry (XRD).....	32
3.7.2 Scanning electron microscopy (SEM) and Energy Dispersive X-ray (EDX) technique .....	32
3.7.3 Thermogravimetric analysis (TGA).....	32
3.7.4 Temperature-programmed desorption (TPD).....	33
<b>CHAPTER IV RESULTS AND DISCUSSIONS.....</b>	<b>34</b>
4.1 Perovskite powder.....	34
4.1.1 Synthesis of LSAF3728 and BSCF5582 perovskite powders by modified citrate method.....	34
4.1.2 Synthesis of LSCF6482 and LSC64 perovskite powders by solution method.....	36
4.2 Characterization of dual-phase perovskite compounds.....	38



## CONTENTS (Cont.)

	<b>PAGE</b>
4.2.1 X-ray diffraction (XRD)	38
4.2.1.1 Phase formation of dual-phase perovskite powder..	38
A. The LSAF-BSCF dual-phase perovskite powder	38
B. The LSAF-LSCF dual-phase perovskite powder	40
C. The LSAF-LSC dual-phase perovskite powder..	42
4.2.1.2 The effect of calcination and sintering on dual-phase perovskite membranes.....	44
A. The variation of BSCF5582 contents in LSAF-BSCF dual-phase perovskite.....	44
B. The variation of LSCF6482 contents in LSAF-LSCF dual-phase perovskite.....	46
C. The variation of LSC64 contents in LSAF-LSC dual-phase perovskite.....	48
4.2.2 Scanning electron microscope (SEM).....	50
4.2.2.1 Effect of setting temperature program of sintering on the morphology of LSAF-BSCF dual-phase perovskite membranes.....	50
4.2.2.2 The influence of sintering time and temperature on morphology of dual-phase perovskite membranes..	52
A. The variation of BSCF5582 content in LSAF-BSCF dual-phase perovskite.....	52
B. The variation of LSCF6482 content in LSAF-LSCF dual-phase perovskite.....	53
C. The variation of LSC64 content in LSAF-LSC dual-phase perovskite.....	54
4.2.2.3 The effect of composition on morphology of dual-phase perovskite membranes.....	55
A. The variation of BSCF5582 contents on morphology of LSAF-BSCF dual-phase membranes.....	55

## CONTENTS (Cont.)

	<b>PAGE</b>
B. The variation of LSCF6482 contents on morphology of LSAF-LSCF dual-phase membranes.....	56
C. The variation of LSCF64 contents on morphology of LSAF-LSC dual-phase membranes.....	57
4.3 Oxygen desorption of perovskite compounds.....	58
4.3.1 Thermogravimetric analysis (TGA).....	58
4.3.1.1 The LSAF-BSCF dual-phase perovskite membranes.....	59
4.3.1.2 The LSAF-LSCF dual-phase perovskite membranes.....	60
4.3.1.3 The LSAF-LSC dual-phase perovskite membranes.....	62
4.3.2 Temperature-program desorption of oxygen (O <sub>2</sub> -TPD).....	63
4.3.2.1 The O <sub>2</sub> -TPD of the LSAF-BSCF dual-phase membranes.....	65
4.3.2.2 The O <sub>2</sub> -TPD of the LSAF-LSCF dual-phase membranes.....	66
4.3.2.3 The O <sub>2</sub> -TPD of the LSAF-LSC dual-phase membranes.....	67
<b>CHAPTER V CONCLUSIONS AND SUGGESTION.....</b>	<b>71</b>
5.1 Conclusions.....	71
5.2 Suggestion.....	72
<b>REFERENCES.....</b>	<b>73</b>
<b>APPENDIX.....</b>	<b>78</b>
<b>VITA.....</b>	<b>80</b>

## LIST OF FIGURES

	<b>PAGE</b>
Figure 2.1 ABO <sub>3</sub> ideal perovskite structure showing oxygen octahedron containing the B ion linked through corners to form a three-dimensional cubic lattice.....	11
Figure 2.2 The relationship between symmetry and ionic radii in the perovskite.....	11
Figure 2.3 Operating principle of a ceramic membrane reactor for the partial oxidation of methane to syngas.....	16
Figure 2.4 Perovskite membrane concepts.....	16
Figure 2.5 Schematic illustration of the profile in oxygen chemical potential $\mu_{O_2}$ across the MIEC membrane at steady-state conditions.....	17
Figure 2.6 The curve shows a possible Po <sub>2</sub> Profile over the membrane. A single prime indicates air side, double prime indicates permeate side.....	18
Figure 2.7 Mechanism of sintering.....	25
Figure 4.1 XRD patterns of LSAF3728 after calcined under conditions (a); a.1) 1000°C, 5 hr., a.2) 1000°C, 10 hr., a.3) 1100°C, 5 hr. a.4) 1200°C, 5 hr. and calcined under condition (b) 1000°C, 6 hr.....	35
Figure 4.2 XRD pattern of BSCF5582 perovskite powder.....	36
Figure 4.3 XRD pattern of LSCF6482 perovskite compound.....	37
Figure 4.4 XRD pattern of LSC64 perovskite compound.....	37
Figure 4.5 XRD patterns of pure LSAF3728, pure BSCF5582 and dual-phase perovskite powder of LSAF-BSCF with ratio 12:1 by weight....	39
Figure 4.6 The EDX pattern of LSAF-BSCF dual-phase membrane with ratio 12:1 by weight.....	40
Figure 4.7 XRD patterns of pure LSAF3728, pure LSCF6482 and dual-phase perovskite powder of LSAF-LSCF with ratio 12:1 by weight.....	41
Figure 4.8 The EDX pattern of LSAF-LSCF dual-phase membrane with ratio 12:1 by weight.....	42

	<b>PAGE</b>
Figure 4.9 XRD patterns of pure LSAF3728, pure LSC64 and dual-phase perovskite powder of LSAF-LSC with ratio 12:1 by weight .....	43
Figure 4.10 The EDX pattern of LSAF-BSCF dual-phase membrane with ratio 12:1 by weight.....	44
Figure 4.11 XRD patterns of LSAF-BSCF dual-phase perovskite membranes in various ratios after sintering at 1400°C, 6 hr.....	45
Figure 4.12 XRD patterns of LSAF-BSCF dual-phase perovskite membranes in various ratios after sintering at 1400°C, 6 hr.....	45
Figure 4.13 XRD patterns of LSAF-LSCF dual-phase perovskite membranes in various ratios after sintering at 1400°C, 6 hr.....	47
Figure 4.14 XRD patterns of LSAF-LSCF dual-phase perovskite membranes in various ratios after sintering at 1400°C, 6 hr.....	47
Figure 4.15 XRD patterns of LSAF-BSCF dual-phase perovskite membranes in various ratios after sintering at 1400°C, 6 hr.....	48
Figure 4.16 XRD patterns of LSAF-LSC dual-phase perovskite membranes in various ratios after sintering at 1400°C, 6 hr.....	49
Figure 4.17 SEM pictures of dual-phase membranes after set temperature program see Scheme 3.4 a); membrane sintered at (a) 1,200°C, 5 hr., (b) 1,300°C, 5 hr., (c) 1,300°C, 10 hr., set temperature program see Scheme 3.4 b); membrane sintered at (d) 1,300°C, 5 hr., (e) 1,300°C, 10 hr., and set temperature program see Scheme 3.4 c); membrane sintered at (f) 1,300°C, 6 hr.....	51
Figure 4.18 SEM pictures of LSAF-BSCF with ratio12:1 by weight after sintered at a) 1,300°C, 6 hr., b) 1,300°C, 12 hr., c) 1,300°C, 18 hr. and d) 1,400°C, 6 hr.....	52
Figure 4.19 SEM pictures of LSAF-LSCF with ratio12:1 by weight after sintered at a) 1,300°C, 6 hr., b) 1,300°C, 12 hr., c) 1,300°C, 18 hr. and d) 1,400°C, 6 hr.....	53
Figure 4.20 SEM pictures of LSAF-LSC with ratio12:1 by weight after sintered at a) 1,300°C, 6 hr., b) 1,300°C, 12 hr., c) 1,300°C, 18 hr. and d) 1,400°C, 6 hr.....	54

Figure 4.21 SEM pictures of LSAF-BSCF membranes with ratio a) 12:1, b) 12:2, c) 12:3 and d) 12:4 by weight.....	55
Figure 4.22 SEM pictures of LSAF-LSCF membranes with ratio a) 12:1, b) 12:2, c) 12:3 and d) 12:4 by weight.....	56
Figure 4.23 SEM pictures of LSAF-LSC membranes with ratio a) 12:1, b) 12:2, c) 12:3 and d) 12:4 by weight.....	57
Figure 4.24 TG-DSC profiles of LSAF3728 perovskite.....	58
Figure 4.25 TGA profiles of LSAF-BSCF dual-phase perovskite.....	59
Figure 4.26 TGA profiles of LSAF-LSCF dual-phase perovskite.....	61
Figure 4.27 TGA profiles of LSAF-LSC dual-phase perovskite.....	62
Figure 4.28 O <sub>2</sub> -TPD profiles of pure LSAF3728 perovskite.....	64
Figure 4.29 O <sub>2</sub> -TPD profiles of LSAF-BSCF dual-phase with various ratios...	65
Figure 4.30 O <sub>2</sub> -TPD profiles of LSAF-LSCF dual-phase with various ratios...	66
Figure 4.31 O <sub>2</sub> -TPD profiles of LSAF-LSC dual-phase with various ratios.....	67

## LIST OF SCHEMES

	<b>PAGE</b>
Scheme 3.1 The calcination conditions of LSAF3728 powder.....	28
Scheme 3.2 The calcination condition of BSCF5582 powder.....	29
Scheme 3.3 The calcination condition of LSCF6482 powder.....	30
Scheme 3.4 The sintering conditions of dual-phase membranes.....	31



สถาบันวิทยบริการ  
จุฬาลงกรณ์มหาวิทยาลัย

## LIST OF TABLES

		<b>PAGE</b>
Table 3.1	Chemical and reagents for synthesis of perovskite	27
Table 4.1	Lattice parameters of LSAF-BSCF dual-phase perovskite powder and pure phase of LSAF and BSCF.....	39
Table 4.2	Lattice parameters of LSAF-LSCF dual-phase perovskite powder and pure phase of LSCF and LSCF.....	41
Table 4.3	Lattice parameters of LSAF-LSC dual-phase perovskite powder and pure phase of LSAF and LSC.....	43
Table 4.4	Lattice parameter of LSAF-BSCF dual-phase perovskite.....	46
Table 4.5	Lattice parameter of LSAF-LSCF dual-phase perovskite.....	48
Table 4.6	Lattice parameter of LSAF-LSC dual-phase perovskite.....	49
Table 4.7	TGA data of LSAF-BSCF dual-phase perovskite.....	60
Table 4.8	TGA data of LSAF-LSCF dual-phase perovskite.....	61
Table 4.9	TGA data of LSAF-LSC dual-phase perovskite.....	63
Table 4.10	Amount of oxygen desorption for LSAF-BSCF dual-phase perovskite.....	66
Table 4.11	Amount of oxygen desorption for LSAF-LSCF dual-phase perovskite.....	67
Table 4.12	Amount of oxygen desorption for LSAF-LSC dual-phase perovskite.....	68
Table 4.13	Amount of oxygen desorption of dual-phase perovskites and LSAF3728.....	69

## LIST OF ABBRIVIATIONS

$\delta$	Non-stoichiometry of oxygen in mole formula
$\sigma_e$	Electronic conductivity
$\sigma_i$	Ionic conductivity
$\sigma_{ij}$	Partial conductivity of the jth-type ionic charge
$\sigma_{tot}$	Electrical conductivity
BSCF	Perovskite containing Ba, Sr, Co, and Fe
$^{\circ}\text{C}$	Degree celsius
EDX	Energy Dispersive X-ray
hr.	Hour
LSC	Perovskite containing La, Sr, and Co
LSAF	Perovskite containing La, Sr, Al, and Fe
LSCF	Perovskite containing La, Sr, Co, and Fe
MIECM	Mixed ionic-electronic conducting membrane
min	Minute
O <sub>2</sub> -TPD	Temperature program desorption of oxygen
P'O <sub>2</sub>	Partial pressure of oxygen at higher pressure
P''O <sub>2</sub>	Partial pressure of oxygen at lower pressure
POM	Partial Oxidation of Methane
$r_{Al^{3+}}$	Ionic radius of aluminium
$r_{Co^{3+}}$	Ionic radius of cobalt
$r_{Fe^{3+}}$	Ionic radius of iron
$r_{La^{3+}}$	Ionic radius of lanthanum
$r_{Sr^{2+}}$	Ionic radius of strontium
$r_{Ba^{2+}}$	Ionic radius of barium
SEM	Scanning Electron Microscope
t	Tolerance number
TEC	Thermal expansion coefficient
TGA	Thermogravimetric analysis
XRD	X-ray diffraction



# CHAPTER I

## INTRODUCTION

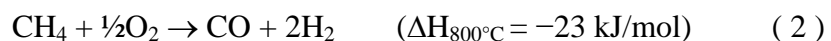
### 1.1 Background

Gas conversion to liquids is more important for both economic and environmental reasons. The quantity of gas reserves is huge and approximates the energy equivalent of the known crude oil reserves. Much of this natural gas is remote, located in a region where it is currently uneconomic to deliver to the market, and conversion to liquids opens economic alternatives. There are also significant environmental drivers for the conversion of natural gas [1]. Natural gas will be used a valuable raw material for several industrial processes, for example synthesis gas (syngas) manufacturing.

Syngas is a mixture of CO and H<sub>2</sub>. It is used as feedstock for many important industrial processes, such as methanol synthesis or the Fischer–Tropsch process [2]. Among the most important commercial routes of syngas manufacturing is the steam reforming of methane.



This process requires large amounts of energy and also suffers from limitations like poor selectivity for CO and a high H<sub>2</sub>/CO product ratio which is unsuitable for methanol synthesis. An alternative route is the partial oxidation of methane (POM) as presented in Equation 2, which is more favorable H<sub>2</sub> to CO ratio in the product gas as well as the mild exothermic of the reaction.



POM is necessary to use pure oxygen, rather than air in the steam forming process. The scheme is considered very attractive if the cost of the oxygen supply

can be reduced, so an expensive oxygen plant is needed. It was found that the investment cost in a cryogenic oxygen plant may constitute up to 45% of the total investment cost [3]. An alternative route that seems very promising is to use a mixed-conducting membrane for the oxygen separation. Mixed-conducting material, for example perovskite oxides ( $ABO_3$ ) which offers potential solutions to eliminate the need for constructing the oxygen separation plant. The technology substantially reduces the cost of converting natural gas to syngas by 30%, and could save the oil and gas industry millions of dollars annually. Several advantages of using the oxygen-ion conducting membrane reactor include achieving high product selectivity, employing air as the source of the oxidant while eliminating  $N_2$  contamination in the product, circumventing flammability limits due to diffusion-limited operation, reducing a large part of the cost of gas compression in downstream processing, and avoiding the formation of environmental pollutant ( $NO_x$ ) during high-temperature reactions [4].

Mixed ionic electronic conductors (MIEC) exhibiting both electronic and ionic conductivities have a wide range of utilization such as fuel cells [5] which are expected to be a new and clean electric power source, in particular, for electric vehicles [6] and oxygen sensors are essential for combustion control. Major potential applications of mixed-conducting ceramic membranes in chemical and petroleum industries are as separators for air separation and as membrane reactors for partial oxidation of methane reactions.

Some perovskite oxides ( $ABO_3$ ) are found to be good mixed-conducting materials. In  $ABO_3$  perovskite structure, where A is the larger cation in a twelvefold coordination, and B is the smaller cation in the sixfold coordination with oxygen ions. The B ions can take a mixed-valence state such as transition metals. The partial substitution of cations in the  $ABO_3$  perovskite structure by cations with a lower valence either leads to formation of oxygen vacancies or to charge compensation by electronic charge carriers. The ratio of the ionic to electronic conductivity may vary markedly and in a complex manner with temperature, oxygen activity and dopants. The nature and extent of oxygen nonstoichiometry greatly affects the level of ionic conductivity, requiring judicious choice of the substituting ions. Large numbers of disordered oxygen vacancies at elevated temperatures may lead to the onset of high ionic conductivity. For example, in the series  $La_{1-x}Sr_xCo_{1-y}Fe_yO_{3-\delta}$ , the ionic conductivity in air at

temperatures 700-1,000°C can be one to two orders of magnitude larger than that of known zirconia-based solid electrolytes [7].

## 1.2 Literature review

Teraoka *et al.* demonstrated that the oxygen permeation fluxes through the LaCoO<sub>3</sub>-based perovskite-type membranes were 2-4 orders of magnitude higher than those of the stabilized zirconia at the same temperatures. Since then, increasing studies have been reported on the synthesis and properties of the LaCoO<sub>3</sub>-based perovskite-type ceramics because of their potential applications as membranes in gas separation and membrane reactors [8].

In solids, electrons or holes in narrow bands move either by tunneling through a potential well or by hopping. Though the hopping mobilities at room temperature are low, usually, the density of charge carrier is very large resulting in metallic conductivity. Conduction in these compounds occurs in two ways. La and Co in unsubstituted LaCoO<sub>3</sub> each has a valence of +3. Then the La atom is substituted with Sr (valence +2), to maintain charge neutrality, the valence of Co changes from +3 to +4. This causes the ‘creation’ of an electronic charge carrier, in this case, a hole. This hole, however, is localized over an area of the order of a lattice constant unlike metallic charge carriers and is often referred to as a polaron. On the other hand, any oxygen vacancy present in the compound acts as ionic charge carrier. However due to low mobility of ionic charge carriers as compared to polarons, the former do not play significant role in charge transport. The mobility of polarons occurs through a thermally activated process known as hopping. Thus, conduction in LSC occurs through small polaron hopping [9].

Petrov *et al.* studied the crystal structure, electrical conductivity and magnetic properties of La<sub>1-x</sub>Sr<sub>x</sub>CoO<sub>3-δ</sub> at different oxide compositions and oxygen nonstoichiometries. They reported electrical conductivity of La<sub>1-x</sub>Sr<sub>x</sub>CoO<sub>3-δ</sub> sample in air as a function of strontium content (x) at temperatures 333, 673, 873 and 973 K. The conductivity reaches a maximum at approximately x = 0.4 [10].

Pure LaCoO<sub>3</sub> behaves as a semiconductor at lower temperature. At higher temperatures it appears metallic. Substituting Sr for La, the transition to metallic behavior occurs at lower temperatures. The conductivity of series La<sub>1-x</sub>Sr<sub>x</sub>CoO<sub>3-δ</sub>

moves to lower Sr content with increasing temperature. The conductivity of  $\text{La}_{0.6}\text{Sr}_{0.4}\text{CoO}_{3-\delta}$  is 2,035 S/cm at 873 K [11]. The  $\text{La}_{0.6}\text{Sr}_{0.4}\text{CoO}_3$  (LSC) is a perovskite-type oxide and one of the noteworthy ceramic materials because of its mixed conductivity at high temperature.

In 2003, Lee *et al.* [12] studied the effect of surface modification by coating  $\text{La}_{0.6}\text{Sr}_{0.4}\text{CoO}_{3-\delta}$  (LSC) onto  $\text{La}_{0.7}\text{Sr}_{0.3}\text{Ga}_{0.6}\text{Fe}_{0.4}\text{O}_{3-\delta}$  (LSGF) and  $\text{La}_{0.6}\text{Sr}_{0.4}\text{Co}_{0.2}\text{Fe}_{0.8}\text{O}_{3-\delta}$  (LSCF) membranes to increase oxygen permeation fluxes. It was found that the modification of both surfaces with catalytically surface-reactive LSC made an excellent oxygen-permeable Ga-doped perovskite membrane. By introducing a highly surface exchange-reactive LSC coating on the LSGF membrane, significant promotion in the oxygen fluxes could be obtained. This promotion was conspicuous if the coating layer was porous, or had larger surface area. On the contrary, the oxygen permeation flux of LSCF was not affected by surface modification.

In 1995, Ten Elshof *et al.* [13] studied oxidative coupling of methane in a mixed-conducting perovskite membrane reactor. Dense  $\text{La}_{0.6}\text{Sr}_{0.4}\text{Co}_{0.8}\text{Fe}_{0.2}\text{O}_{3-\delta}$  membranes were applied as a dense membrane for oxygen supply in a reactor for methane coupling. Permeation fluxes are typically  $1 \text{ mmol m}^{-2}\text{s}^{-1}$  at  $900^\circ\text{C}$  with activation energy in the range of 130-140 kJ/mol. At temperatures above  $900^\circ\text{C}$ , substantial production of hydrogen was seen, which is likely due to thermal decomposition of methane. The  $\text{C}_2$  selectivity decreased strongly above this temperature. At  $880^\circ\text{C}$ ,  $\text{C}_2$  selectivity increased with increasing methane partial pressure, up to 67% at  $P_{\text{CH}_4} = 0.93 \text{ bar}$ . Increasing the oxygen partial pressure in the oxygen supplying chamber was shown to contribute mainly to the formation of CO and  $\text{CO}_2$ .

In 1999, Lane *et al.* [14] investigated electrical, electrocatalytic and catalytic properties of  $\text{LaCoO}_3$ -based materials due to their high electronic and ionic conductivity values. For example,  $\text{La}_{0.6}\text{Sr}_{0.4}\text{Co}_{0.2}\text{Fe}_{0.8}\text{O}_{3-\delta}$  (LSCF6428) is a mixed ionic-electronic conductor (MIEC) which displays significant and technologically useful levels of both oxygen ion and electronic conductivity. It also has the advantage of exhibiting a greater degree of stability, both mechanical and chemical, than some other mixed conducting oxides. From these reasons, the material has attracted interest for using in a wide range of application.

The  $\text{La}_{0.6}\text{Sr}_{0.4}\text{Co}_{0.8}\text{Fe}_{0.2}\text{O}_{3-\delta}$  perovskite-type oxides showed thermal expansion coefficient (TEC) of  $17.5 \times 10^{-6} \text{ K}^{-1}$ , electronic ( $\sigma$ ) of  $3.94 \times 10^{-1} \Omega^{-1}\text{cm}^{-1}$  and ionic conductivities ( $\sigma_{\text{O}}$ ) of  $8 \times 10^{-3} \Omega^{-1} \text{cm}^{-1}$  at  $800^{\circ}\text{C}$  in air [15].

In 2004, Xu *et al.* [16] studied the influence of sintering temperature on microstructure and mixed electronic-ionic conduction properties of  $\text{La}_{0.6}\text{Sr}_{0.4}\text{Co}_{0.8}\text{Fe}_{0.2}\text{O}_{3-\delta}$  ceramics in the range  $1,100\text{-}1,250^{\circ}\text{C}$ . The preferred sintering temperature was ascertained to be  $1200^{\circ}\text{C}$  for  $\text{La}_{0.6}\text{Sr}_{0.4}\text{Co}_{0.8}\text{Fe}_{0.2}\text{O}_{3-\delta}$  ceramics in terms of mixed conduction properties. The specimen sintered at  $1,200^{\circ}\text{C}$  exhibited an electrical conductivity  $1.26 \times 10^3 \Omega^{-1}\text{cm}^{-1}$  and an oxygen ionic conductivity  $3.73 \times 10^3 \Omega^{-1}\text{cm}^{-1}$  at  $800^{\circ}\text{C}$ .

Shao *et al.* [17] investigated the oxygen permeation behavior and stability of the  $\text{Ba}_{0.5}\text{Sr}_{0.5}\text{Co}_{0.8}\text{Fe}_{0.2}\text{O}_{3-\delta}$  oxide membrane. It was found that the new material had greatly improved structural stability than that of  $\text{SrCo}_{0.8}\text{Fe}_{0.2}\text{O}_{3-\delta}$ , also the oxygen permeation flux was improved modestly with the Ba doping. They showed the Ba doping effect on the properties of the  $\text{Ba}_{1-x}\text{Sr}_x\text{Co}_{0.8}\text{Fe}_{0.2}\text{O}_{3-\delta}$  material. The relationship of phase structure and stability with tolerance factor was proposed. The doping of Ba in  $\text{Sr}(\text{Co}_{0.8}\text{Fe}_{0.2})\text{O}_{3-\delta}$  could not lead to the improvement of these materials in the resisting of reduction, but the synergetic effect between cobalt and iron in the material was improved. Considerable high oxygen permeation rates were found for the BSCF membranes in the whole range of Ba doping content. The  $\text{Ba}_{0.3}\text{Sr}_{0.7}\text{Co}_{0.8}\text{Fe}_{0.2}\text{O}_{3-\delta}$  membrane had the highest oxygen permeation flux ( $1.19 \text{ ml/cm}^2 \text{ min}$  for  $1.50 \text{ mm}$  thickness membrane at  $850^{\circ}\text{C}$ ).

In 2000, Shao *et al.* [18] reported the oxygen permeation and stability of  $\text{SrCo}_{0.8}\text{Fe}_{0.2}\text{O}_{3-\delta}$  (SCF),  $\text{Ba}_{0.5}\text{Sr}_{0.5}\text{Co}_{0.8}\text{Fe}_{0.2}\text{O}_{3-\delta}$  (BSCF) oxide, using a combined citrate-EDTA complexing method. Oxygen permeation experiment indicated that BSCF membrane has also higher oxygen permeation flux than that SCF under air/He oxygen partial gradient. At  $950^{\circ}\text{C}$  the permeation flux reached about  $1.4 \text{ ml/cm}^2 \text{ min}$  through  $1.80 \text{ mm}$  thickness BSCF membrane. The permeation flux and phase structure of BSCF membrane were very stable at higher than  $850^{\circ}\text{C}$ . The phase transition was found to be reversible at high temperatures. BSCF is a promising material for using in oxidation membrane reactors at operation temperatures higher than  $850^{\circ}\text{C}$ .

In 2001, Shao *et al.* [19] applied BSCF ceramic membrane for activation of methane. The membrane reactor has intrinsic catalytic activities for methane conversion to ethane and ethylene. C<sub>2</sub> selectivity up to 40-70% was achieved with a methane conversion efficiency of 3.25-0.65% between 800°C and 900°C. The partial oxidation of methane to syngas in a BSCF membrane reactor was also performed by packing LiLaNiO/γ-Al<sub>2</sub>O<sub>3</sub> with 10% Ni loading as the catalyst. At the initial stage, oxygen permeation flux, methane conversion and CO selectivity were closely related with the state of the catalyst. Less than 21 hr. was needed for the oxygen permeation flux to reach its steady state 98.5% CH<sub>4</sub> conversion, 93.0% CO selectivity and 10.45 ml/cm<sup>2</sup> min oxygen permeation flux were achieved under steady state at 850°C. A BSCF membrane reactor was successfully operated at 875°C for more than 500 hr. for the POM reaction with fairly stable oxygen permeation flux of about 11.5 ml/cm<sup>2</sup> min.

For practical applications, a dense oxygen separation membrane should possess the following properties: (1) high oxygen permeation flux, i.e. having both high oxygen ionic and electronic conductivities; (2) structural stability within appropriate ranges of temperature and oxygen partial pressure; (3) sufficient mechanical strength and chemical compatibility.

However, it is difficult to meet all these requirements in a single phase because improvement in one aspect is often accompanied by the deterioration in others [20]. Therefore, another group of membrane materials called the dual-phase composites comprised of the mixture of an oxide ionic conductor and an electronically conducting phase. For the composite mixed conductor, it is possible to choose good ionic and electronic conductors as components, and to control the mixed conductivity by adjusting the fraction of constituents.

In 1992, Mazanec *et al.* [21] was first introduced the concept of dual-phase membranes. They made the composites of yttria stabilized zirconia oxide (YSZ) and Pd (or In/Pr), which showed much improved oxygen permeation flux when the metal volume percentage was above a critical value. After that, several researchers reported the improved oxygen permeation flux with different sets of dual-phase composites. In 2000, Kim *et al.* [22] investigated the oxygen permeation properties of Bi<sub>1.5</sub>Y<sub>0.3</sub>Sm<sub>0.2</sub>O<sub>3</sub> (BYS) /Ag dual-phase membranes compared with that of pure BYS membrane. The BYS and silver dual-phase membranes were prepared by mixing BYS and Ag powders. Oxygen permeation and electric conduction through

these BYS/Ag dual-phase membranes were studied in the temperature range of 650-850°C. They found that a percolative BYS/Ag membrane was obtained with 40 vol% silver. The BYS/Ag membrane is still non-percolative up to at least 30 vol% of silver. The electrical conductivity of the BYS/Ag 40% membrane was 104-105 times that of the BYS/Ag 30% membrane. The oxygen permeation flux of the BYS/Ag 40% membrane was  $5.8 \times 10^{-7}$  mol/cm<sup>2</sup>s at 850°C with oxygen partial pressures at the feed and permeates sides being 0.21 and 0.009 atm, respectively. The continuous silver phase in the percolative BYS/Ag membrane increases both the electronic conductivity and surface reaction rate which result in substantial improvement of oxygen permeation.

At the same time, the resultant properties may be strongly dependent of the interaction between the components. For example, the ionic transport in Ce<sub>0.8</sub>Gd<sub>0.2</sub>O<sub>2-δ</sub> (CGO)-La<sub>0.7</sub>Sr<sub>0.3</sub>MnO<sub>3-δ</sub> (LSM) membranes was found to decrease due to cation interdiffusion between phases [23]. In addition, CGO-LSM composites comprising significant volume fractions of CGO may be unstable under large oxygen pressure gradients due to significant volume changes of ceria on reducing.

In 2004, Shaula *et al.* [24] investigated the substituting LSM with a mixed conductor, which may contribute to ionic transport and using (La<sub>0.9</sub>Sr<sub>0.1</sub>)<sub>0.98</sub>Ga<sub>0.8</sub>Mg<sub>0.2</sub>O<sub>3-δ</sub> (LSGM) which more stable solid electrolyte phase instead of CGO. Composite ceramics made of two perovskite-type compounds, LSGM and La<sub>0.8</sub>Sr<sub>0.2</sub>Fe<sub>0.8</sub>Co<sub>0.2</sub>O<sub>3-δ</sub> (LSFC) were mixed in the ratio 60:40 % wt. The membranes were sintered at elevated temperatures (1,320-1,410°C). To obtain the dense membranes and leads to fast interdiffusion of the components, forming almost single perovskite phase ceramics with local inhomogeneities. This phase interaction decreases the oxygen ionic transport in the composites, where the level of ionic conductivity is intermediate between those of LSGM and LSFC was found to decrease both ionic and electronic conductivities and to increase thermal expansion. The average thermal expansion coefficients (TEC) of LSGM-LSFC composites are  $(12.4-13.5) \times 10^{-6}$  K<sup>-1</sup> at 100-650°C and  $(17.8-19.8) \times 10^{-6}$  K<sup>-1</sup> at 650-1000°C.

In 2003, Wang *et al.* [25] improved the oxygen permeation of the Fe-doped LaGaO<sub>3</sub> (LSGF) by introducing a phase with high electronic conductivity such as BSCF. They reported a new structure of dense dual-phase membrane. In this dual-

phase membrane, oxygen ion conductivity (OIC-phase) is perovskite oxide made of  $\text{La}_{0.15}\text{Sr}_{0.85}\text{Ga}_{0.3}\text{Fe}_{0.7}\text{O}_{3-\delta}$  (LSGF) and electron conductivity (EC-phase) is perovskite oxide made of BSCF. This dual-phase membrane consists of an OIC ceramic phase defined by the closed packing of OIC ceramic particles and a three-dimensional film of an EC-phase covering the surface (or grain-boundary) of the OIC ceramic particles. Dense BSCF-LSGF composites of BSCF and LSGF powders were mixed in the ratio 1:12.8 by volume. The oxygen permeation test shows that the oxygen permeation flux of LSGF-BSCF membrane ( $J_{\text{O}_2} = 0.45 \text{ ml/cm}^2 \text{ min}$ , at  $915^\circ\text{C}$ ) is much higher than that of LSGF membrane ( $J_{\text{O}_2} = 0.05 \text{ ml/cm}^2 \text{ min}$ ).

In 2000, Ishihara, et al. [26] compared the conventional mixed electronic and ionic conductor of  $\text{LaCoO}_3$  with  $\text{LaGaO}_3$ . These  $\text{LaGaO}_3$ -based perovskite oxides exhibited notably high oxide ion conductivity but low electronic conductivity. Recently, the mixed electronic-oxide ionic conductors, based on  $\text{LaGaO}_3$  and doped with a transition metal used for separating air. It became evident that the electrical conductivity was greatly improved by doping Fe, Co or Ni for the Ga site of  $\text{LaGaO}_3$ . In particular, Fe-doped  $\text{LaGaO}_3$  exhibited a high oxygen permeation rate and stability against reduction.

Recently, the  $\text{LaGaO}_3$  based perovskite and doped with transition metal was reported by some groups for a membrane to separate oxygen from air. Ishihara et al. [27] proposed that Fe doped  $\text{LaGaO}_3$  based oxide exhibited high electronic hole and oxide ion conductivity.  $\text{La}_{0.7}\text{Sr}_{0.3}\text{Ga}_{0.6}\text{Fe}_{0.4}\text{O}_3$  is highly attractive as the oxygen permeating membrane for  $\text{CH}_4$  partial oxidation. In the system  $(\text{La,Sr})(\text{Fe,Ga})\text{O}_{3-\delta}$ , the highest level of oxygen-ionic transport was observed for  $\text{La}_{0.3}\text{Sr}_{0.7}\text{Fe}_{1-x}\text{Ga}_x\text{O}_{3-\delta}$  series.

Yaremchenko et al [28] investigated substitution of iron with aluminum in perovskite-type  $\text{La}_{0.3}\text{Sr}_{0.7}\text{Fe}_{1-x}\text{Al}_x\text{O}_{3-\delta}$ . The results suggest that the substitution of iron in  $\text{La}_{0.3}\text{Sr}_{0.7}\text{FeO}_{3-\delta}$  with aluminum is less favorable with respect to Ga doping in terms of the oxygen ionic transport, but may provide significant advantages if taking into account the high costs and possible volatilization of gallium oxide under reducing conditions. The perovskite-type  $\text{La}_{0.3}\text{Sr}_{0.7}\text{Fe}_{1-x}\text{Al}_x\text{O}_{3-\delta}$  were synthesized by glycine-nitrate process. XRD analysis showed formation of cubic perovskite phase for  $\text{La}_{0.3}\text{Sr}_{0.7}\text{Al}_{0.2}\text{Fe}_{0.8}\text{O}_{3-\delta}$ . The level of oxygen ionic conduction



in Al-containing ferrites was found lower than in Ga-substituted analogues. The oxygen permeability of  $\text{La}_{0.3}\text{Sr}_{0.7}\text{Al}_{0.2}\text{Fe}_{0.8}\text{O}_{3-\delta}$  will improve by using the mixed-conductor with dominant electron conductivity.

In the present work, we report the preparation dual-phase membranes comprised of  $\text{La}_{0.3}\text{Sr}_{0.7}\text{Al}_{0.2}\text{Fe}_{0.8}\text{O}_{3-\delta}$  and  $\text{La}_{0.6}\text{Sr}_{0.4}\text{CoO}_{3-\delta}$  (dominant oxygen ion conductivity),  $\text{Ba}_{0.5}\text{Sr}_{0.5}\text{Co}_{0.8}\text{Fe}_{0.8}\text{O}_{3-\delta}$  and  $\text{La}_{0.6}\text{Sr}_{0.4}\text{Co}_{0.8}\text{Fe}_{0.2}\text{O}_{3-\delta}$  (dominant electron conductivity). The oxygen adsorption-desorption of these dual-phase was investigated.

### 1.3 The objectives of the thesis

The objectives of this study are as follows:

1. To synthesize perovskite powders of  $\text{La}_{0.3}\text{Sr}_{0.7}\text{Al}_{0.2}\text{Fe}_{0.8}\text{O}_{3-\delta}$  (LSAF3728),  $\text{Ba}_{0.5}\text{Sr}_{0.5}\text{Co}_{0.8}\text{Fe}_{0.8}\text{O}_{3-\delta}$  (BSCF5582),  $\text{La}_{0.6}\text{Sr}_{0.4}\text{Co}_{0.8}\text{Fe}_{0.2}\text{O}_{3-\delta}$  (LSCF6482),  $\text{La}_{0.6}\text{Sr}_{0.4}\text{CoO}_{3-\delta}$  (LSC64).
2. To prepare dual-phase membranes of LSAF–BSCF, LSAF–LSCF and LSAF–LSC in various ratios and characterize the structures by XRD.
3. To study oxygen permeation property of the dual-phase membranes by using TGA and  $\text{O}_2$ -TPD.

## CHAPTER II

### THEORY

Perovskites are a large family of crystalline ceramics that derive their name from a specific mineral known as perovskite. They are the most abundant minerals on earth and have been of continuing interest to geologists for the clues they hold to the planet's history. The parent material, perovskite, was first described in the 1830's by the geologist Gustav Rose, who named it after the famous Russian mineralogist Count Lev Aleksevich von Perovski. There are many perovskite compound types, each have various properties that are used in different applications such as insulators, dielectrics, magnetic materials, ionic conductors, mixed conductors, and superconductors. This study is focused on the use of mixed conducting perovskites as oxygen separation membranes.

#### 2.1 Structure of perovskites

##### 2.1.1 Crystal structure

An ideal perovskite structure has an  $ABO_3$  stoichiometry and a cubic crystal structure is composed of a three-dimensional framework of corner-sharing  $BO_6$  octahedron. The A-site cation fills the 12 coordinate cavities formed by the  $BO_3$  network and is surrounded by 12 equidistant anions [29]. Figure 2.1 depicts the corner sharing octahedral that form the skeleton of the structure, in which the center position is occupied by the A cation. Alternatively, this structure can be viewed with the B cation placed in the center of the octahedron and the A cation is in the center of the cube.

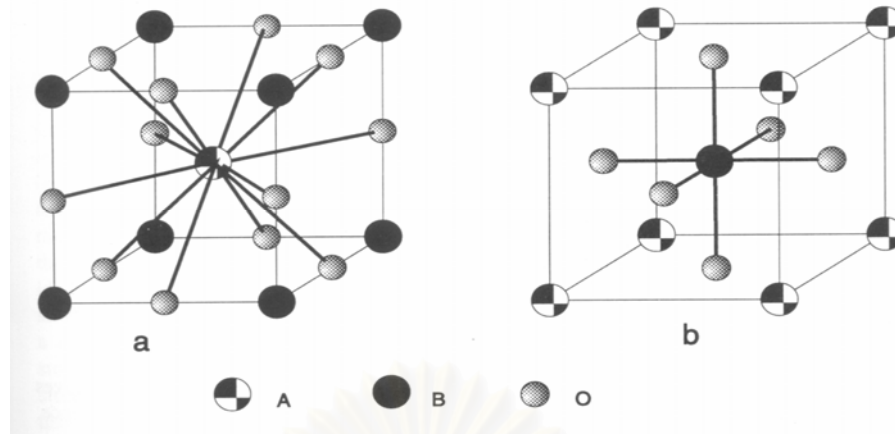


**Figure 2.1**  $ABO_3$  ideal perovskite structure showing oxygen octahedron containing the B ion linked through corners to form a three-dimensional cubic lattice.

### 2.1.2 Tolerance factors in perovskites

Goldschmidt et al. introduced a tolerance factor,  $t$ , describing the relationship between symmetry and ionic radii in the perovskites [30]. It can be defined as:

$$t = \frac{(r_A + r_O)}{\sqrt{2}(r_B + r_O)} \quad (2.1)$$

Where  $r_A$  and  $r_B$  are the mean ionic radii for A and B site cation taking into account the coordination numbers, respectively, and  $r_O$  is the radii of oxide ion. This can be illustrated for the perovskite structure by deriving a relationship between the radii of the various ions. Figure 2.2 shows the relationship between ionic radii in the perovskite structure.

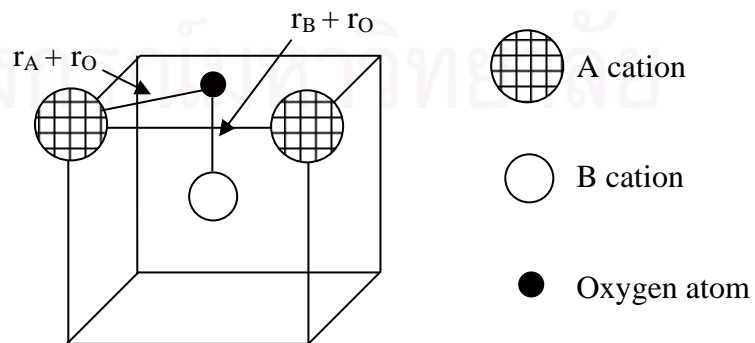


**Figure 2.2** The relationship between symmetry and ionic radii in the perovskite.

The atoms are touching one another, the B-O distance is equal to  $a/2$  ( $a$  is the cubic unit cell parameter) while the A-O distance is  $(a/\sqrt{2})$  and the following relationship between the ionic radius ( $r$ ) holds:  $r_A + r_O = \sqrt{2}(r_B + r_O)$ . The ideal perovskite is the cubic structure with the tolerance factor close to 1.0. It is known that almost all perovskites have a  $t$  value ranging from 0.75 to 1.00. However, it seems that  $t = 0.75-1.00$  is a necessary but not a sufficient condition for the formation of the perovskite structure. Even in the range of  $t = 0.8-0.9$  which is the most favourable value for perovskites. The distorted structure may show orthorhombic, rhombohedral, tetragonal, monoclinic and triclinic symmetry at room temperature but it transforms to the cubic structure at ambient temperature.

### 2.1.3 Nonstoichiometry in perovskites

Besides the ionic radii requirements, another condition to be fulfilled is electroneutrality, i.e., the sum of charges of A and B equals the total charge of oxygen anions. This is attained by means of appropriate charge distribution of the form  $A^{1+}B^{5+}O_3$ ,  $A^{2+}B^{4+}O_3$ , or  $A^{3+}B^{3+}O_3$ . In addition to this, partial substitution of A and B ions is allowed, thus yielding a plethora of compounds while preserving the perovskite structure. However, deficiencies of cations at the A- or B-sites or of oxygen anions are frequent, which results in defective perovskites. Nonstoichiometry in perovskites can arise from cation deficiency (in the A or B site), anion deficiency, or anion excess. For the cation deficiency, A-site cations can be missing without collapse of the perovskite network because of the stability of the  $BO_3$  group. On the contrary, B-site vacancies are not energetically favored because of the large formal charge and the small size of the B cations in perovskites. Nevertheless, an oxygen vacancy in perovskites is more common than a cation deficiency [31].

Many oxygen-deficient perovskites can be described on the basis of complex perovskite-related super-structures of general formula  $A_nB_nO_{3n-1}$ , in which the stacking manner depends on the size, electronic configurations, and coordination numbers of A and B cations. Oxygen vacancies are accomplished by substituting ions of similar size but different valence. For example, some of the  $La^{3+}$  ions in  $LaBO_3$  are replaced by  $Sr^{2+}$  to form  $La_{1-x}Sr_xBO_{3-\delta}$ , and therefore, oxygen vacancies are formed.

The former composition can be considered as an anion-deficient perovskite with one-sixth of the oxygen ions being vacant. Oxygen vacancies are ordered in alternate [001]  $\text{BO}_2$  planes of the cubic structure such that alternate [110] rows of oxide anions are missing.

## 2.2 Physical properties

The perovskite structure class is one of the most commonly occurring and important in all of materials science. Physical properties of interest among perovskites include superconductivity, colossal magnetoresistance, ionic conductivity, and a multitude of dielectric properties. Because of the great flexibility inherent in the perovskite structure, there are many different types of distortions which can occur from the ideal structure. Many of the physical properties of perovskites depend crucially on the details of these distortions, particularly the electronic, magnetic and dielectric properties which are so important for many of the applications of perovskite materials. The  $\text{ABO}_3$  perovskites display physical properties such as ferroelectricity ( $\text{BaTiO}_3$ ), ferromagnetism ( $\text{SrRuO}_3$ ), weak ferromagnetism ( $\text{LaFeO}_3$ ), superconductivity ( $\text{YBa}_2\text{Cu}_3\text{O}_7$ ), large thermal conductivity due to exciton transport ( $\text{LaCoO}_3$ ), insulator-to-metallic transitions of interest for thermistor applications ( $\text{LaCoO}_3$ ), a fluorescence compatible with laser action ( $\text{LaAlO}_3 : \text{Nd}$ ), and transport properties of interest for high temperature thermoelectric power ( $\text{La}_2\text{CuO}_4$ ).

### 2.2.1 Mixed ionic-electronic conductors

Perovskite oxide exhibits both ionic and electronic conductivity. It may show both high oxygen ion conductivity due to the high oxygen vacancy concentration, and a high electronic conductivity due to the mixed-valence state. [32], the B ions can take a mixed-valence state, charge neutrality is maintained by both the formations of oxygen vacancies and a change in the valence state of the B ions. The B-site ion substitution can increase the concentration of oxygen vacancies, such as Cu and Ni ions, which naturally take the divalent oxidation state [33]. If the valence state of the B ions is fixed, neutrality is maintained only by the formation of oxygen vacancies. The oxides may be predominantly ionic conductors, in this case.

The electrical properties of perovskites have aroused special interest since the discovery in 1986 of superconductivity at 40 K in cuprates. These cuprates are whole superconductors, exhibiting a mixed valence of copper  $\text{Cu}^{2+}$ - $\text{Cu}^{3+}$ . Among these, the exception is Ce-doped  $\text{Nd}_2\text{CuO}_4$ , with  $T_c$  close to 25 K, which belongs to a different structural type and is an electron superconductor. All these compounds have a common feature, the two-dimensional character of the structure, which has been shown to be an important factor for the existence of superconductivity at high temperature.

The overall electrical conductivity  $\sigma_{tot}$  is the sum of electronic conductivity  $\sigma_e$  and ionic conductivity  $\sigma_i$ , as Equation (2.2),

$$\sigma_{tot} = \sum \sigma_{ij} + \sigma_e \quad (2.2)$$

Where  $\sigma_{ij}$  is the partial conductivity (in  $\Omega^{-1}\text{cm}^{-1}$ ) of the  $j$ th-type ionic charge carriers presenting in the solid. The electrical behavior in perovskites depends on the outermost electrons, which may be localized at specific atomic sites or may be collective. Since localized electrons may carry a spontaneous moment, there is a strong correlation between the electrical and magnetic properties of perovskites. Rare-earth perovskites containing transition ions show widely differing electrical properties.

The electronic conduction can be n-type or p-type, depending on the material properties and ambient oxygen partial pressure. The energy level shifts from the center of the energy gap toward the empty zone for an n-type semiconductor or the filled band for a p-type semiconductor. An n-type conductor is an electron conductor while a p-type conductor is an electron hole conductor. It was noticed that perovskites with high p-type electronic conductivity tended to be active for deep methane oxidation reactions while those with high n-type electronic conductivity, ionic conductors, and insulators were all found to be more selective to  $\text{C}_2$  compounds

Ionic conductivity occurs normally via interstitial sites or by hopping into a vacant site (vacancy motion) or a more complex combination based on interstitial and vacant sites. Ionic charge carriers can be either atomic in nature or normally defects of either the anionic or cationic sublattice.

In order to characterize the materials, it is more often to measure their electronic and ionic conductivity instead of concentrations of electrons (holes) and mobile ions (vacancies). The calculated ionic and electronic conductivity, which were separately, measured by using 4-probe ionic direct current and ordinary 4-probe direct current techniques, respectively.

### 2.2.2 Magnetic properties

In the ideal cubic perovskite structure, each atom of oxygen is shared by two  $B^{3+}$  ions, forming a B-O-B angle of  $180^\circ$ . Such a configuration is favorable for super exchange interactions between magnetic  $B^{3+}$  cations. This exchange usually results in anti-parallel coupling of nearest-neighbor magnetic moments. When the  $B^{3+}$  ions are in two sub lattices ( $A_2BB'O_6$ ) the other spin arrangements are possible. If  $B'$  is a diamagnetic ion, the  $B^{3+}$  ions are aligned anti-ferromagnetic, and the most important exchange mechanism is believed to be a longer range super exchange interaction through two oxygens of the type B-O-B'-O-B. The B-B separation is now considerably longer than the 0.4 nm separation found in the ideal perovskite. The  $LnFeO_3$  ( $Ln$  = lanthanide) perovskites are those that have attracted the most attention because of their possible applications as technological magnetic materials. These compounds show a weak spontaneous magnetic moment, which is attributed to a slight canting of the iron moments, which are otherwise anti-ferromagnetic aligned. Similarly,  $LnMnO_3$  shows very interesting magnetic properties. These manganites containing mostly  $Mn^{3+}$  or  $Mn^{4+}$  ions show anti-ferromagnetic behavior.

## 2.3 Dense perovskite membranes for oxygen separation

### 2.3.1 Perovskite membrane concepts

A principle behind application of this perovskite membrane reactor technology for the spontaneous conversion of natural gas into synthesis gas is shown in Figure 2.3. These devices behave as short-circuited electrochemical cells, except that no electrical energy is required to drive this thermodynamically downhill process.

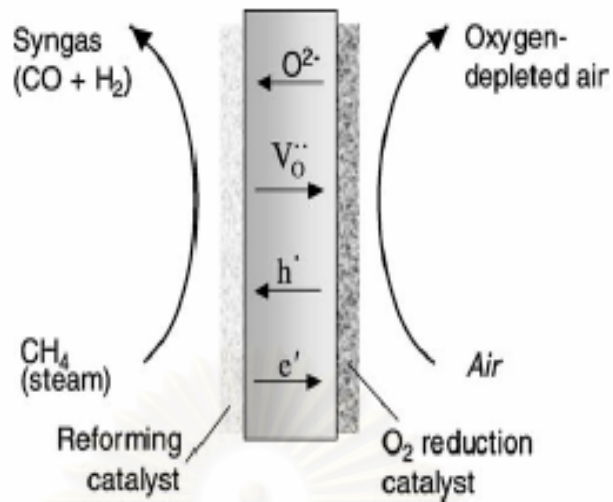


**Figure 2.3** Operating principle of a ceramic membrane reactor for the partial oxidation of methane to syngas.

Oxygen separation with oxide ion conducting membranes consists of a sequence of steps as shown in Figure 2.4.

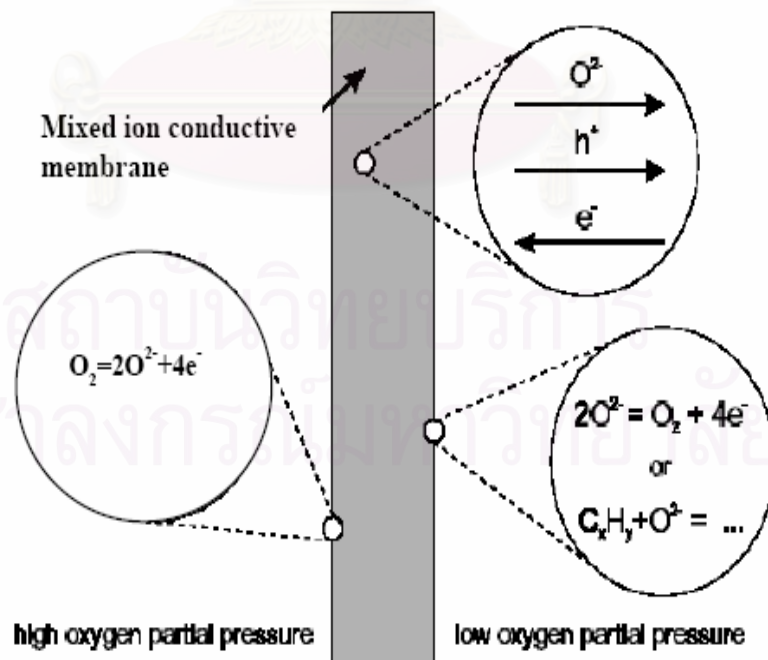


**Figure 2.4** Perovskite membrane concepts.



At the feed side, oxygen molecules from gaseous mixture adsorb at the membrane surface and disassociate into oxide ions by taking up electrons. These ions transfer through the bulk of the membrane to the permeate side, where they release electrons and convert back to gaseous oxygen molecules. Note that this sequence can not last unless a path is available for electrons to return from the permeate side to the feed side. Therefore, it is desirable that the membrane is made from the ion-conducting material that can conduct electrons as well. In practice, two categories of mixed oxide ion and electron conducting materials have been used to fabricate oxygen permeable membranes [34].

### 2.3.2 Oxygen permeation through a mixed-conducting membrane

The operating of an MIEC membrane is illustrated in Figure 2.5. By imposing an oxygen partial pressure differential across the membrane oxygen is driven from the high partial pressure side to the low partial pressure side. In a typical membrane reactor, the pressure differential is provided by air on one side and a reducing gas, i.e. depleting the oxygen partial pressure by a chemical reaction, on the other side of the membrane [35]. The oxygen anions permeate from the high to the low partial pressure side, while overall charge neutrality was maintained by a counterbalancing flux of electrons (and/or electron holes), as depicted schematically in Figure 2.5.

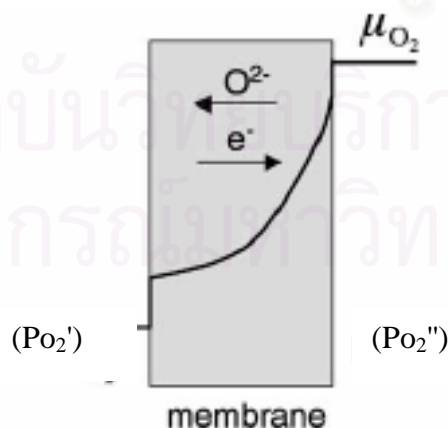


**Figure 2.5** Schematic illustration of the profile in oxygen chemical potential  $\mu_{O_2}$  across the MIEC membrane at steady-state conditions.

Mechanism for oxygen permeation through a mixed-conducting membrane can be described as follows [36, 37]:

1. Mass transfer of gaseous oxygen from the gas phase with high oxygen partial pressure to the membrane surface.
2. Reaction between the molecular oxygen and oxygen vacancies at the membrane surface.
3. Dissociation and electron transfer, giving chemisorbed oxygen species.
4. Incorporation in membrane surface layer.
5. Diffusion of lattice defects to interior.
6. Oxygen vacancy bulk diffusion across the membrane.
7. Association and electron transfer, forming chemisorbed oxygen species.
8. Desorption from the surface.
9. Mass transfer of oxygen from the membrane surface to the gas phase with low oxygen partial pressure.

For practical applications, it is important to know whether the oxygen flux was limited by bulk diffusion or a surface exchange process for a certain compound. Oxygen activity drops generally occur in both interface regions and the bulk of the material as shown in Figure 2.6.

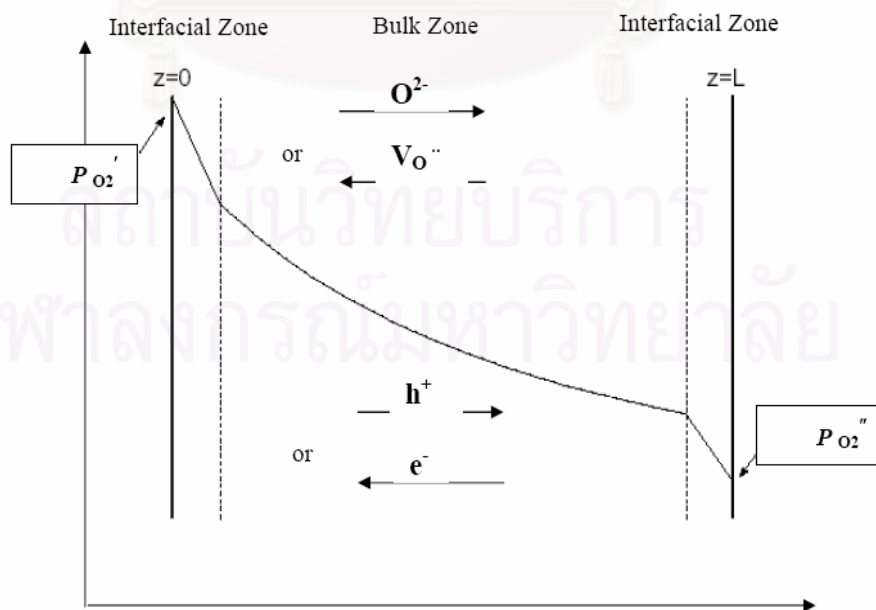


**Figure 2.6** The curve shows a possible  $P_{O_2}$  Profile over the membrane. A single prime indicates air side, double prime indicates permeate side.

Classical Wagner theory is usually adopted to express the flux of oxygen through MIEC membranes exposed by the following equation [13]:

$$J_{O_2} = \frac{RT}{4^2 F^2 L} \int_{P_{O_2}''}^{P_{O_2}' } t_i t_{el} \sigma_{total} d \ln p_{O_2} \quad (2.2)$$

Here  $J_{O_2}$  is the oxygen permeation flux in  $\text{mol cm}^{-2} \text{s}^{-1}$ ,  $t_i$  is the ionic transference numbers,  $t_{el}$  is electronic transference numbers,  $\sigma_{total}$  ( $= \sigma_{ion} + \sigma_{el}$ ) is the total conductivity ( $\Omega^{-1} \text{cm}^{-1}$ ),  $P_{O_2}'$  and  $P_{O_2}''$  are the oxygen partial pressures at the high and the low partial pressure side of the membrane, respectively;  $L$  is the membrane thickness (cm).  $R$ ,  $F$  and  $T$  refer to the gas constant ( $\text{J mol}^{-1} \text{K}^{-1}$ ), Faraday's constant ( $\text{C mol}^{-1}$ ) and the temperature (K), respectively.

This equation is valid only if the oxygen flux through the membrane is controlled by bulk diffusion through the oxide lattice. Reduction of the membrane thickness will lead to higher oxygen flux.

## 2.4 Perovskite synthesis

The procedure for preparing perovskite type membranes consists of three steps: powder synthesis, shaping and sintering. Powder synthesis, as the first step, plays a critical role in determining the particle size of the powder, and consequently has an influence on the microstructure of the membrane. There are many routes to synthesize powders, such as a conventional solid-state reaction method and a wet chemical process that includes thermal decomposition of cyanide, metal-EDTA, chemical co-precipitation and the sol-gel process. Cui and Liu [38] reported in their study that powders synthesized by different methods had different temperatures of crystal transformation and the surface defect of powders dried by a supercritical method improved the formation of the crystal structure.

The synthesis of perovskite powder has been achieved by many methods, including a conventional solid-state reaction method and a solution reaction that includes thermal decomposition of cyanide, metal-EDTA, chemical co-precipitation and the sol-gel process etc.

### 2.4.1 Gas phase reaction

The deposition of perovskite films with a specific thickness and composition generally requires gas phase reaction or transport. Many physical techniques have been developed for gas phase deposition such as laser ablation, molecular beam epitaxy, dc sputtering, magnetron sputtering, electron beam evaporation and thermal evaporation. In general, they can be divided into two categories based on the target they use. The first type uses separate targets where a different speed of deposition for each element has to be determined. The second method uses the performed perovskite material itself as target and the stoichiometric phase is transported to the substrate by sputtering or ablation techniques.

### 2.4.2 Solid-state reaction

The solid state reaction is very convenient but the impurities are introduced from raw materials, milling media, and the calcination container. Because of the high temperature required for the complete reaction. Conventional processing of the perovskite-related materials uses solid-state reactions between metal-carbonates, hydroxides, and oxides. LSCF represents a typical case. Raw materials  $\text{La}_2\text{O}_3$ ,  $\text{SrCO}_3$ ,  $\text{CoO}_3$ , and  $\text{Fe}_2\text{O}_3$  were mixed and ball-milled. After drying, then the mixed powders were calcined at  $1,000^\circ\text{C}$  to remove impurities and to achieve single-phase perovskite powder.

### 2.4.3 Solution reaction

A convenient way of classifying the methods, which state from solution, is to consider the means used for solvent removal. Two basic classes exist. The first is based upon precipitation with subsequent filtration, centrifugation, etc., used to separate the solid and liquid phases. The second basic method depends upon thermal processes, e.g., evaporation, sublimation, combustion, etc., to remove the solvent. The latter method is preferred because of the possible contemporaneous conversion of the residue into the desired product.

The solution reaction method is potentially advantageous in comparison with other methods for achieving homogeneous mixing of lower processing temperature,

better control the stoichiometry and purity, greater flexibility in from thin films and new compositions, an easily generated porous, and an enhanced ability to control particle size.

## **2.5 Perovskite membrane preparation**

### **2.5.1 Solution reaction synthesis of perovskites**

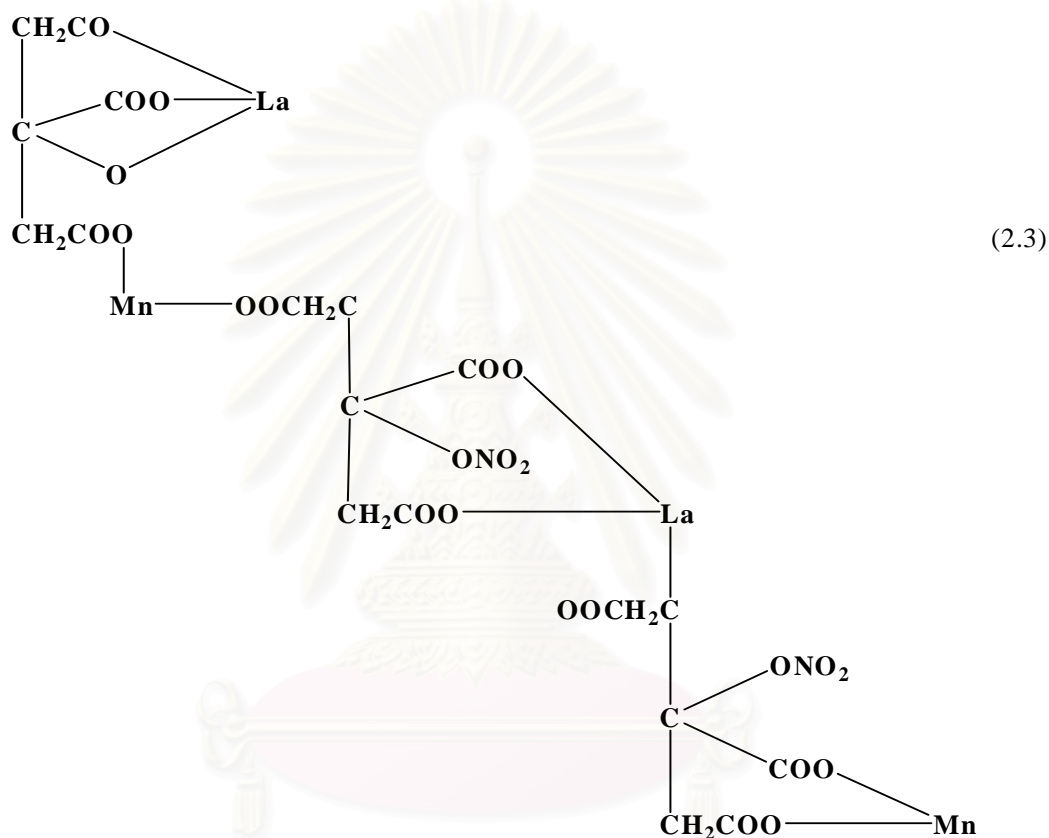
Solution reactions have been developed from solid-state synthesis to produce the required properties of raw perovskite powders, such as spray-pyrolysis, freeze drying, precipitation, sol-gel and liquid mix process, etc. Because of the conventional solid-state synthesis promotes the crystal growth and resulting in a hard agglomeration. The perovskite powders made from solution chemical methods are very fine, and can be not agglomerate, which facilitates the densification process. This method using sintering temperature which can be lower than those made from conventional solid-state synthesis methods.

The initial process was pioneered by Pechini and is referred to either as Pechini process [39]. This method includes first dissolving hydrous oxides or alkoxides of the elements in a polyhydroxy alcohol such as ethylene glycol, with a chelating agent, such as citric acid. Then polyhydroxy alcohol such as ethylene glycol is added and the liquid is heated to 150 to 250°C to allow the chelates to undergo polyesterification. Heating is continued to remove excess water, resulting in solid polymeric resin. The temperature is increased to about 400°C to char or decompose the resin. The temperature is further increased to 500 to 900°C to form crystallites of the mixed oxide composition. The crystallites are typically 20 to 50 nm and clustered into agglomerates. An advantage of the Pechini method is that the viscosity and polymer molecular weight of the solution can be tailored by varying the citric acid/ethylene glycol ratio and the solution synthesis temperature.

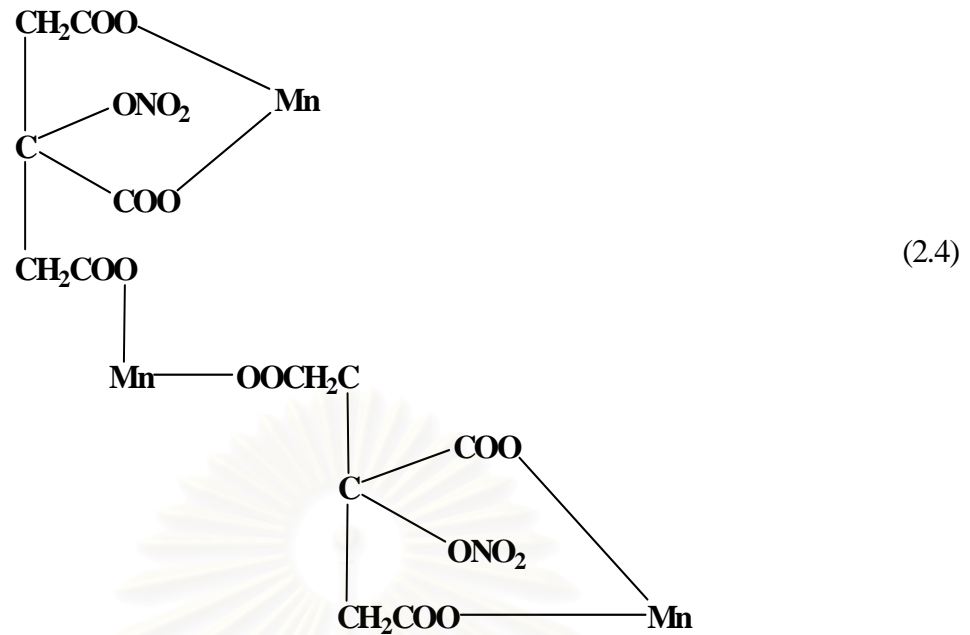
The modifications of Pichini process have been developed. One was called amorphous citrate process that involves producing precursor from citric acid and metal nitrate before thermal decomposition. Baythoun and Sale investigate the production of Sr-substituted  $\text{LaMnO}_3$  perovskite powder by the amorphous citrate

process, the manganese citrate-nitrate precursor may be revealed as in Equation 2.3 [40].

In the complex the lanthanum is triply charged and replaces in one case the hydrogen of three  $\text{-COOH}$  groups (as in normal citrate formation) and in another case it replaces the hydrogen of one  $\text{-OH}$  group and two  $\text{-COOH}$  groups. Manganese in the divalent state replaces the hydrogen in two  $\text{-COOH}$  groups while  $\text{NO}_2$  replaces the hydrogen of one  $\text{-OH}$  group



The amounts of metal and citric acid should not less than equimolar. In all cases the minimum amount of citric acid used was that necessary to bond the metals if all the  $\text{NO}_3^-$  ions were replaced. If the high amount of citric acid was used,  $\text{Mn}_2\text{O}_3$  was presented from the complex as shown in Equation 2.4:



In this case, structure would allow some citric acid, water, and nitrate ions to be lost during the preparation of gel. Every three molecules of citric originally present one remains uncombined and may be removed from the mixture by either evaporation or decomposition to yield acetone, carbon dioxide and water during the precursor preparation in the vacuum oven.

### 2.5.2 Powder sizing

A single particle size does not produce good packing. Optimum packing for particles all the same size results in over 30% void space. Adding particles of a size equivalent to the largest voids reduces the void pore volume to 23%. Therefore, to achieve maximum particle packing, a range of particle sizes is required. Powder particles are influenced on compacting and sintering. The objective of the pressing step is to achieve maximum particle packing and uniformity.

Hard and dense agglomerates in ceramic powders usually result in large interagglomerate pores after sintering. Therefore small particle size is important because it facilitates the high strength of green disc and the sintering process. The primary driving force for densification of a compacted powder at high temperature is the change in surface free energy. Very small particles have high surface areas. The high surface free energy and very strong thermodynamic drive force decrease their surface by bonding them together. The particle with approximate sizes of 1  $\mu\text{m}$  or

less can be compacted into a porous shape and sintered at a high temperature to near-theoretical density [41]. Typically, the finer the powder, the greater its surface area, and the lower the temperature and shorter time for densification. Long times of the sintering temperature was a result of the increasing in grain growth which causes lower strength.

### **2.5.3 Powder compacting by uniaxial pressing**

Uniaxial pressing involves the compaction of powder into a rigid die by applying pressure in a single axial direction through a rigid punch or piston. The presses are usually mechanical or hydraulic. Pressing results in the direct contact of particles, reduces the average distance between particles, and changes the shape of particles. The apparent density of a compact was controlled by mixing of the proper various particles size fractions.

To enhance the compacting, before pressing, the powder should be disaggregated by mixing the powder with solvent such as isopropanol in the ultrasonic bath or added a couple drops of acetone to reduce the surface tension.

### **2.5.4 Sintering**

Sintering is the process whereby powder compacts are heated so that adjacent particles fuse together. The fusing of particles results in an increase in the density of the part and hence the process is sometimes called densification. There are some processes such as hot isostatic pressing which combine the compaction and sintering processes into a single step.

The density of the component can also change during sintering, depending on the materials and the sintering temperature. These dimensional changes can be controlled by an understanding and control of the pressing and sintering parameters, and components can be produced with dimensions that need little or no rectification to meet the dimensional tolerances. The driving force for sintering is the decrease in surface free energy that occurs as the surface area of the polycrystalline aggregate is reduced. This process can be achieved by solid-state reaction or alternatively in the presence of a liquid phase. When a powdered aggregate is sintered, pore size is reduced, and the grain growth can be much enhanced. The growth of the neck is due



to the transport of matter or of the counter-flow of vacancies between the particles and the pores. In crystalline powder, its transport occurs by diffusion (bulk, surface, or grain boundary diffusion), whereas in amorphous materials, it occurs by viscous flow. Kuczynski has defined the neck growth as in Equation 2.5.

$$X^n/r^m = kt \quad (2.5)$$

Where  $X$  and  $r$  are defined in Figure 2.7,  $t$  is the time,  $k$  is the temperature dependent constant,  $n$  and  $m$  are constants dependent on the mechanisms of growth, viscous or bulk diffusion, surface diffusion, or evaporation and condensation.

The sintering process can be distinguished by three stages. The first stage or initial stages during which the necks form at points of particle contact and the particles usually center approach each other. At this stage the individual particles are still distinguishable. The intermediate stage during that the necks become large, resulting in the formation of an interconnected pore structure. The third or the final stages, the pores become isolated.

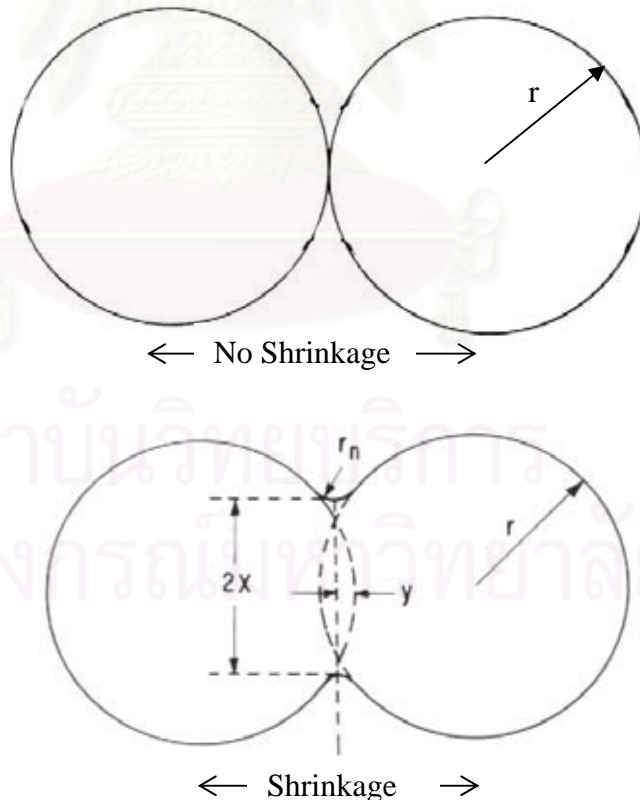
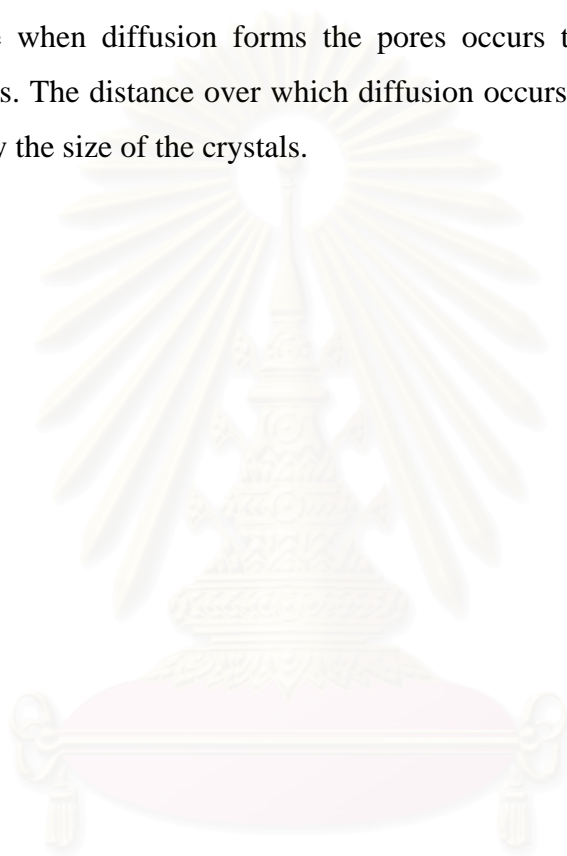


**Figure 2.7** Mechanism of sintering.

Elimination of the interconnectivity of pores eliminates surface and vapor transport. The most important diffusion paths during the sintering of two spheres with a grain boundary are surface diffusion, grain boundary diffusion, volume diffusion from the grain boundary to the neck surface, and volume diffusion from the sphere surface to the neck surface.

The sintering rate also affected by the crystallization and growth processes, which occur concurrently. The sintering rate is reduced when there is intensive grain growth because when diffusion forms the pores occurs toward the boundaries of individual grains. The distance over which diffusion occurs with a reduction in pores is determined by the size of the crystals.



สถาบันวิทยบริการ  
จุฬาลงกรณ์มหาวิทยาลัย

## CHAPTER III

### EXPERIMENTAL

The apparatus and experimental procedures including processing of perovskite powders synthesis, perovskite membranes preparation and characterization of materials, are described below:

#### 3.1 Chemicals

The chemicals listed in Table 3.1, were used without further purification.

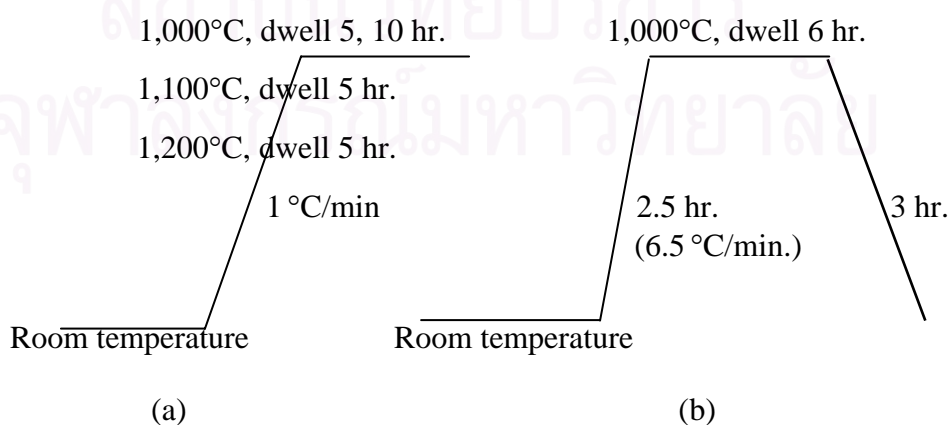
**Table 3.1** Chemical and reagents for synthesis of perovskite

Reagents	Formula Weight	Purity %	Company
Al(NO <sub>3</sub> ) <sub>3</sub> ·9H <sub>2</sub> O	375.13	≥98	Fluka
Ba(NO <sub>3</sub> ) <sub>2</sub>	261.35	≥99	Fluka
Co(NO <sub>3</sub> ) <sub>2</sub> ·6H <sub>2</sub> O	291.03	≥98	Fluka
Citric Acid	192.43	99.5	Fluka
Fe(NO <sub>3</sub> ) <sub>3</sub> ·9H <sub>2</sub> O	404.00	98-101	Fluka
HNO <sub>3</sub>	63.01	65	Merck
La(NO <sub>3</sub> ) <sub>3</sub> ·6H <sub>2</sub> O	433.02	≥99	Fluka
NH <sub>4</sub> OH	35.05	25	Merck
Sr(NO <sub>3</sub> ) <sub>2</sub>	211.63	≥99	Fluka

### 3.2 Synthesis of LSAF3728 and BSCF5582 perovskite powders by modified citrate method

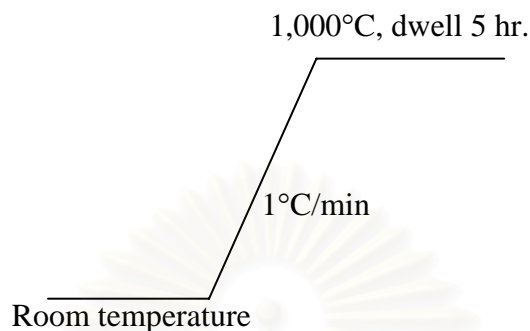
The perovskite powder of  $\text{La}_{0.3}\text{Sr}_{0.7}\text{Al}_{0.2}\text{Fe}_{0.8}\text{O}_{3-\delta}$  (LSAF3728) and  $\text{Ba}_{0.5}\text{Sr}_{0.5}\text{Co}_{0.8}\text{Fe}_{0.2}\text{O}_{3-\delta}$  (BSCF5582) were synthesized in basic solution. The preparation of powder was modified from the citrate pyrolysis method [42]. Stoichiometric amounts of corresponding high purity metal nitrates (based on 0.02 mole of perovskite powder) were partially dissolved in 10 ml ultra pure nitric acid (65%). Then citric acid with an amount of two times of the total metal ions was added. The mixture solution was titrated with  $\text{aq. NH}_3$  at the controlled rate of 2-3 ml/min. The pH of the solution was adjusted to 9.

The combustion of the homogeneous solution was carried out on a hot plate at around 200-300°C in a three-liter beaker covered with a fine sieve to prevent the loss of fine powder. The water was evaporated until a sticky gel was obtained. Then it became a large swelling viscous mass and finally self ignited by  $\text{NH}_4\text{NO}_3$ . The combustion lasted for about 10-20 seconds. The sponge-like solids expanded to occupy almost 2/3 of the beaker volume at the end. The powder of LSAF3728 was fired at 400°C for 2 hr. in furnace. The resulting powder was ground by mortar and calcined at 1,000–1,200°C with two different conditions (a) and (b) to achieve phase purity and remove the residual carbon. The conditions used for the calcination of the perovskite powders were set as follows:



**Scheme 3.1** The calcination conditions of LSAF3728 powder.

For the  $\text{Ba}_{0.5}\text{Sr}_{0.5}\text{Co}_{0.8}\text{Fe}_{0.2}\text{O}_{3.8}$  powder was calcined in the air at  $1,000^\circ\text{C}$  for 5 hr. with heating rates of  $1^\circ\text{C}/\text{min}$ .



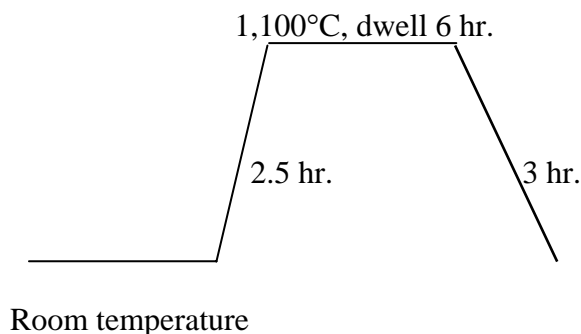
**Scheme 3.2** The calcination condition of BSCF5582 powder.

The particle was ground completely well by mortar before characterization.

### 3.3 Synthesis of LSCF6482 and LSC64 perovskite powders by solution method

The components of  $\text{La}_{0.6}\text{Sr}_{0.4}\text{Co}_{0.8}\text{Fe}_{0.2}\text{O}_{3.8}$  (LSCF6482) and  $\text{La}_{0.6}\text{Sr}_{0.4}\text{CoO}_{3.8}$  (LSC64) were synthesized by solution method.

The perovskite LSCF6482 powder was prepared by mixing an appropriate amount of  $\text{La}(\text{NO}_3)_3 \cdot 6\text{H}_2\text{O}$ ,  $\text{Sr}(\text{NO}_3)_2$ ,  $\text{Co}(\text{NO}_3)_2 \cdot 6\text{H}_2\text{O}$  and  $\text{Fe}(\text{NO}_3)_3 \cdot 9\text{H}_2\text{O}$  with distilled water. The mixture solution was stirred and heated on a hot plate around  $200^\circ\text{C}$  to evaporate water until sticky gel appeared. The heating temperature was increased to remove  $\text{NO}_x$  and the solid powder was obtained. Then it was heated at  $400^\circ\text{C}$  for 2 hr. in the furnace. The particle was ground completely well by mortar and calcined at  $1,100^\circ\text{C}$  for 6 hr. The calcined condition was shown in scheme 3.3. The powder of LSCF6482 and LSC64 were characterized by XRD.



**Scheme 3.3** The calcination condition of LSCF6482 powder.

### 3.4 Preparation of dual-phase perovskite

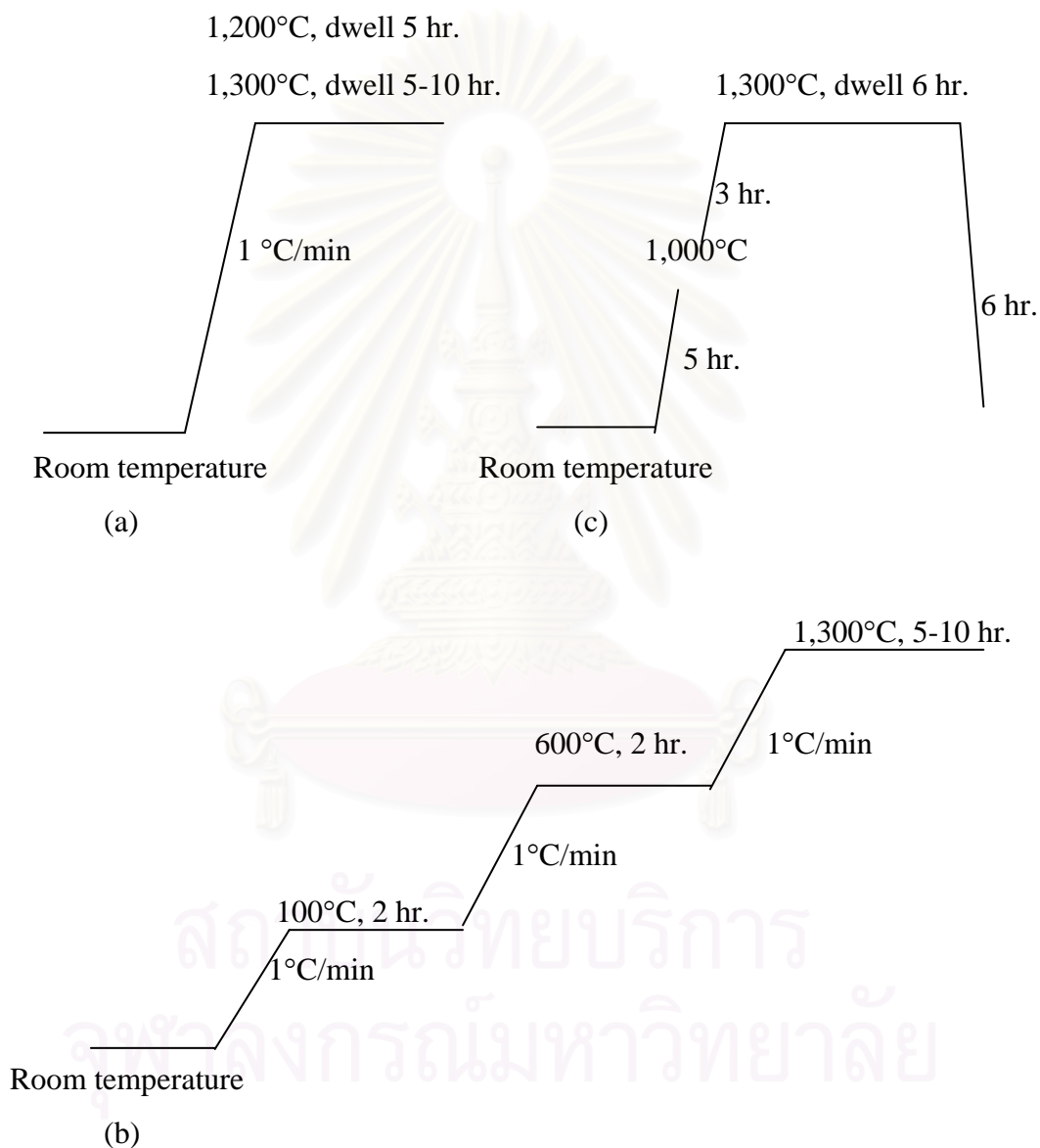
The  $\text{La}_{0.3}\text{Sr}_{0.7}\text{Al}_{0.2}\text{Fe}_{0.8}\text{O}_{3-\delta}$ - $\text{Ba}_{0.5}\text{Sr}_{0.5}\text{Co}_{0.8}\text{Fe}_{0.2}\text{O}_{3-\delta}$ ,  $\text{La}_{0.3}\text{Sr}_{0.7}\text{Al}_{0.2}\text{Fe}_{0.8}\text{O}_{3-\delta}$ - $\text{La}_{0.6}\text{Sr}_{0.4}\text{Co}_{0.8}\text{Fe}_{0.2}\text{O}_{3-\delta}$  and  $\text{La}_{0.3}\text{Sr}_{0.7}\text{Al}_{0.2}\text{Fe}_{0.8}\text{O}_{3-\delta}$ - $\text{La}_{0.6}\text{Sr}_{0.4}\text{CoO}_{3-\delta}$  dual-phase membranes (designated as LSAF-BSCF, LSAF-LSCF, LSAF-LSC, respectively) were prepared by mixing powders of each series of composite in the ratio 12:1, 12:2, 12:3 and 12:4 by weight. The mixing powder was ball-milled for 3 hr. in acetone medium and let it air-dried to evaporate acetone for 2 hr. The resulting powder was ground by mortar and then calcined at 1,000°C in a furnace. The condition used for the calcination of the mixing perovskite powder was set the same as calcined condition of LSAF3728.

### 3.5 Perovskite membrane preparation

The disc shape of dual-phase perovskites were formed by KBr die. The KBr die includes loading and pressing. The calcined perovskite powder was loaded into the cavity. The die having the perovskite powder inside was knocked against table for 2-3 times to evaporate the air inside the powder. After the die was completely assembled, the plunger was brought to the surface of the powder gently for final leveling and then rotates for smooth surface. About 1 ton was applied on the plunger by the uniaxial pressing machine. At the beginning of pressing, the pressure was slowly applied to 1 ton for 5 min. The pressure was released and then the die was removed from the press. Then the assembly was held while the press was slowly pumped until the pellet ejected.

### 3.6 The sintering of the perovskite oxides

The dual-phase perovskite membranes were generally sintered in air at 1,200-1,400°C. They were sintered under different conditions. The condition sintering of dual-phase membranes were set as follows:



**Scheme 3.4** The sintering conditions of dual-phase membranes.

### **3.7 Characterization of the perovskite oxides**

#### **3.7.1 X-ray diffractometry (XRD)**

The phase formation of perovskite powder, dual-phase perovskites were characterized after calcination and sintering by X-ray diffraction (XRD). The X-ray patterns, for both powder and membranes, were taken by using Rigaku, DMAX 2002 Ultima Plus X-Ray powder diffractometer equipped with a monochromator and a Cu-target X-ray tube (40 kV, 30 mA). The angles of  $2\theta$  ranged from 20-70 degree (step time 0.5 s., scan step 0.020 degree) at Department of Chemistry, Faculty of Science, Chulalongkorn University.

#### **3.7.2 Scanning electron microscopy (SEM) and Energy Dispersive X-ray (EDX) technique**

The morphology of the dual-phase membranes were carried out using a JEOL JSM-5800LV scanning electron microscopy, Oxford Instrument (Link ISIS series 300) at the Scientific and Technological Research Equipment Center (STREC), Chulalongkorn University. This instrument uses X-rays or electrons scattered back from the surface “illuminated” by a restored electron beam to generate an image with remarkable three-dimensional qualities. Specimens were sputtering coated with gold to reduce charge effects.

EDX analysis was used to determine the elements in dual-phase membrane. This technique is used in conjunction with SEM.

#### **3.7.3 Thermogravimetric analysis (TGA)**

Thermogravimetric analysis (TGA) was performed on TA instrument thermogravimetric analyzer (SDT 2960) at Department of Chemistry, Faculty of Science, Mahidol University. The powder specimens were used to heat up from room temperature to 1,000°C. TGA was performed under N<sub>2</sub> atmosphere, heating rate of 20 °C/min. The weigh loss indicates the desorbed oxygen from the lattice. In this



experiment, the perovskite membranes which were grounded into fine powder (particle size  $\leq$  200 mesh).

#### **3.7.4 Temperature-programmed desorption (TPD)**

Desorption of  $O_2$  were measured by Oxygen Temperature Programmed Desorption ( $O_2$ -TPD), at Department of Chemistry, Faculty of Science, Chulalongkorn University. Oxygen desorption capacity of the samples was studied as follows. About 100 mg of sample was loaded in a U-shape quartz tube. Helium was used as the carrier gas with a flow rate of 40 ml/min. The perovskite powder was pretreated at 900°C for 0.5 hr., then cooled to 100°C, after which adsorption of gas was performed in a flow of 99.99%  $O_2$  for 30 min. The powder was maintained at 100°C in He flow for another 0.5 hr. to eliminate physically adsorbed  $O_2$ . The temperature increased from 100°C to 900°C at a rate of 10°C/min. TCD was used on line with a computer data acquisition system.

## CHAPTER IV

### RESULTS AND DISCUSSIONS

In this thesis the preparation and oxygen permeation of dual-phase perovskite membranes were studied. Each perovskite compound is indicated by the abbreviation using the initial letters of each metal in A and B sites sequentially, followed by the corresponding number which refers to the proportion of each metal in the compound. For examples,  $\text{La}_{0.3}\text{Sr}_{0.7}\text{Al}_{0.2}\text{Fe}_{0.8}\text{O}_{3-\delta}$  and  $\text{Ba}_{0.5}\text{Sr}_{0.5}\text{Co}_{0.8}\text{Fe}_{0.2}\text{O}_{3-\delta}$  are abbreviated as LSAF3728 and BSCF5582, respectively.

#### 4.1 Perovskite powder

##### 4.1.1 Synthesis of LSAF3728 and BSCF5582 perovskite powders by modified citrate method

Yaremchenko *et al.* [28] prepared  $\text{La}_{0.3}\text{Sr}_{0.7}\text{Fe}_{1-x}\text{Al}_x\text{O}_{3-\delta}$  perovskites by the glycine-nitrate process (GNP). This method used the molar glycine/nitrate ratio equal to 2.0. The LSAF3728 powder was annealed at 1,300°C for 5 hr. The XRD pattern exhibited single-phase of cubic structure.

In this thesis, LSAF3728 was synthesized by modified citrate method; the metal nitrates were dissolved in 65% nitric acid, which then reacted with citric acid to form metal-citrate-nitrate complexes. These metal-citrate complexes can undergo polymerization when liquid ammonia was added. Meanwhile aq.NH<sub>3</sub> was added, the white fume of NH<sub>4</sub>NO<sub>3</sub> was suddenly observed, which came from the free NO<sub>3</sub><sup>-</sup> reacting with NH<sub>3</sub>·H<sub>2</sub>O and generated the heat. In the case of LSAF3728 the colour of the mixture had been changed from brown to yellow at pH ≈ 2 and the fume stopped at pH ≈ 2. At this point, the remained citric acid and NH<sub>4</sub>NO<sub>3</sub> might dissolve in the solution due to the adding of aq.NH<sub>3</sub> (10 ml). Then the solution is clear green (pH ≈ 3.5) and precipitated later. The precipitation indicated the metal citrate-nitrate gel resulting from the polymerization of the metal citrate-nitrate complex when aq.NH<sub>3</sub> was increased. Then the solution changed from clear deep green to clear brown solution (pH ≈ 9).

The combustion of the metal citrate-nitrate gel solution was composed of three steps: evaporation, decomposition, and spontaneous combustion. The excess solvent was firstly evaporated until a sticky gel was obtained. During the final stage of evaporation, the mixture began to swell, and became viscous. The generated gases can be observed from the large swelling viscous mass. Finally, at around 250°C the spontaneous combustion was initiated to convert the mixture into the powder. A typical burning of 40 ml of gel solution was completed within 20-30 seconds. Phase formation of LSAF3728 was characterized by X-ray diffraction.

The single-phase perovskite with cubic structure shows the diffraction line at the reflective planes 100, 110, 111, 200, 210, 211 and 220. The presence of the splitting peaks exhibit the distortion from the cubic structure and the appearance of diffraction lines other than those will be due to the other compound or secondary phase.

XRD pattern of LSAF3728 powder calcined at different conditions (Scheme 3.1) were shown in Figure 4.1. The effect of calcination conditions on phase purity of LSAF3728 was observed.

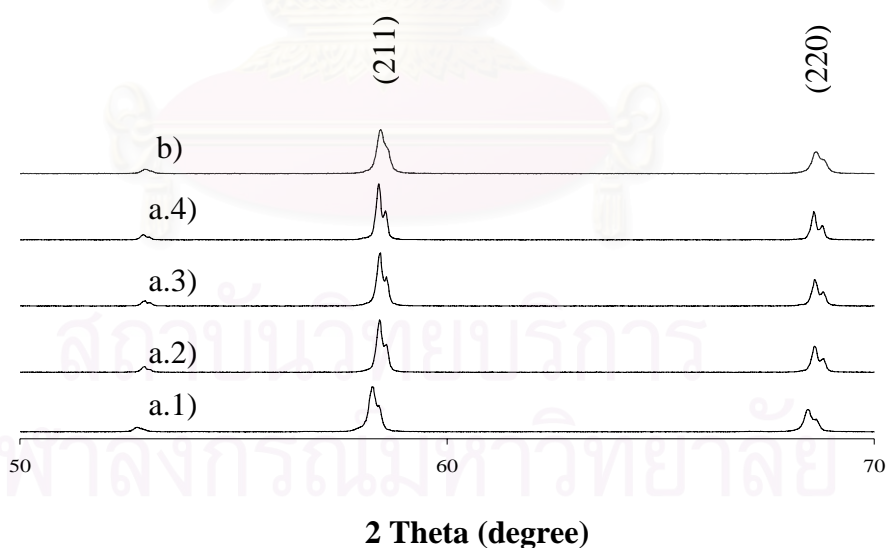


**Figure 4.1** XRD patterns of LSAF3728 after calcined under conditions (a); a.1) 1,000°C, 5 hr., a.2) 1,000°C, 10 hr., a.3) 1,100°C, 5 hr. a.4) 1,200°C, 5 hr. and calcined under condition (b) 1,000°C, 6 hr.

Figure 4.1 (a) reveals the phase structure of LSAF distorted from the cubic structure when the calcination temperature and time increased. But XRD pattern of the calcined powder under condition (b) shows the single peaks which indicate the pure phase of perovskite. Thus, the calcination condition at temperature 1,000°C for 6 hr. was applied for preparation of dual-phase perovskite membranes.

In the case of BSCF5582, the XRD pattern of the powder after calcination at 1,000°C for 5 hr. was illustrated in Figure 4.2.

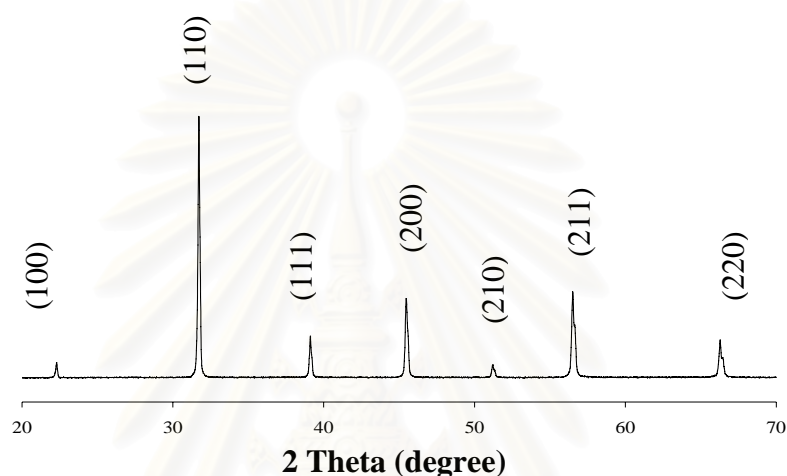


**Figure 4.2** XRD pattern of BSCF5582 perovskite powder.

The XRD pattern of BSCF5582 shows a cubic structure which reveals the diffraction line at the reflective planes 100, 110, 111, 200, 210, 211 and 220. No secondary phase was observed.

#### **4.1.2 Synthesis of LSCF6482 and LSC64 perovskites powder by solution method**

The metal nitrates were dissolved in distilled water. The clearly solution heated at 300°C until a sticky gel was obtained. During the evaporation, the mixture became viscous and the oxide started to form. The NO<sub>x</sub> gas was generated for 10 min. The black powder was observed after calcination at 1100°C for 6 hr. The powder of LSCF6482 and LSC64 were characterized by XRD.

The XRD patterns of LSCF6482 and LSC64 powder after calcination were shown in Figures 4.3-4.4.

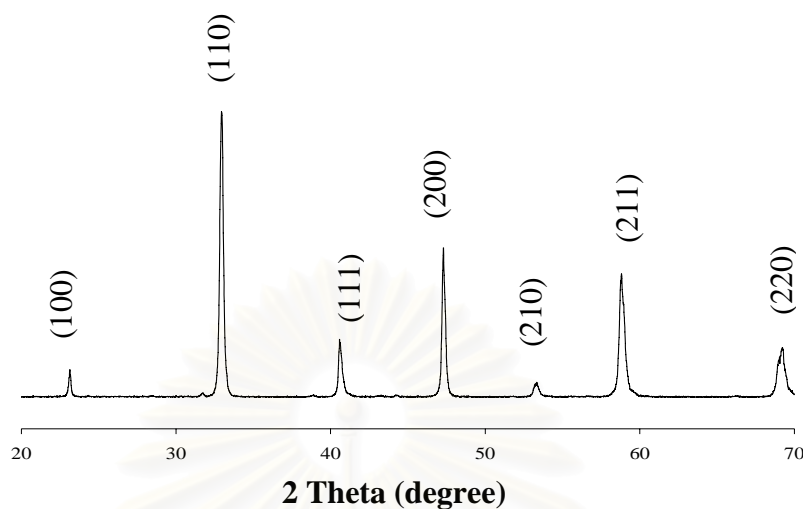


**Figure 4.3** XRD pattern of LSCF6482 perovskite compound.

For LSCF6482, XRD pattern was shown in Figures 4.3. This figure exhibited the diffraction line at the reflective planes 100, 110, 111, 200, 210, 211 and 220. Thus diffraction peak indicates the cubic structure of single phase perovskite.

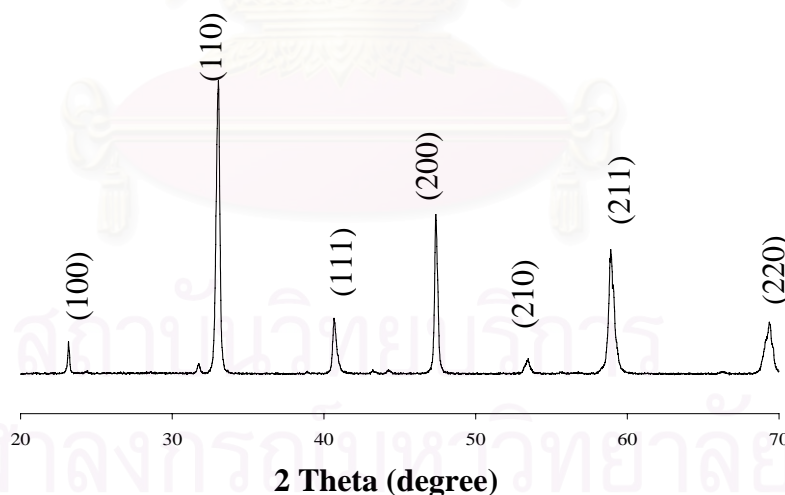


**Figure 4.4** XRD pattern of LSC64 perovskite compound.

The XRD pattern of LSC64 powder with a cubic structure exhibited the diffraction line at the reflective planes 100, 110, 111, 200, 210, 211 and 220.

## 4.2 Characterization of dual-phase perovskite compounds

The LSAF-BSCF, LSAF-LSCF, and LSAF-LSC dual-phase perovskites were prepared from the mixture powder in ratio 12:1, 12:2, 12:3 and 12:4 by weight, respectively. The mixing powder was ball-milled for 3 hr. The powder was annealed at 1,000°C, 6 hr. All of dual-phase perovskite membranes after sintering preserve good integrity with no fracture.

The XRD was used for characterization the phase formation of dual-phase perovskite. The morphologies of all dual-phase perovskite membranes sintered at different times and temperatures were examined by SEM.

### 4.2.1 X-ray diffraction (XRD)

The phase formation of dual-phase perovskites were indicated by XRD. The lattice parameter of synthesized perovskites and dual-phase perovskite was calculated by XRD software.

#### 4.2.1.1 Phase formation of dual-phase perovskite powder

##### A. The LSAF-BSCF dual-phase perovskite powder

The XRD patterns of LSAF-BSCF dual-phase perovskite powder after calcination was compared with those of LSAF3728 and BSCF5582 powder, as shown in Figure 4.5. Basically, the XRD pattern of single-phase perovskite with a cubic structure exhibited the diffraction line at the refractive planes 100, 110, 111, 200, 210, 211 and 220. The pure phases of LSAF3728 and BSCF5582 exhibited the same cubic structure but XRD peaks in different two theta values because of the difference in lattice parameter, shown in Table 4.1.

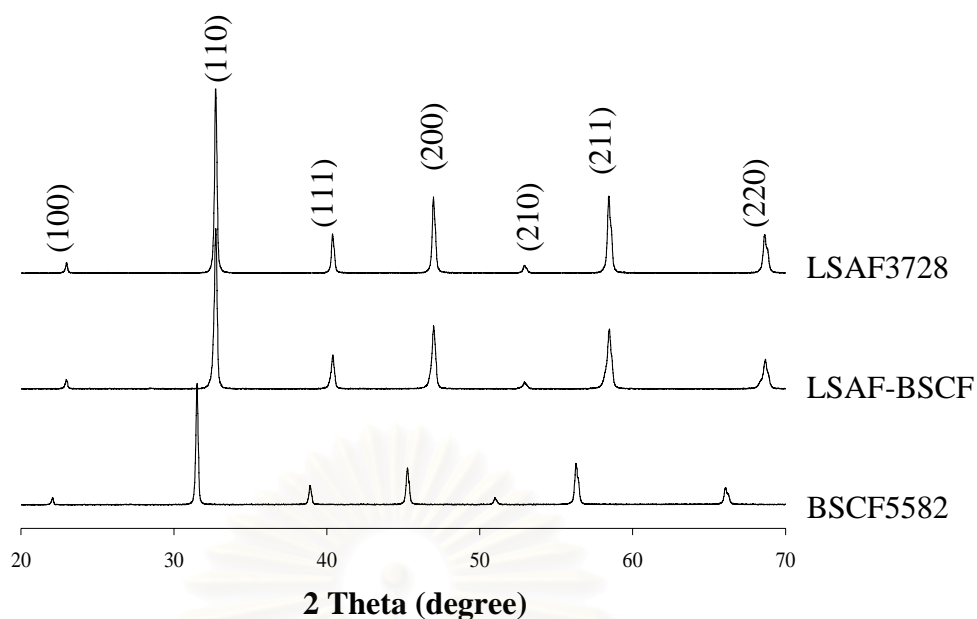


**Figure 4.5** XRD patterns of pure LSAF3728, pure BSCF5582 and dual-phase perovskite powder of LSAF-BSCF with ratio 12:1 by weight.

The XRD data of LSAF-BSCF dual-phase perovskite powder with ratio 12:1 by weight shows the cubic structure with a lattice parameter ( $3.8647 \text{ \AA}$ ) which is the same as that for the pure LSAF3728 phase.

**Table 4.1** Lattice parameters of LSAF-BSCF dual-phase perovskite powder and pure phase of LSAF and BSCF

Compounds	Crystal system	a ( $\text{\AA}$ )
LSAF3728	Cubic	3.8658
LSAF-BSCF	Cubic	3.8647
BSCF5582	Cubic	3.9874

From XRD peak of LSAF-BSCF dual-phase, there are no visible XRD peaks obtained from the BSCF phase due to the small amount of BSCF phase in the dual-phase perovskite. Therefore we used EDX for analyzing all elements which were contained in dual-phase perovskite membrane.

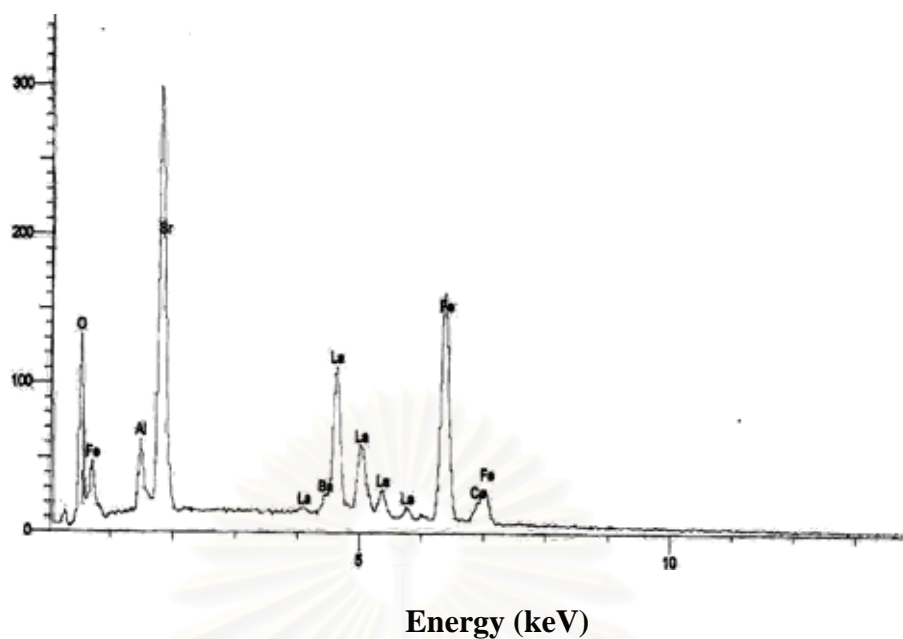


**Figure 4.6** The EDX pattern of LSAF-BSCF dual-phase membrane with ratio 12:1 by weight.

The EDX analysis (Figure 4.6) shows the elements of O, La, Sr, Al, Fe, Ba and Co. It is confirmed that the BSCF was contained in LSAF-BSCF dual-phase perovskite membrane.

### **B. The LSAF-LSCF dual-phase perovskite powder**

Phase formation of LSAF-LSCF with ratio 12:1 by weight is shown in Figure 4.7 compared with the pure phase of LSAF3728 and LSCF6482. The patterns exhibited the diffraction line at the miller indices 100, 110, 111, 200, 210, 211 and 220. The diffraction peak indicates the cubic structure of perovskite.



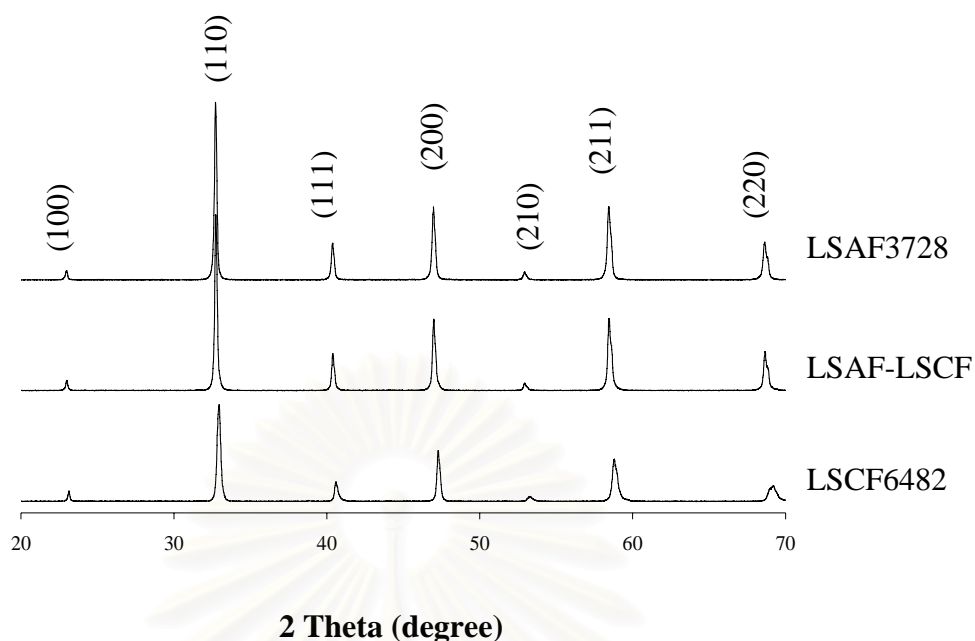


**Figure 4.7** XRD patterns of pure LSAF3728, pure LSCF6482 and dual-phase perovskite powder of LSAF-LSCF with ratio 12:1 by weight.

From Figure 4.7, the XRD peak of LSCF6482 did not appear in XRD pattern of LSAF-LSCF dual-phase because the dual-phase had a small content of LSCF6482.

**Table 4.2** Lattice parameters of LSAF-LSCF dual-phase perovskite powder and pure phase of LSCF and LSCF

Compounds	Crystal system	a (Å)
LSAF3728	Cubic	3.8658
LSAF-LSCF	Cubic	3.8648
LSCF6482	Cubic	3.8418

Table 4.2 lists the lattice parameters of pure LSAF3728, LSCF6482 and LSAF-LSCF dual-phase perovskite powder with ratio 12:1 by weight. This dual-phase reveals cubic structure which its lattice parameter is almost the same as that of pure LSAF3728. It indicates that LSCF can diffuse easily into LSAF domain because of similar composite materials.

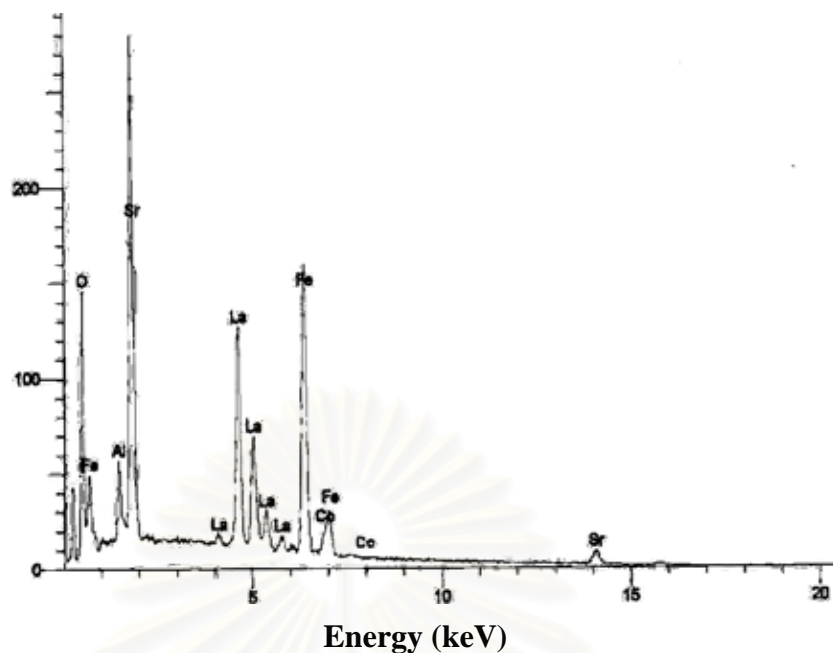


**Figure 4.8** The EDX pattern of LSAF-LSCF dual-phase membrane with ratio 12:1 by weight.

In EDX analysis, the Co element was presented in Figure 4.8 which confirming the elements of pure LSCF phase mixed in dual-phase of LSAF-LSCF perovskite membrane.

### C. The LSAF-LSC dual-phase perovskite powder

Figure 4.9 shows XRD patterns of pure LSAF3728, pure LSC64 and dual-phase perovskite powder of LSAF-LSC with ratio 12:1 by weight. The phase formation of LSAF-LSC dual-phase exhibited the cubic structure with lattice parameter of 3.8628 Å, listed in Table 4.3. The parameter is somewhat the same as that for the pure LSAF3728.

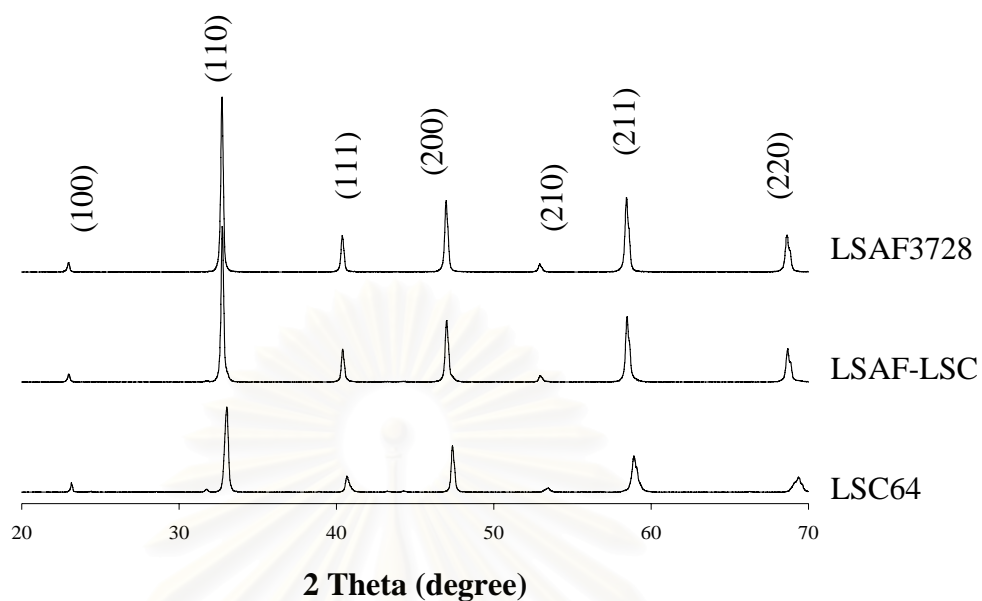


**Figure 4.9** XRD patterns of pure LSAF3728, pure LSC64 and dual-phase perovskite powder of LSAF-LSC with ratio 12:1 by weight.

**Table 4.3** Lattice parameters of LSAF-LSC dual-phase perovskite powder and pure phase of LSAF and LSC

Compounds	Crystal system	a (Å)
LSAF3728	Cubic	3.8658
LSAF-LSC	Cubic	3.8628
LSC64	Cubic	3.8334

From the XRD results, the phase formation of calcined powder of dual-phase perovskites indicated the same cubic structure of pure LSAF3728 perovskite. The lattice parameter of dual-phase did not change when doped LSAF3728 with BSCF5582, LSCF6428 and LSC64.

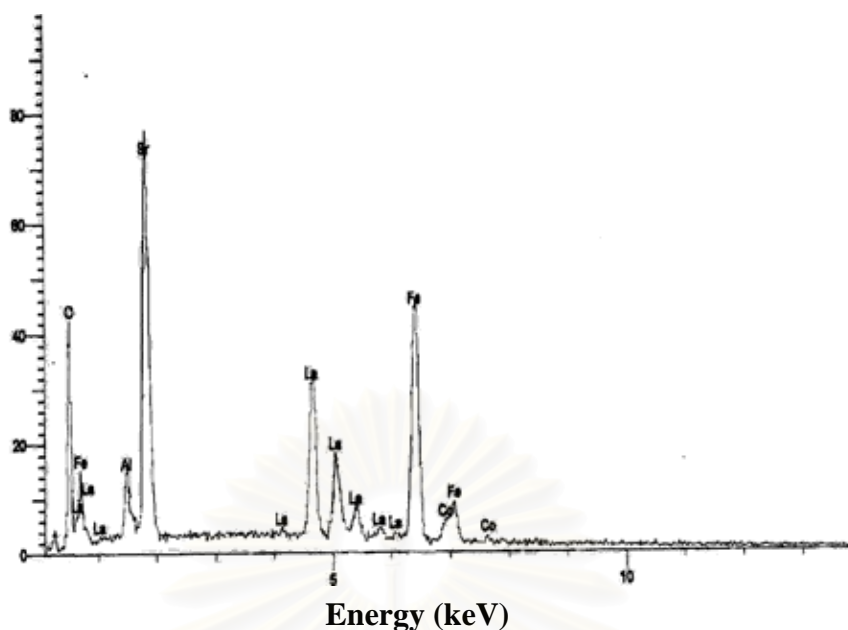


**Figure 4.10** The EDX pattern of LSAF-BSCF dual-phase membrane with ratio 12:1 by weight.

The EDX analysis (Figure 4.6) shows the elements of O, La, Sr, Al, Fe and Co in dual-phase membrane, confirming that the LSC phase was contained in the dual-phase.

#### 4.2.1.2 The effect of calcination and sintering on dual-phase perovskite membranes

##### A. The variation of BSCF5582 contents in LSAF-BSCF dual-phase perovskite

The phase formation of variation of BSCF5582 contents in dual-phase perovskites after calcined at 1,000°C, 6 hr. and sintered at 1,400°C, 6 hr. were shown in Figures 4.11-4.12.

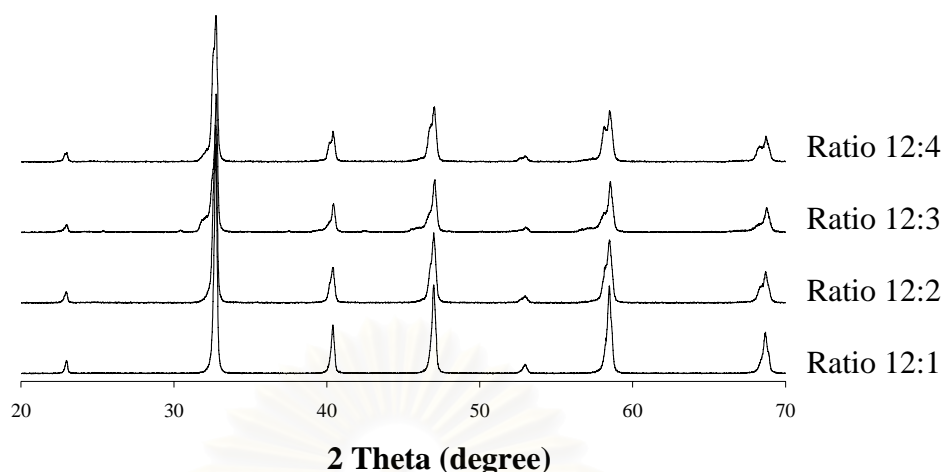


**Figure 4.11** XRD patterns of LSAF-BSCF dual-phase perovskites in various ratios after calcined at 1,000°C, 6 hr.

Figure 4.11 showed XRD patterns of the LSAF-BSCF dual-phase perovskite calcined at 1,000°C, 6 hr. The XRD patterns of LSAF-BSCF dual-phase with cubic structure exhibit the diffraction line at the reflective planes 100, 110, 111, 200, 210 and 211. As the BSCF composition increased, the diffraction peak ( $2\theta = 69$ ) becomes broad which indicated one single perovskite phase with a cubic distortion. The dual-phase of LSAF-BSCF was sintered at 1,400°C and phase formation was characterized by XRD. The results are shown in Figure 4.12.

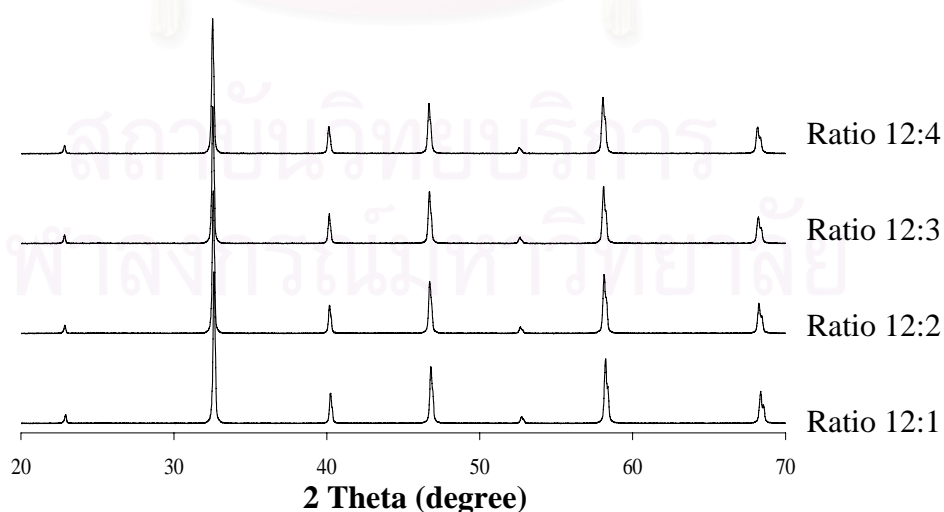


**Figure 4.12** XRD patterns of LSAF3728-BSCF5582 dual-phase perovskite membranes in various ratios after sintering at 1,400°C, 6 hr.

After sintering at 1,400°C, XRD pattern of all of these dual-phase exhibit the phase structure of cubic perovskite. This suggests that the interaction at high temperature causes more diffusion of barium and cobalt cation into LSAF matrix. It is confirmed by the increasing of lattice parameters of dual-phase after sintering (Table 4.4).

**Table 4.4** Lattice parameter of LSAF-BSCF dual-phase perovskite

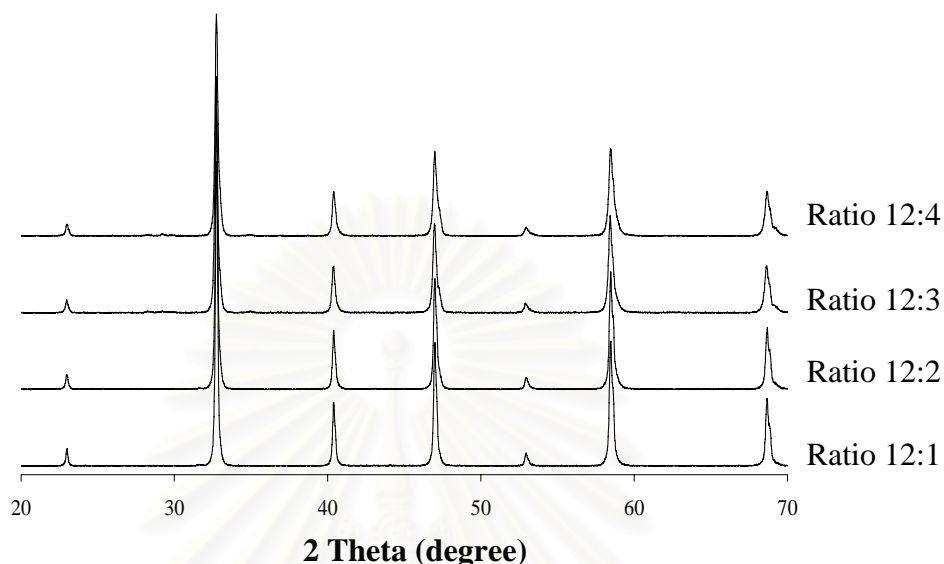
Ratio LSAF:BSCF (by weight)	Crystal system	Lattice parameters a (Å)	
		After calcinations at 1,000°C	After sintering at 1,400°C
12:1	Cubic	3.8647	3.8805
12:2	Cubic	3.8642	3.8876
12:3	Cubic	3.8617	3.8856
12:4	Cubic	3.8616	3.8859

Table 4.4 lists both crystal system and lattice parameters of LSAF-BSCF dual-phase perovskite with various ratios after calcinations and sintering. The unit cell values of powder after calcined and sintered did not change with the increasing of the amount of BSCF5582. The lattice parameter increased after sintering. This result demonstrated that BSCF5582 phase merged with LSAF3728. There are two reasons to explain this result. 1) It might be the substitution of Ba for La and Sr in A-site because the ionic radius of  $Ba^{2+}$  larger than ionic radius of  $La^{3+}$  and  $Sr^{2+}$  ( $r_{Ba^{2+}} = 1.66$  Å,  $r_{La^{3+}} = 1.36$  Å,  $r_{Sr^{2+}} = 1.44$  Å). 2) The ionic radius of  $Co^{3+} = 0.75$  Å is larger than ionic radius of  $Al^{3+} = 0.54$  Å, ionic radius of  $Fe^{3+} = 0.55$  Å [50]. The substitution of Co for Al in B-site of  $ABO_3$  might lead to the larger lattice parameter.

#### **B. The variation of LSCF6482 contents in LSAF-LSCF dual-phase perovskite**

The XRD patterns of LSAF-LSCF dual-phase with ratio 12:1, 12:2, 12:3 and 12:4 by weight after calcined at 1,000°C, 6 hr. are presented in Figure 4.13. This result showed cubic perovskite structure of the composite even though the ratio of

LSAF-LSCF increased from 12:1 to 12:4. It shows that LSCF can diffuse completely into LSAF cubic structure. The lattice parameter did not change when the contents of LSCF6482 varied (see Table 4.5).



**Figure 4.13** XRD pattern of LSAF-LSCF dual-phase perovskite in various ratios after calcined at 1,000°C, 6 hr.

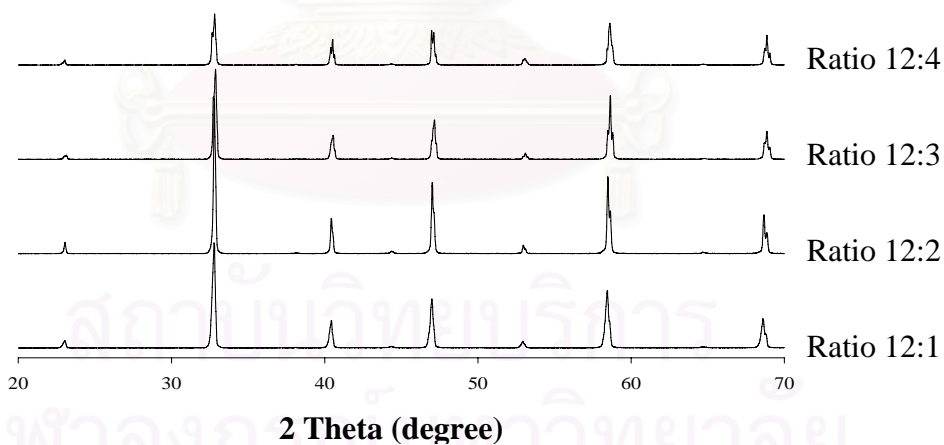


**Figure 4.14** XRD patterns of LSAF3728-LSCF6482 dual-phase perovskite membranes in various ratios after sintering at 1,400°C, 6 hr.

Figure 4.14 shows XRD pattern of dual-phase perovskite membranes in various ratios after sintered at 1,400°C. All patterns reveal the cubic structure. The unit cell parameters listed in Table 4.5 show that the lattice parameters of sintered membranes barely changed as compared to those of membranes before sintering. It

can be explained that the phase interaction between LSAF and LSCF occurred completely after calcination.

**Table 4.5** Lattice parameter of LSAF-LSCF dual-phase perovskite

Ratio LSAF:LSCF (by weight)	Crystal system	Lattice parameter a (Å)	
		After calcinations at 1,000°C	After sintering at 1,400°C
12:1	Cubic	3.8648	3.8699
12:2	Cubic	3.8640	3.8668
12:3	Cubic	3.8640	3.8613
12:4	Cubic	3.8637	3.8628

Also, it is demonstrated that the structure is stable after sintering at high temperature. It is suggested that the partial substitution at B site has less effect to the structure.

### C. The variation of LSC64 content in LSAF-LSC dual-phase perovskite

The characteristic XRD patterns of the LSAF-LSC dual-phase perovskite after calcination and sintering are shown in Figure 4.15-4.16.

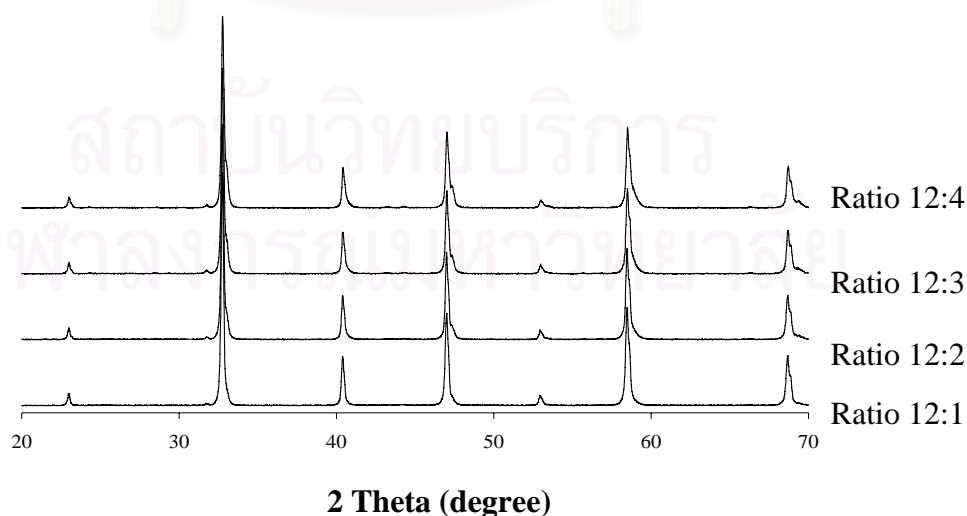


**Figure 4.15** XRD pattern of LSAF-LSC dual-phase perovskite in various ratios after calcined at 1,000°C, 6 hr.



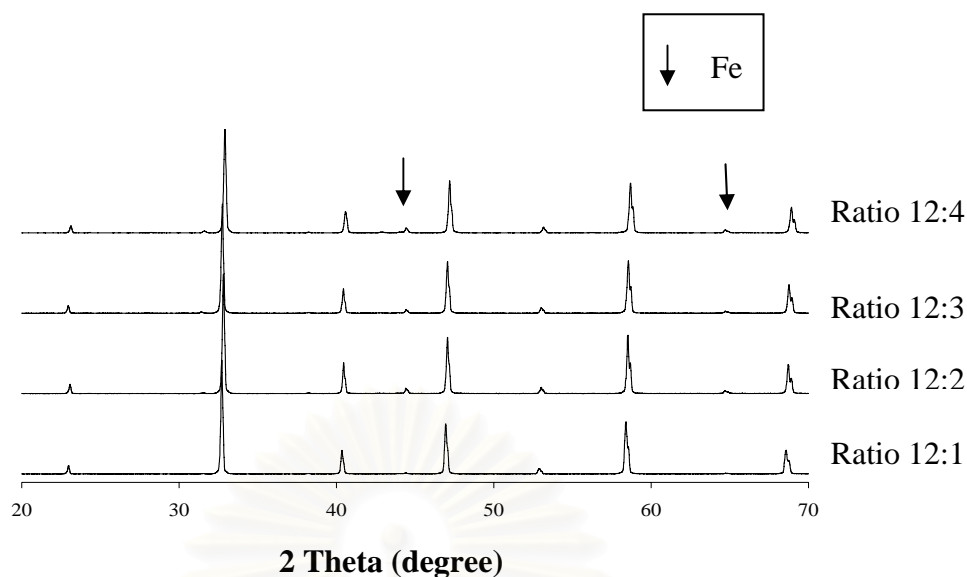


**Figure 4.16** XRD patterns of LSAF3728-LSC64 dual-phase perovskite membranes in various ratios after sintering at 1,400°C, 6 hr.

According to Figures 4.15, 4.16 and Table 4.6, the LSAF-LSC dual-phase with ratios 12:1, 12:2, 12:3 and 12:4, calcined at 1,000°C showed a single phase of perovskite cubic structure with no significant change of lattice parameters. For dual-phase perovskite membrane with ratio 12:4 after sintered at 1,400°C, (Figure 4.12), the secondary phase of Fe(0) (marked with ↓) (JCPDS-database: 99-0064) was observed.

**Table 4.6** Lattice parameter of LSAF-LSC dual-phase perovskite

Ratio LSAF:LSC (by weight)	Crystal system	Lattice parameter a (Å)	
		After calcination at 1,000°C	After sintering at 1,400°C
12:1	Cubic	3.8628	3.8677
12:2	Cubic	3.8622	3.8572
12:3	Cubic	3.8618	3.8514
12:4	Cubic	3.8615	3.8469

The lattice parameters are shown in Table 4.6. The unit cell data of the dual-phase perovskites before and after sintering at 1,400°C decrease with the increasing of LSC64 contents as well as the amount of the secondary phase of Fe. The presence of

LSC dispersed in LSAF matrix caused that the LSAF-LSC membranes undergo small change in composition. Thus the structure of LSAF-LSC can be stabilized by iron.

#### **4.2.2 Scanning electron microscope (SEM)**

The morphologies of all dual-phase perovskite membranes after sintered at different conditions were examined by SEM.

##### **4.2.2.1 Effect of setting temperature program of sintering on the morphology of LSAF-BSCF dual-phase perovskite membranes**

To attain dense membrane, the compacting perovskite powder and setting temperature program of sintering were concerned. The dual-phase perovskite membranes were sintered at different setting temperature program mentioned in the previous section, Scheme 3.4. The different setting temperature programs refer to sintering rate of heating up to target sintering temperature.

The surface of dual-phase membranes after sintering at different setting temperature program were investigated by SEM technique as presented in Figure 4.17.

From Figure 4.17 (a-c), the same temperature program was set with heating rate of about 1°C/min. The SEM pictures showed the grain size of dual-phase perovskite increased with the increasing of sintering temperature and sintering time. The particle was fused into large grain size at higher temperature. The dual-phase membranes were sintered at 1,300°C (setting temperature program see Scheme 3.4 b) which display in Figure 4.13 (d and e). The grain size of dual-phase perovskite increased with the increasing of sintering time. This condition indicated the larger grain size than membranes after sintered with heating rate 1°C/min. The grain size of membranes in Figure 4.17 (f) showed similar phenomena as Figure 4.17 (e). The membrane, Figure 4.17 (e), was taken longer sintering time than membrane in Figure 4.17 (f).

Due to three conditions differ in heat up to target temperature. The sintering conditions as Scheme 3.4 (a) and (b) were slowly heating up, it indicated the longer time for sintering. Therefore, the sintering condition as shown in Scheme 3.4 (c) is

suitable to obtain the dense dual-phase perovskite membranes. The condition in Scheme 3.4 (c) was applied for sintering of all dual-phase membranes.

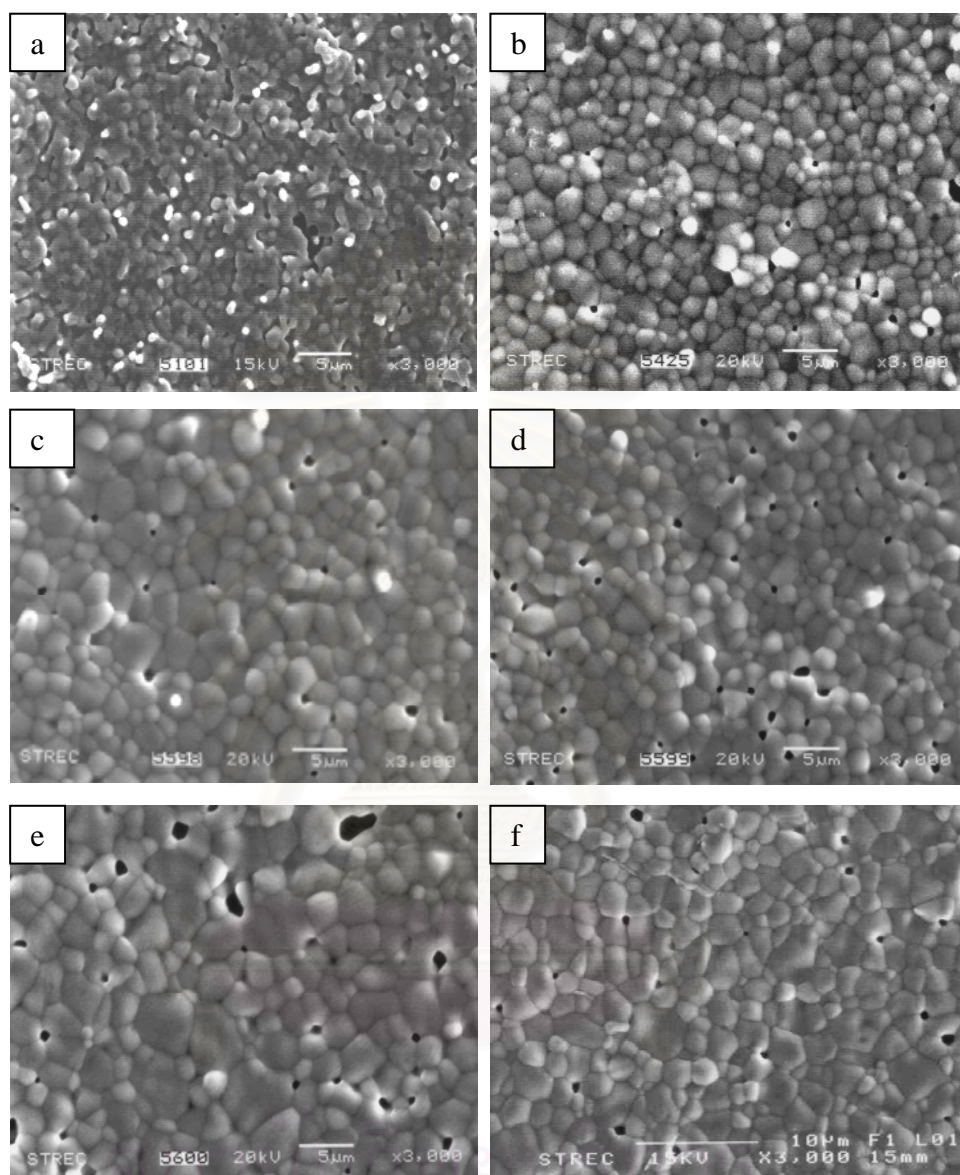


**Figure 4.17** SEM pictures of LSAF-BSCF dual-phase membranes after set temperature program see Scheme 3.4 a); membrane sintered at (a) 1,200°C, 5 hr., (b) 1,300°C, 5 hr., (c) 1,300°C, 10 hr., set temperature program see Scheme 3.4 b); membrane sintered at (d) 1,300°C, 5 hr., (e) 1,300°C, 10 hr., and set temperature program see Scheme 3.4 c); membrane sintered at (f) 1,300°C, 6 hr.

#### 4.2.2.2 The influence of sintering time and temperature on morphology of dual-phase perovskite membranes

##### A. The LSAF-BSCF dual-phase perovskite membranes

The morphologies of LSAF-BSCF membranes with ratio LSAF:BSCF = 12:1 by weight after sintered at 1,300°C, 6 hr., 1,300°C, 12 hr., 1,300°C, 18 hr. and 1,400°C, 6 hr. are shown in Figure 4.18.

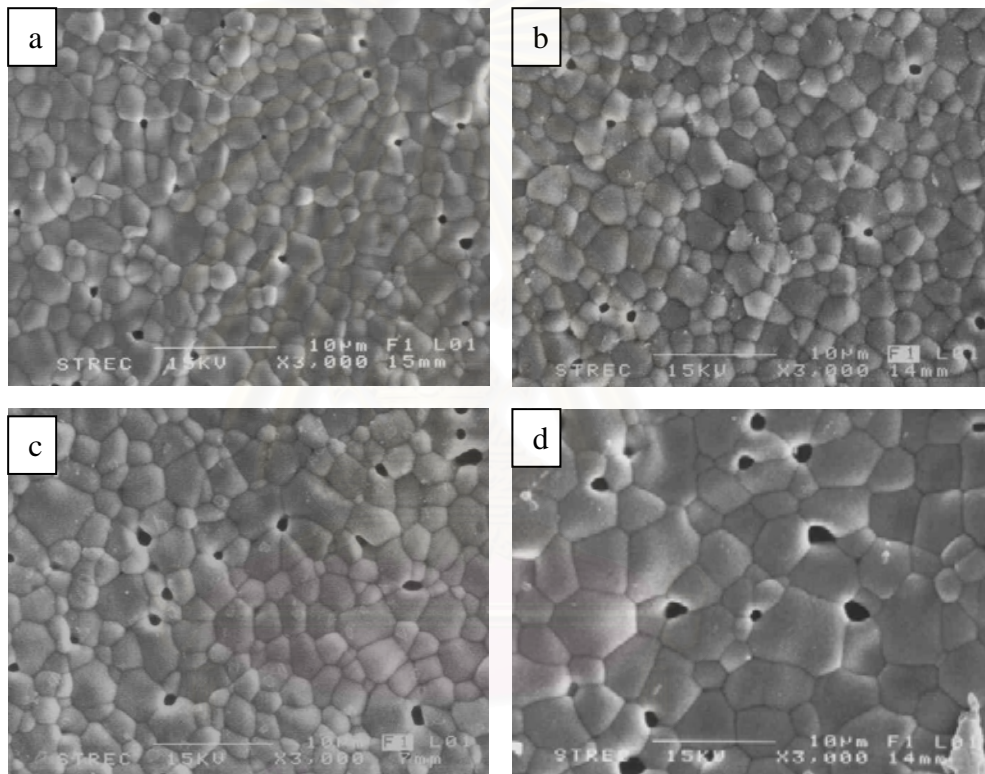


**Figure 4.18** SEM pictures of LSAF-BSCF with ratio 12:1 by weight after sintered at a) 1,300°C, 6 hr., b) 1,300°C, 12 hr., c) 1,300°C, 18 hr. and d) 1,400°C, 6 hr.

The grain size of dual-phase compound slightly increases with increasing of sintering time. The grain size after sintered at 1,400°C is larger than that of membrane after sintered 1,300°C. It might be due to the particle fuse together. It is concluded that the grain size increased with the increasing of sintering temperature.

## B. The LSAF-LSCF dual-phase perovskite membranes

Figure 4.19 display the surface of LSAF-LSCF dual-phase membranes with ratio 12:1 by weight after sintered at different time and temperature.

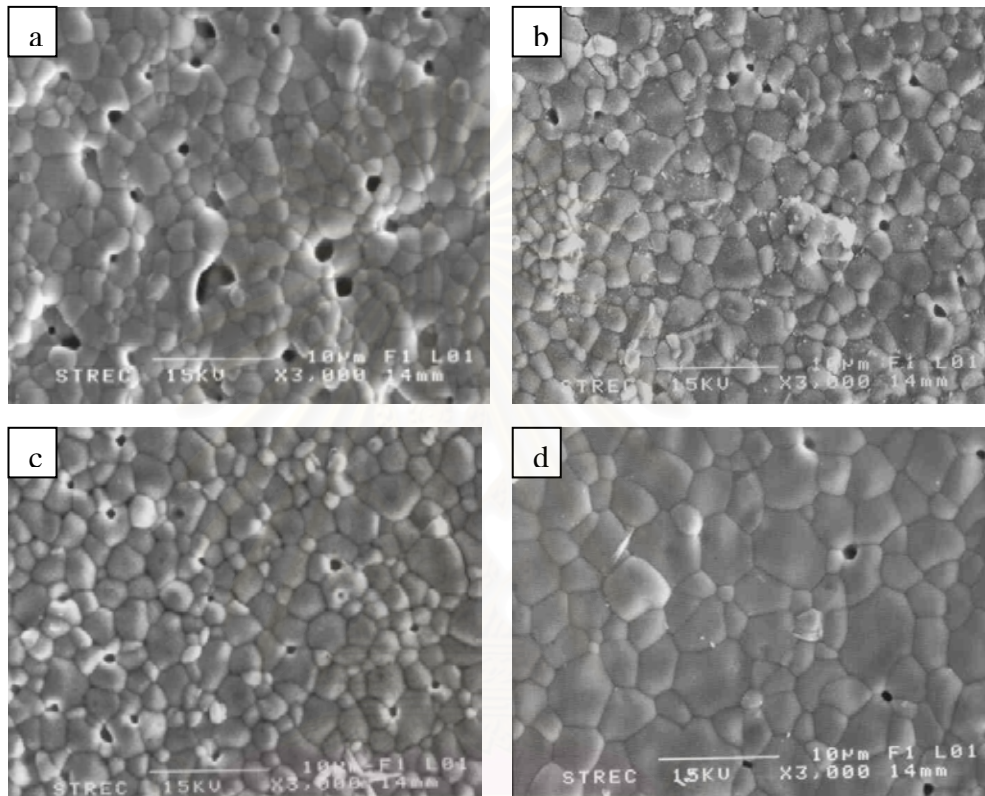


**Figure 4.19** SEM pictures of LSAF-LSCF with ratio 12:1 by weight after sintered at a) 1,300°C, 6 hr., b) 1,300°C, 12 hr., c) 1,300°C for 18 hr. and d) 1,400°C, 6 hr.

Figures 4.19 (a), 4.19 (b) and 4.19 (c) show the picture at 1,300°C that the grain size did not increase when the sintering time increase. From Figure 4.19 (d), the grain size of LSAF-LSCF membrane increased when sintering temperature increase to 1,400°C at shorter time (6 hr.). The dense membrane was obtained when membrane was heated up to 1,400°C.

### C. The LSAF-LSC dual-phase perovskite membranes

The dual-phase of LSAF-LSC membranes were investigated by SEM technique shown in Figure 4.20.

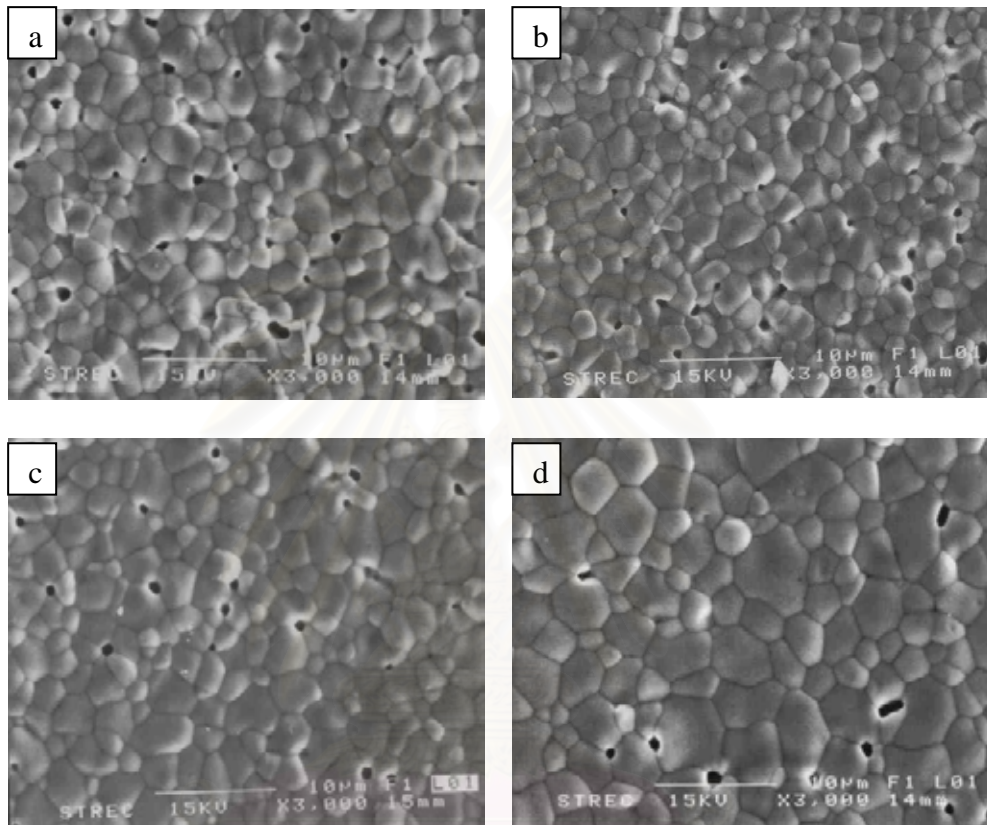


**Figure 4.20** SEM pictures of LSAF-LSC with ratio 12:1 by weight after sintered at a) 1,300°C, 6 hr., b) 1,300°C, 12 hr., c) 1,300°C, 18 hr. and d) 1,400°C, 6 hr.

The morphologies of membranes were considered when sintered at 1,300°C, 6 hr., 1,300°C, 12 hr., 1,300°C, 18 hr. and 1,400°C, 6 hr. The membranes were densified after sintered for a long time at 1,300°C, the porosity on surface decreased and grain size of membranes increases. The LSAF-LSC membrane after sintered at 1,400°C was acquired grain growth and dense membrane.

### 4.2.2.3 The effect of composition on morphology of dual-phase perovskite membranes

The morphologies of LSAF-BSCF, LSAF-LSCF and LSAF-LSC dual-phase membranes with various ratios were characterized by SEM technique. In this section, we considered the dual-phase membranes were sintered at 1,400°C for 6 hr.

#### A. The variation of BSCF5582 contents on morphology of LSAF-BSCF dual-phase membranes

SEM pictures in Figure 4.21, exhibited morphologies of variation of BSCF5582 in LSAF-BSCF membranes. The grain size of perovskite increased together with the increasing BSCF5582 contents. Therefore at the same sintering temperature, the size of grains in dual-phase with ratio 12:4 was larger than ratio 12:3, ratio 12:2 and ratio 12:1 by weight, respectively.

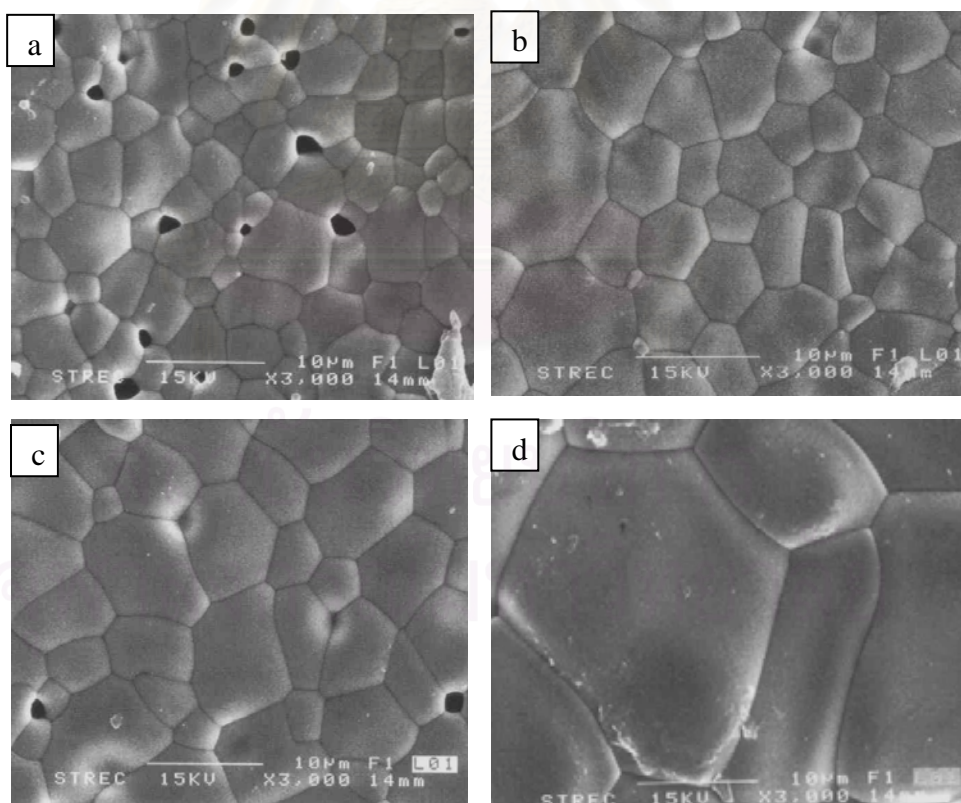


**Figure 4.21** SEM pictures of LSAF-BSCF membranes with ratio a) 12:1, b) 12:2, c) 12:3 and d) 12:4 by weight

## B. The variation of LSCF6482 contents on morphology of LSAF-LSCF dual-phase membranes

The morphology of membranes after sintered at 1,400°C for 6 hr. was considered when varies LSCF6482 content, as shown in Figure 4.22.

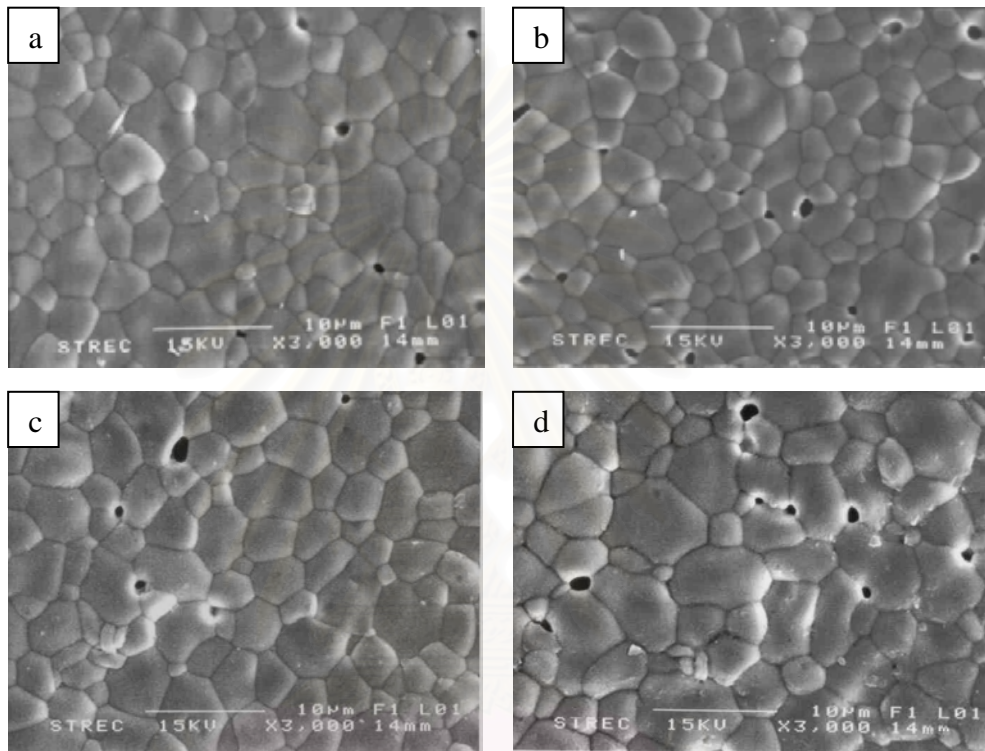


**Figure 4.22** SEM pictures of LSAF-LSCF membranes with ratio a) 12:1, b) 12:2, c) 12:3 and d) 12:4 by weight

From Figure 4.22, the grain size slightly increased with an increasing content of LSCF6482. Therefore the LSCF6482 contents did not affect on morphology of the dual-phase membranes.



### C. The variation of LSC64 contents on morphology of LSAF-LSC dual-phase membranes

Figure 4.23 shows that the morphologies of LSAF-LSC dual-phase membranes with various ratios, 12:1, 12:2, 12:3 and 12:4 by weight, respectively.

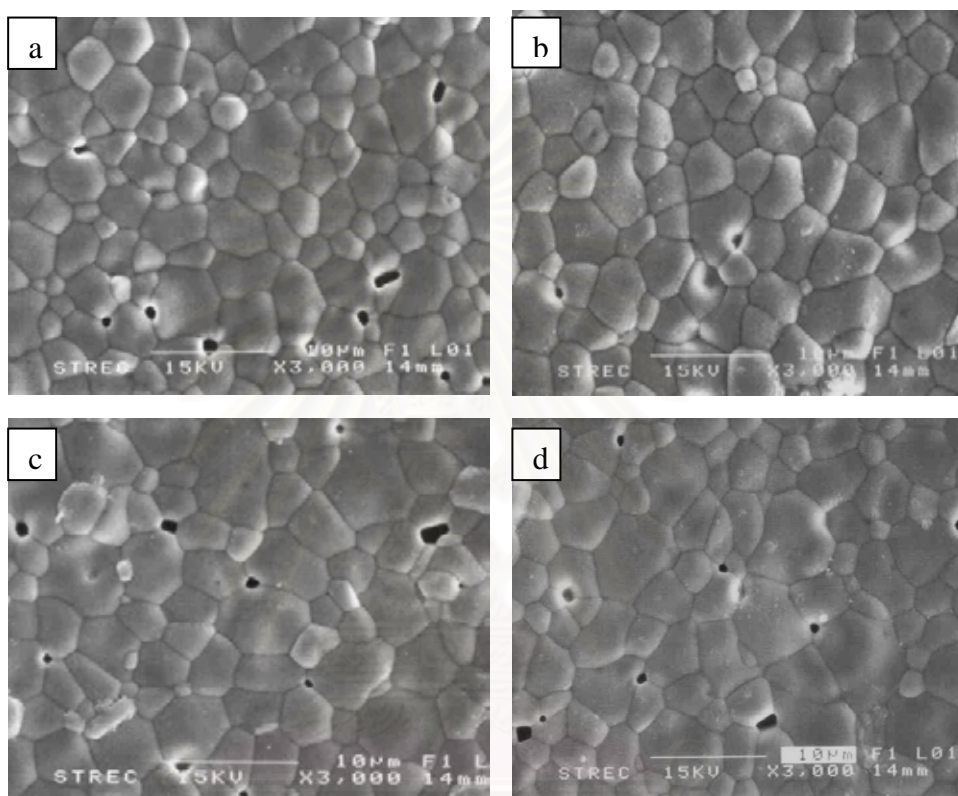


**Figure 4.23** SEM pictures of LSAF-LSC membranes with ratio a) 12:1, b) 12:2, c) 12:3 and d) 12:4 by weight

The LSC64 contents in LSAF-LSC system affected on the grain size of membrane after sintering at 1,400°C for 6 hr. The grain size increased with the increasing of LSC64 contents. Therefore the LSAF-LSCF dual-phase perovskite membrane with ratio 12:4 by weight exhibited the largest grain size in their series.

### 4.3 Oxygen desorption of perovskite compounds

Oxygen desorption of the dual-phase perovskite compounds were analyzed by TGA and O<sub>2</sub>-TPD technique.

#### 4.3.1 Thermogravimetric analysis (TGA)

The amount of oxygen was desorbed during the thermogravimetric analysis. A notable TGA data is weight change (%) which corresponds to oxygen vacancy concentration. The oxygen vacancy concentration indicated that oxygen desorption relate to oxygen permeation in perovskite compound [43, 44]. The TGA profile of LSAF3728 powder after sintered at 1,400°C is given in Figure 4.24.

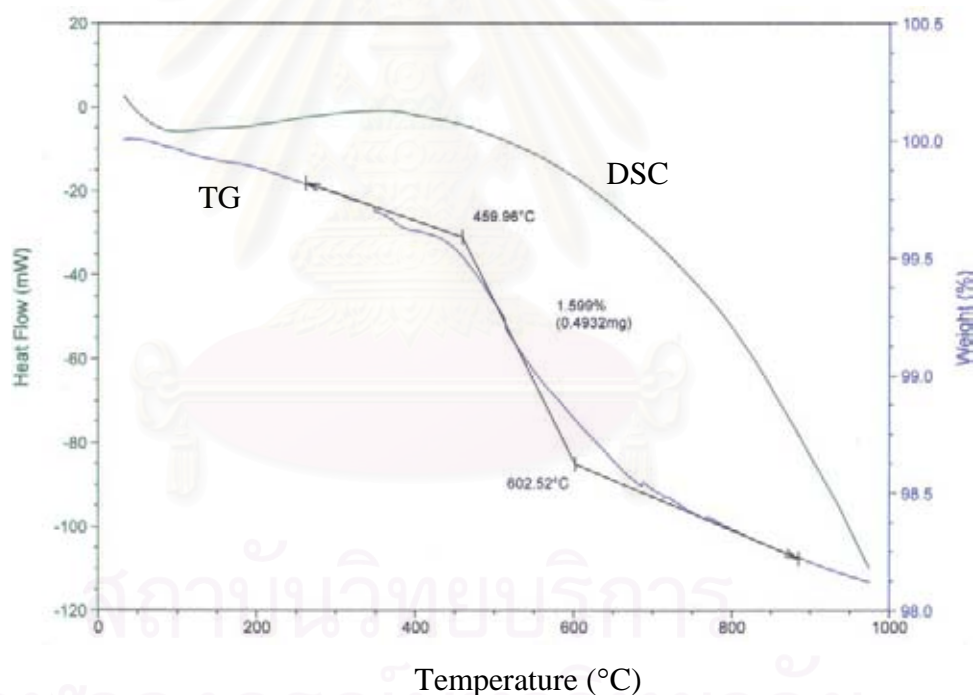


**Figure 4.24** TG-DSC profiles of LSAF3728 perovskite

It is exhibited that the oxygen desorption begins at about 460°C to 603°C. Weight loss of sample decreases rapidly with increasing the temperatures. The LSAF3728 perovskite has weight loss about 1.599%.

The DSC profile shows no endothermic or exothermic peak in the whole heating process, which denotes that no structure transition occurs for the perovskite oxide

All series of dual-phase perovskite membranes after sintered at 1,400°C were analyzed by thermogravimetric analysis (TGA). The perovskite powder was measured under nitrogen gas. The temperature increased from room temperature to 1000°C with heating rate of 20°C min<sup>-1</sup>.

#### 4.3.1.1 The LSAF-BSCF dual-phase perovskite membranes

The weight change for LSAF-BSCF dual-phase powder with varying BSCF5528 contents were executed under N<sub>2</sub> atmosphere. The weight losses for the LSAF-BSCF compounds with ratio 12:1, 12:2, 12:3 and 12:4 by weight are plotted versus temperature shown in Figure 4.25. It is implied that the observed weight change results from the loss of lattice oxygen on heating.

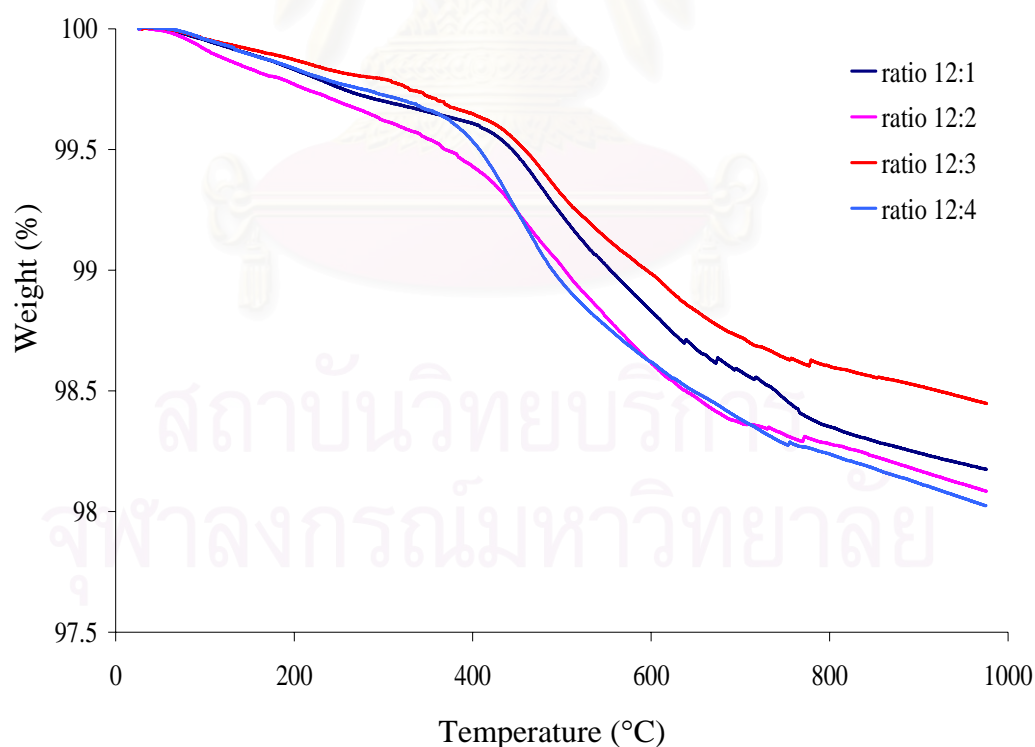


**Figure 4.25** TGA profiles of LSAF-BSCF dual-phase perovskite

From TGA curves, it can be seen that all ratios of LSAF-BSCF have the same weight loss starting around 380°C. Then weight of samples quickly decreased when the temperature increases from 380°C to 800°C.

The percentage weight loss of LSAF-BSCF dual-phase perovskite was presented in table 4.7.

**Table 4.7** TGA data of LSAF-BSCF dual-phase perovskite

Ratio of LSAF:BSCF	Weight loss (%)
12:1	1.413
12:2	1.424
12:3	1.267
12:4	1.619

The TGA data of LSAF-BSCF dual-phase perovskite powder reveals that LSAF-BSCF dual-phase perovskite with ratio 12:4 by weight had the highest weight change as compare to that of the other ratios due to the largest grain size (see section 4.2.2.3 part A) of LSAF-BSCF was comfortably disintegrated by heating temperature condition of TGA. It is noted that the LSAF-BSCF dual phase with ratio 12:4 has the highest oxygen permeation.

#### 4.3.1.2 The LSAF-LSCF dual-phase perovskite membranes

Thermogravimetric analyses of powder LSAF-LSCF dual-phase after sintering was performed under nitrogen atmosphere. The weight changes observed upon heating in N<sub>2</sub> are displayed in Figure 4.26

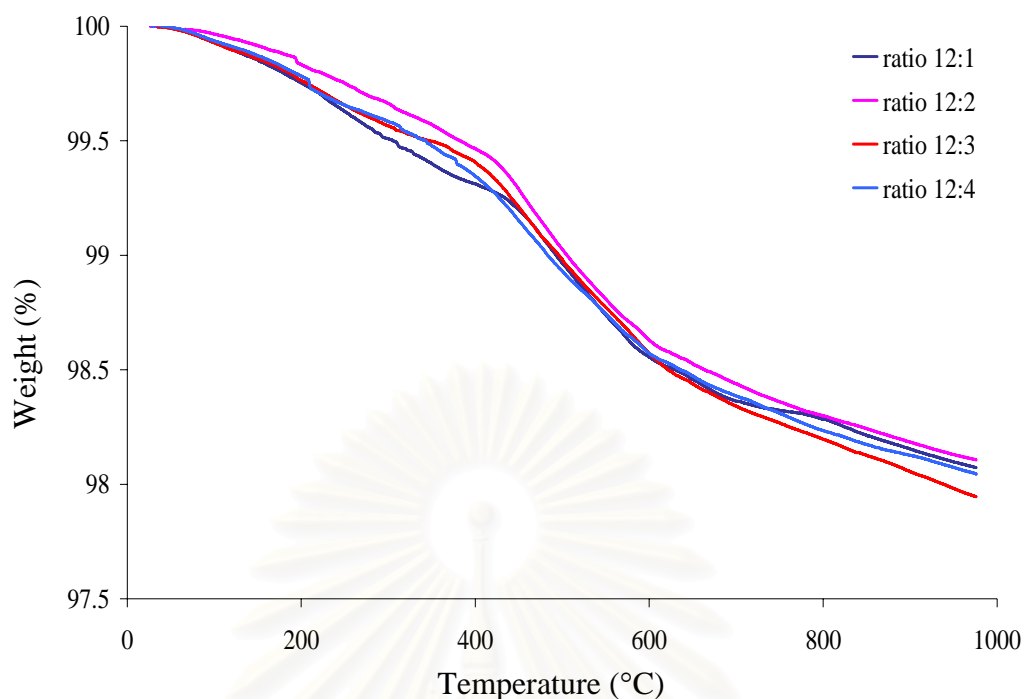


**Figure 4.26** TGA profiles of LSAF-LSCF dual-phase perovskite

The TGA curves demonstrate the loss of oxygen began at temperature in range 380-450°C. All ratios of LSAF-LSCF dual-phase showed that the weight change rapidly decreased at 400-700°C.

The percentage of weight change of LSAF-LSCF samples are listed in Table 4.8.

**Table 4.8** TGA data of LSAF-LSCF dual-phase perovskite

Ratio of LSAF:LSCF	Weight loss (%)
12:1	1.012
12:2	1.192
12:3	1.466
12:4	1.521

From TGA data of LSAF-LSCF dual-phase perovskite, it can be seen that weight change increased with increasing amount of LSCF6482. The result indicated that the LSAF-LSCF membrane with ratio 12:4 had the highest oxygen lattice loss

than those ratios 12:1, 12:2 and 12:3. Because of the weight change of LSAF-LSCF with ratio 12:4 is less than that of pure LSAF3728. Therefore the LSCF6482 perovskite compound did not improve the oxygen permeate property of LSAF3728.

#### 4.3.1.3 The LSAF-LSC dual-phase perovskite membranes

The LSAF-LSC dual-phase perovskite was measured oxygen desorption by thermogravimetric analysis under  $N_2$  atmosphere.

Figure 4.27 shows the relative weight change and temperature for LSAF-LSC dual-phase compounds with various ratios (12:1, 12:2, 12:3 and 12:4 by weight).

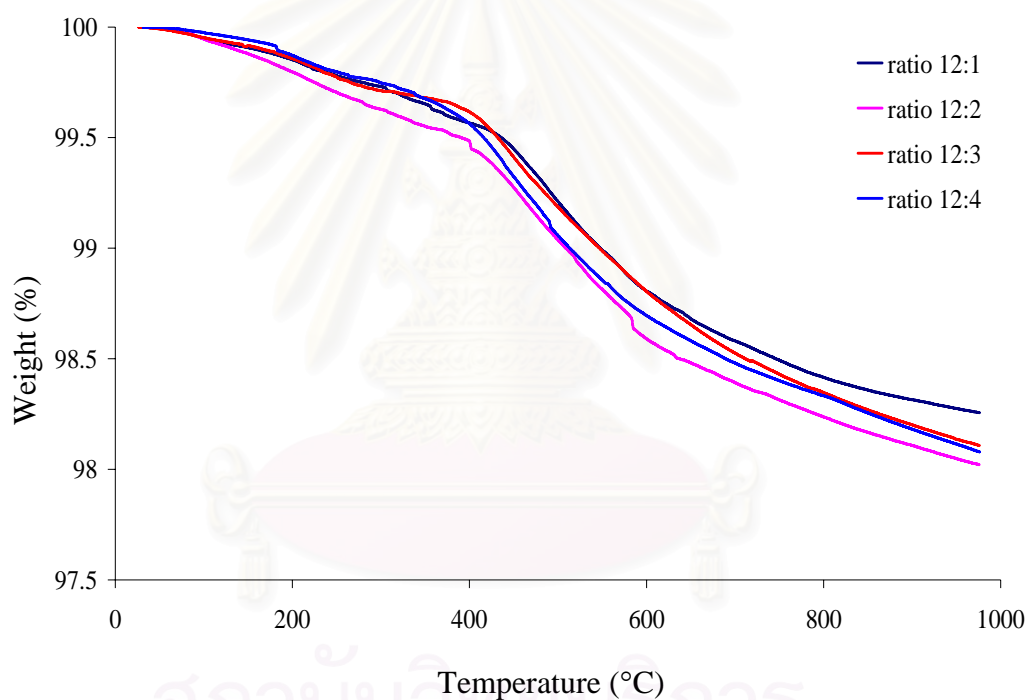


**Figure 4.27** TGA profiles of LSAF-LSC dual-phase perovskite

All ratio of LSAF-LSC dual-phase perovskite exhibited quickly decreased weight loss after heat up from 350°C to 650°C for. The weight change data of LSAF-LSC dual-phase is listed in Table 4.9.

**Table 4.9** TGA data of LSAF-LSC dual-phase perovskite

Ratio of LSAF:LSC	Weight loss (%)
12:1	1.292
12:2	1.543
12:3	1.267
12:4	1.644

The LSAF-LSC dual-phase with ratio 12:4 by weight had the highest percentage weight loss compare to the LSAF-LSC with ratio 12:1, 12:2 12:3 and pure LSAF3728 (1.599%).

The oxygen permeation property correlates with the weight change and oxygen vacancy. Then the dual-phase with ratio 12:4 by weight of LSAF-LSC has the higher oxygen permeation than LSAF-BSCF, LSAF3728 and LSAF-LSCF, respectively.

#### 4.3.2 Temperature-program desorption of oxygen (O<sub>2</sub>-TPD)

In the oxygen temperature program desorption (O<sub>2</sub>-TPD) process, oxygen was exchanged by chemisorption mechanism. The ion participated not only on surface but also inside the perovskite.

Generally, the O<sub>2</sub>-TPD profiles of most perovskites can be characterized by the appearance of  $\alpha$  and  $\beta$  desorption peaks. The  $\alpha$  peak appeared at low temperature (300-600°C) but  $\beta$  peak appeared at high temperature (600-800°C). The peak is due to the oxygen that is accommodated in the oxygen vacancies, while desorption is ascribable to the reduction of B-site cations [45, 46]. In particular its onset and intensity depend in part on the nature of the metal B of the ABO<sub>3</sub> structure, but mainly on the degree of substitution of the A ion with ions of lower valence. When the A ion is partially substituted with an ion of different oxidation state a charge compensation is required so as to achieve electroneutrality. This can either be achieved by formation of oxygen vacancies or by shift of the B metal toward higher valences [47, 48].

The O<sub>2</sub>-TPD profile of LSAF3728 perovskite after sintering at 1,400°C is given in Figure 4.28.

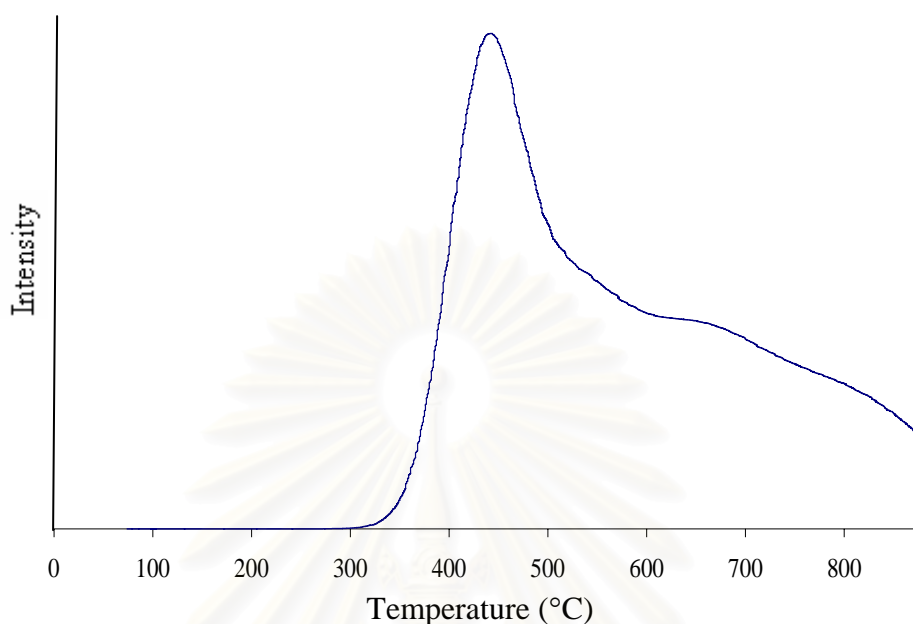


**Figure 4.28** O<sub>2</sub>-TPD profile of pure LSAF3728 perovskite

It shows two kinds of oxygen, sharp peak desorption called  $\alpha$  and broad peak desorption called  $\beta$ -oxygen. The  $\alpha$ -oxygen is the oxygen in atmosphere which desorbed between 200°C and 550°C. The  $\beta$ -oxygen is the oxygen lattice in perovskite structure, they are desorbed between 550°C and 800°C. Commonly, doping Fe at B-site of ABO<sub>3</sub> with aluminum would increase perovskite stability in the oxidation-reduction condition. It means that Al does not affect the redox behaviour of Fe [49]. The amount of oxygen desorption of LSAF is 0.466 and 0.199 mmol/g at low temperature zone (200-550°C) and high temperature zone (550-800°C), respectively.

จุฬาลงกรณ์มหาวิทยาลัย



### 4.3.2.1 The O<sub>2</sub>-TPD of the LSAF-BSCF dual-phase membranes

The O<sub>2</sub>-TPD profiles of LSAF-BSCF dual-phase perovskite with various ratios were shown in Figure 4.29.

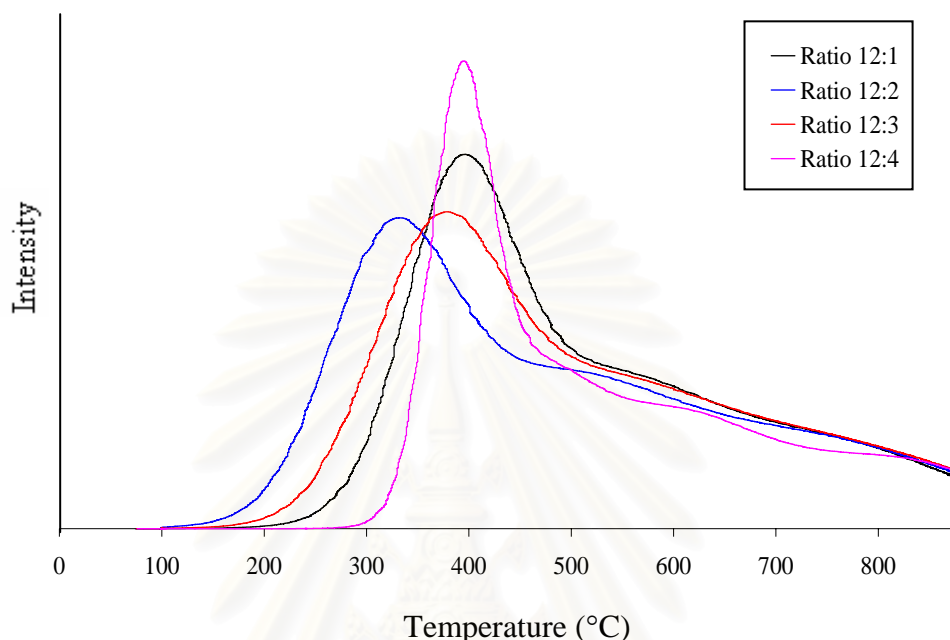


**Figure 4.29** O<sub>2</sub>-TPD profiles of LSAF-BSCF dual-phase with various ratios

Two O<sub>2</sub> desorption peaks are observed for all samples, one between 200°C and 550°C and the other between 550°C and 900°C, similar to the O<sub>2</sub>-TPD profile of pure LSAF3728. It indicated that La<sup>3+</sup> at A site was substituted by Ba<sup>2+</sup>/Sr<sup>2+</sup> from mixing BSCF in dual-phase (confirmed by XRD data), to balance positive charge reduction, the higher oxidation state (Co<sup>4+</sup>/Fe<sup>4+</sup>) at B site was generated from Co<sup>3+</sup>/Fe<sup>3+</sup>. The amount of oxygen desorption of LSAF-BSCF dual-phase with varying BSCF contents were recorded in Table 4.10.

The LSAF-BSCF dual-phase with ratio 12:4 by weight exhibited the highest oxygen desorption at low temperature region while LSAF-BSCF with ratio 12:1 exhibited the highest oxygen desorption at high temperature region. The oxygen desorption at high temperature region barely decreased when BSCF5582 contents were increased.

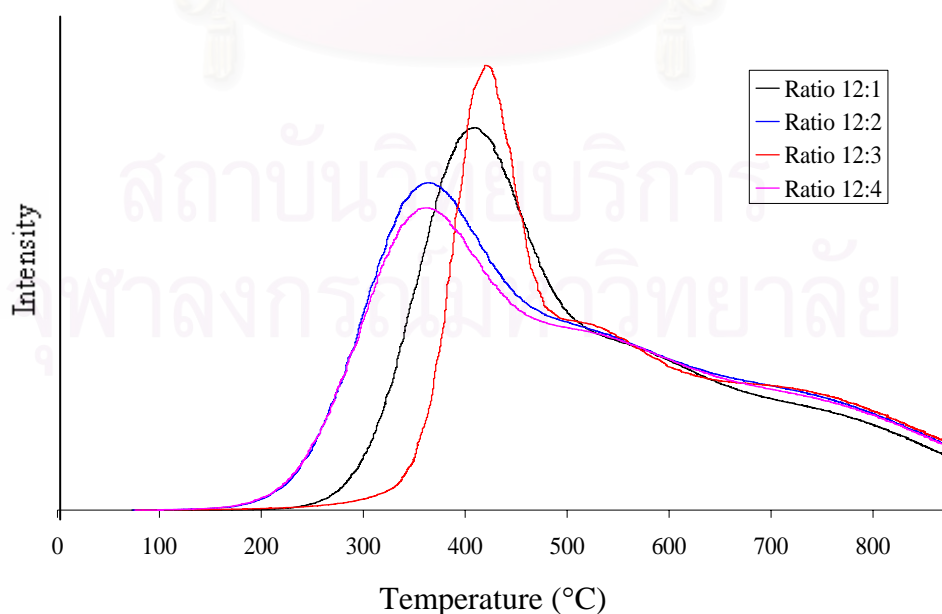
**Table 4.10** Amount of oxygen desorption for LSAF-BSCF dual-phase perovskite

Ratio of LSAF:BSCF	Oxygen (mmol/g)		Total oxygen desorption
	Low temp. zone (200-550°C)	High temp. zone (550-800°C)	
12:1	0.356	0.125	0.481
12:2	0.346	0.115	0.461
12:3	0.355	0.107	0.462
12:4	0.376	0.109	0.485

From Table 4.10, LSAF-BSCF with ratio 12:1 and 12:4 have the higher total oxygen desorption than that of the other ratios. It means that the amount of BSCF does not affect the total oxygen desorption of dual-phase perovskite. LSAF-BSCF (12:1) has the higher oxygen desorption at high temperature than LSAF-BSCF (12:4). It is concluded that LSAF-BSCF (12:1) has the highest total oxygen desorption.

#### 4.3.2.2 The O<sub>2</sub>-TPD of the LSAF-LSCF dual-phase membranes

The O<sub>2</sub>-TPD profiles of the LSAF-LSCF dual-phase with various ratios displayed in Figure 4.30.

**Figure 4.30** O<sub>2</sub>-TPD profiles of LSAF-LSCF dual-phase with various ratios

It can be seen that two prominent characteristic peaks occur on all samples. Desorption peaks are displayed around 200-550°C and 550-800°C, represented as  $\alpha$ -oxygen and  $\beta$ -oxygen respectively.

**Table 4.11** Amount of oxygen desorption for LSAF-LSCF dual-phase perovskite

Ratio of LSAF:LSCF	Oxygen (mmol/g)		Total oxygen desorption
	Low temp. zone (200-550°C)	High temp. zone (550-800°C)	
12:1	0.413	0.259	0.672
12:2	0.445	0.276	0.721
12:3	0.364	0.287	0.651
12:4	0.389	0.278	0.667

Table 4.11 lists amount of oxygen desorption for LSAF-LSCF dual-phase perovskite with various ratios. Amount of oxygen desorption produced by mixing LSCF with LSAF in dual-phase perovskite, seem to be disordered. At high temperature zone, the  $\text{Co}^{3+}$  can be reduced to  $\text{Co}^{2+}$  [47]. Total amount of oxygen desorption of LSAF-LSCF dual-phase with ratio 12:2 has higher value than the other ratios.

#### 4.3.2.3 The $\text{O}_2$ -TPD of the LSAF-LSC dual-phase membranes

The  $\text{O}_2$ -TPD profiles of LSAF-LSC dual-phase perovskite with various ratios were shown in Figure 4.31.

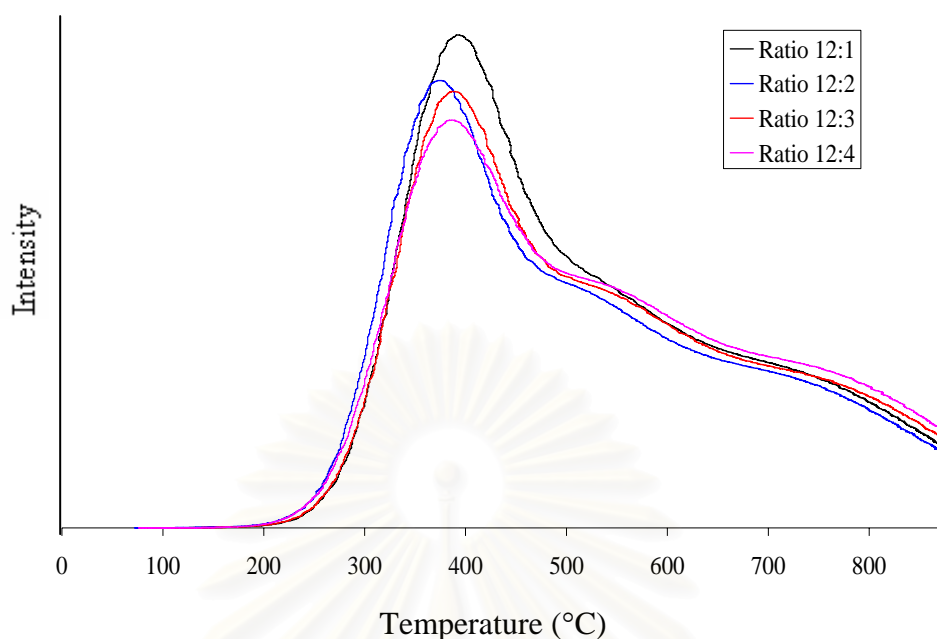


**Figure 4.31** O<sub>2</sub>-TPD profiles of LSAF-LSC dual-phase perovskite with various ratios

From Figure 4.31, the spectra displays desorption peaks at low temperature region about 200-550°C ( $\alpha$ -peak) and high temperature region about 550-800°C ( $\beta$ -peak). At  $\alpha$ -peak, the oxygen from oxygen vacancies is the first to be liberated. Then the oxygen from crystal lattice ( $\beta$ -peak) is liberated between 550-800°C range.

Amount of oxygen desorption for LSAF-LSC dual-phase perovskite with varying LSC contents listed in Table 4.12.

**Table 4.12** Amount of oxygen desorption for LSAF-LSC dual-phase perovskite

Ratio of LSAF:LSC	Oxygen (mmol/g)		Total oxygen desorption
	Low temp. zone (200-550°C)	High temp. zone (550-800°C)	
12:1	0.414	0.262	0.676
12:2	0.419	0.264	0.683
12:3	0.400	0.277	0.677
12:4	0.390	0.291	0.681

Amount of oxygen desorption was decreased with an increasing LSC contents at low temperature zone but decreased at high temperature zone. The LSC contents can suppress  $\text{Co}^{3+}/\text{Fe}^{3+}$  to  $\text{Co}^{4+}/\text{Fe}^{4+}$  at low temperature. At high temperature zone, the  $\text{Co}^{3+}$  can be reduced to  $\text{Co}^{2+}$ . It is significant to acquire a smaller TEC for membrane material. The LSAF-LSC dual-phase with ratio 12:4 by weight had the highest  $\beta$ -oxygen desorption. It could be suggested that LSAF-LSC dual-phase with ratio 12:4 is more stable than those other ratios.

From Table 4.12, LSAF-LSC with ratio 12:2 and 12:4 have the higher total oxygen desorption than that of the other ratios. But LSAF-LSC (12:4) has the higher amount oxygen desorption at high temperature than LSAF-LSC (12:2). It is concluded that LSAF-LSC (12:4) has the highest higher total oxygen desorption.

The  $\text{O}_2$ -TPD results indicated that the LSAF-LSC dual-phase with ratio 12:4 revealed the highest oxygen desorption at high temperature (550-800°C) when compared to the other dual-phases. The oxygen desorption data of dual-phase compared with pure LSAF are listed in Table 4.13.

**Table 4.13** Amount of oxygen desorption of dual-phase perovskites and LSAF3728.

Compound	Oxygen (mmol/g)		Total oxygen desorption
	Low temp. zone (200-550°C)	High temp. zone (550-800°C)	
LSAF3728	0.466	0.199	0.665
LSAF:BSCF ratio 12:1	0.356	0.125	0.481
LSAF:LSCF ratio 12:2	0.445	0.276	0.721
LSAF:LSC ratio 12:4	0.390	0.291	0.681

The amount of oxygen desorption of LSAF3728 at low temperature zone is higher than those of dual-phase perovskites. The LSAF can be used at low temperature. As the LSAF-LSCF dual-phase with ratio 12:2 and LSAF-LSC dual-phase with ratio 12:4 showed high oxygen desorption at high temperature. The LSAF-LSCF (12:2) (0.721 mmol/g) reveals the higher oxygen desorption than

that of LSAF (0.665 mmol/g) in the range of 200-800°C. LSCF and LSC might improve the oxygen desorption property of LSAF at high temperature.

Form Table 4.13, it shows that the total amount of oxygen liberated from composite LSAF-BSCF is less than the pure phase of LSAF. BSCF with higher electronic conductivity could not improve the oxygen desorption of LSAF.



สถาบันวิทยบริการ  
จุฬาลงกรณ์มหาวิทยาลัย

## CHAPTER V

### CONCLUSIONS AND SUGGESTION

#### 5.1 Conclusions

The perovskite-type oxides of  $\text{La}_{0.3}\text{Sr}_{0.7}\text{Al}_{0.2}\text{Fe}_{0.8}\text{O}_{3-\delta}$  (LSAF3728) and  $\text{Ba}_{0.5}\text{Sr}_{0.5}\text{Co}_{0.8}\text{Fe}_{0.2}\text{O}_{3-\delta}$  (BSCF5582) were synthesized by a modified citrate method. In addition,  $\text{La}_{0.6}\text{Sr}_{0.4}\text{Co}_{0.8}\text{Fe}_{0.2}\text{O}_{3-\delta}$  (LSCF6482) and  $\text{La}_{0.6}\text{Sr}_{0.4}\text{CoO}_{3-\delta}$  (LSC64) were synthesized by solid state process. The calcined powder indicated cubic perovskite structure.

The dual-phase perovskite membranes were prepared from the mixture of LSAF3728 with BSCF5582, LSCF6482 and LSC64 or abbreviated as LSAF-BSCF, LSAF-LSCF and LSAF-LSC, respectively, in various ratios 12:1, 12:2, 13:3 and 12:4 by weight. After calcinated at 1,000°C and sintered at 1,400°C, the XRD analysis showed that the LSAF-BSCF, LSAF-LSCF and LSCF-LSC dual-phase perovskites revealed the cubic structure. The trace amount of Fe phase was observed in LSCF-LSC dual-phase. The lattice parameters of these dual-phase membranes are the same as that of pure LSAF3728 except for LSAF-BSCF after sintered at 1,400°C, which exhibited higher the unit cell value than that of pure LSAF3728. The unit cell values of the LSAF-BSCF, LSAF-LSCF and LSCF-LSC dual-phase after calcined and sintered did not signified with varying amounts of BSCF5582, LSCF6428 and LSC64, respectively.

The dual-phase membranes were sintered at setting program temperature shown in Scheme 3.4 (b) to obtain dense ceramic membrane. The morphologies of the dual-phase perovskite membranes were characterized by SEM. The sintering time affected on the grain size of the LSAF-BSCF and LSAF-LSC dual phase membrane. When the sintering time increased, the grain size was slightly increasing. On the contrary, the increasing of sintering time has no effect on the grain size of LSAF-LSCF membrane. The grain size of all series of dual-phase membranes were increased with the increase of sintering temperature. Therefore the dual-phase membranes were sintered at 1,400°C for 6 hours. The varying amounts of BSCF5582, LSCF6428 and LSC64 in dual-phase membranes influenced on the increasing of the

microstructure. It is concluded that the LSAF-BSCF, LSAF-LSCF and LSCF-LSC dual-phase membranes with ratio 12:4 by weight had the largest grain size.

The thermogravimetric analysis (TGA) and temperature program desorption of oxygen ( $O_2$ -TPD), indicated the amount oxygen desorption of dual-phase perovskite at high temperature. The TGA results showed that the weight loss of oxygen of dual-phase perovskite with ratio 12:4 by weight was higher than that of other ratios of each series. The experiment data of  $O_2$ -TPD demonstrated that the total oxygen desorption of LSCF-LSCF with ratio 12:2 and LSCF-LSC with ratio 12:4 was larger than that of pure LSAF3728 and LSAF-BSCF with ratio 12:1, respectively. The LSCF-LSCF dual-phase with ratio 12:2 by weight had the highest oxygen desorption property. It concluded that BSCF (dominant electron conductivity) can not modified the oxygen desorption of LSAF. As the LSCF with higher electronic conductivity and LSC (dominant oxygen ion conductivity) can improved the oxygen desorption of LSAF. Therefore, the oxygen permeation flux of LSAF could be increased by mixing LSAF with LSCF and LSC.

## 5.2 Suggestions

From experiment results, future work should be focused on the following:

1. To measure oxygen permeation flux of dual-phase perovskite membranes by using membrane reactor.
2. To test thermal expansion coefficient (TEC) of dual-phase perovskite by dilatometer technique for fuel cell application.
3. To measure the electronic conductivity of the dual-phase membranes by using impedance method.



## REFERENCES

1. Paul, N.; Robin, E.; Steven, L.; Dale, M. Iron Transport Membrane Technology for Oxygen Separation and Syngas Production. *Solid State Ionics*, **2000**, *134*, 21-33.
2. Wanqon, J.; Shiguang, L.; Pei, H.; Nanping, X.; Jun, S.; Lin, Y. S. Tubular Lanthanum Cobaltite Perovskite-type Membrane Reactors for Partial Oxidation of methane to Syngas. *Journal of Membrane Science*, **2000**, *166*, 13-22.
3. Hendriksen, P. V.; Larsen, P. H.; Mogensen, M.; Poulsen, F. W.; Wiik, K. Prospects and Problems of Dense Oxygen Permeable Membranes. *Catalysis Today*, **2000**, *56*, 283-295.
4. Argonne, I. L. Material Scientists at Argonne National Laboratory Chemical Engineering Progress, 1995, 11-14.
5. Teraoka, Y.; Nobunaga, T.; Okamoto, K.; Miura, N.; Yamazoe, N. Influence of Constituent Metal Cations in Substituted  $\text{LaCoO}_3$  on Mixed Conductivity and Oxygen Permeability. *Solid State Ionics*, **1991**, *48*, 207-212.
6. Ishihara, T.; Arikawa, H.; Akbay, T.; Nishiguchi, H.; Takita, Y. Nonstoichiometric  $\text{La}_{2-x}\text{GeO}_{5-\delta}$  Monoclinic Oxide as a New Fast Oxide Ion Conductor. *Journal of the American Chemical Society*, 2001, *123*, 203-209.
7. Bouwmeester, H. J. M.; McIntosh, S. Mixed Ionic-electronic Conducting Perovskites. *Solid State Electrochemistry*, **2005**, 1-14.
8. Zeng, Y.; Lin, Y. S.; Swartz, S. L. Perovskite-type Ceramic Membrane: Synthesis, Oxygen Permeation and Membrane Reactor Performance for Oxidative Coupling of Methane. *Journal of Membrane Science*, **1998**, *150*, 87-98.
9. Bhatta, D. H.; Vedula, R.; Desua, B. S.; Fralick, C. G.  $\text{La}_{1-x}\text{Sr}_x\text{CoO}_3$  for Thin Film Thermocouple Applications. *Thin Solid Films*, **1999**, *350*, 249-257.

10. Petrov, N. A.; Kononchuk, F. O.; Andreev, V. A.; Cherepanov, A. V.; Kofstad, P. Crystal Structure, Electrical and Magnetic Properties of  $\text{La}_{1-x}\text{Sr}_x\text{CoO}_{3-y}$ . *Solid State Ionics*, **1995**, *80*, 189-199.
11. Anthony, P.; Peng, H.; Frank, T. Evaluation of La–Sr–Co–Fe–O Perovskites for Solid Oxide Fuel Cells and Gas Separation Membranes. *Solid State Ionics*, **2000**, *135*, 719-725.
12. Lee, S.; Lee, K. S.; Woo, S. K.; Kim, J. W.; Ishihara, T.; Kim, D. K. Oxygen-Permeation Property of  $\text{LaSrBFeO}_3$  (B=Co, Ga) Perovskite Membrane Surface-Modified by  $\text{LaSrCoO}_3$ . *Solid State Ionics*, **2003**, *158*, 287-296.
13. Ten Elshof, J. E.; Bouwmeester, H.J.M.; Verweij, H. Oxidative Coupling of Methane in a Mixed-conducting Perovskite Membrane Reactor. *Applied Catalysis A: General*, **1995**, *130*, 195-212.
14. Lane, J. A.; Benson, S. J.; Waller, D.; Kilner, J. A. Oxygen Transport in  $\text{La}_{0.6}\text{Sr}_{0.4}\text{Co}_{0.2}\text{Fe}_{0.8}\text{O}_{3-\delta}$ . *Solid State Ionics*, **1999**, *121*, 201-208.
15. Ullmann, H.; Trofimenkoa, N.; Tietzb, F.; Stöverb D.; Ahmad-Khanloub, A. Correlation between Thermal Expansion and Oxide Ion Transport in Mixed Conducting Perovskite-type Oxides for SOFC Cathodes. *Solid State Ionics*, **2000**, *138*, 79-90.
16. Xu, Q.; Huang, D. P.; Chen, W.; Lee, J. H.; Kim, B. H.; Wang, H.; Yuan, R. Z. Influence of Sintering Temperature on Microstructure and Mixed Electronic-ionic Conduction Properties of Perovskite-Type  $\text{La}_{0.6}\text{Sr}_{0.4}\text{Co}_{0.8}\text{Fe}_{0.2}\text{O}_{3-\delta}$  Ceramics. *Ceramics International*, **2004**, *30*, 429-433.
17. Shao, Z.; Xiong, G.; Tong, J.; Dong, H.; Yang, W. Ba Effect in Doped  $\text{Sr}(\text{Co}_{0.8}\text{Fe}_{0.2})\text{O}_{3-\delta}$  on the Phase Structure and Oxygen Permeation Properties of the Dense Ceramic Membranes. *Separation and Purification Technology*, **2001**, *25*, 419-429.
18. Shao, Z.; Yang, W.; Cong, Y.; Dong, H.; Tong, J.; Xiong, G. Investigation of the Permeation Behavior and Stability of a  $\text{Ba}_{0.5}\text{Sr}_{0.5}\text{Co}_{0.8}\text{Fe}_{0.2}\text{O}_{3-\delta}$  Oxygen Membrane. *Journal of Membrane Science*, **2000**, *172*, 177-188.
19. Shao, Z.; Dong, H.; Xiong, G.; Cong, Y.; Yang, W. Performance of a Mixed-conducting Ceramic Membrane Reactor with High Oxygen Permeability for Methane Conversion. *Journal of Membrane Science*, **2001**, *183*, 181-192.

20. Wang, H.; Yang, W. S.; Conga, Y.; Zhua, X.; Lin S.Y. Structure and Oxygen Permeability of a Dual-Phase Membrane. *Journal of Membrane Science*, **2003**, *224*, 107-115.
21. Mazanec, T. J.; Cable, T. L.; Frye, J. G. Electrocatalytic Cells for Chemical Reaction. *Solid State Ionics*, **1992**, *53-56*, 111-118.
22. Kim, J.; Lin, Y.S. Synthesis and Oxygen Permeation Properties of Ceramic-Metal Dual-phase Membranes. *Journal of Membrane Science*, **2000**, *167*, 123-133.
23. Kharton, V. V.; Kovalevsky, V. A.; Viskup, P. A.; Figueiredo, M. F.; Yaremchenko, A. A.; Naumovich, N. E.; Marques, F. M. B. Oxygen Permeability  $\text{Ce}_{0.8}\text{Gd}_{0.2}\text{O}_{2-\delta}$ - $\text{La}_{0.7}\text{Sr}_{0.3}\text{MnO}_{3-\delta}$  Composite Membranes. *Journal of Electrochemical Society*, **2000**, *147*, 2814-2821.
24. Shaulaa, A. L.; Khartona, V. V.; Marquesa, F.M.B. Phase Interaction and Oxygen Transport in  $\text{La}_{0.8}\text{Sr}_{0.2}\text{Fe}_{0.8}\text{Co}_{0.2}\text{O}_3$ - $(\text{La}_{0.9}\text{Sr}_{0.1})_{0.98}\text{Ga}_{0.8}\text{Mg}_{0.2}\text{O}_3$  Composites. *Journal of the European Ceramic Society*, **2004**, *24*, 2631-2639.
25. Wang, H.; Yang, S. W.; Conga Y.; Zhua, X.; Lin S. Y. Structure and Oxygen Permeability of a Dual-phase Membrane. *Journal of Membrane Science*, **2003**, *224*, 107-115
26. Ishihara, T.; Yamada, T.; Arikawa, H.; Nishiguchi, H.; Takita, Y. Mixed Electronic-oxide Ionic Conductivity and Oxygen Permeating Property of Fe-, Co- or Ni-doped  $\text{LaGaO}_3$  Perovskite Oxide. *Solid State Ionics*, **2002**, *135*, 631-636.
27. Ishihara, T.; Tsuruta, Y.; Todaka, T.; Nishiguchi, H.; Takita, Y. Fe Doped  $\text{LaGaO}_3$  Perovskite Oxide as an Oxygen Separating Membrane for  $\text{CH}_4$  Partial Oxidation. *Solid State Ionics*, **2000**, *152-153*, 709-714.
28. Yaremchenko, A.; Patrakev, M.; Kharton, V.; Marques, F., Oxygen Ionic and Electronic Conductivity of  $\text{La}_{0.3}\text{Sr}_{0.7}\text{Fe}(\text{Al})\text{O}_{3-\delta}$  Perovskites. *Solid State Ionics*, **2004**, *6*, 357-366.
29. Li, C.; Sohb, K. C. K.; Wu, P. Formability of  $\text{ABO}_3$  Perovskites. *Journal of Alloys and Compounds*, **2004**, *372*, 40-48.

30. Hayashi, H.; Inaba, H., Matsuyama, M.; Lan, N. G.; Dokiya, M.; Tagawa, H. Structural Consideration on the Ionic Conductivity of Perovskite-type Oxides. *Solid State Ionics*, **1999**, *122*, 1-15.
31. Peña, M. A.; Fierro, J. L. G. Chemical Structures and Performance of Perovskite Oxides. *Chemical Reviews*, **2001**, *101*, 1981-2017.
32. Rao, C. N. R.; Gopalakrishnan, J.; Vidyasagar, K. Superstructure, Ordered Defects and Nonstoichiometry in Metal Oxides of Perovskite and Related Structure. *Indian Journal of Chemistry*, **1984**, *23A*, 265-284.
33. Teraoka, Y.; Nobunaga, T.; and Yamazoe, N. Effect of Cation Substitution on the Oxygen Semipermeability of Perovskite-type Oxide. *Chemistry Letters*, **1988**, 503-506.
34. Wu, K.; Xie, S.; Jiang, G.S.; Liu, W.; Chen C.S. Oxygen Permeation through  $(\text{Bi}_2\text{O}_3)_{0.74}(\text{SrO})_{0.26}\text{-Ag}$  (40% v/o) Composite. *Journal of Membrane Science*, **2001**, *188*, 189-193.
35. Henny J. M. B. Dense Ceramic Membranes for Methane Conversion. *Catalysis Today*, 2003, *82*, 141-150.
36. Teraoka, Y.; Zhang, H. M.; Furukawa, S.; Yamazoe, N. Oxygen Permeation through Perovskite-type Oxide. *Chemistry Letters*, **1985**, 1743-1746
37. Mizusaki, J. Nonstoichiometry, Diffusion, and Electrochemical Properties of Perovskite-type Oxide Electrode Materials. *Solid State Ionics*, **1992**, *52*, 79-91.
38. Cui, X.; Liu, Y. New Methods to Prepare Ultrafine Particles of some Perovskite-type Oxides *Chemical Engineering Journal*, **2000**, *78*, 205-209.
39. Pechini, M. Method of Preparing Lead and Alkaline-earth Titanates and Niobates and Coating Method Using the Same to Form a Capacitor, **U.S Patent, 1976**.
40. Blank, D. H. A.; Kruidhof, H.; Flokstra, J. Preparation of  $\text{YBa}_2\text{Cu}_3\text{O}_{7-\delta}$  by Citrate Synthesis and Pyrolysis. *Journal of Physics. D: Applied Physics*, **1988**, *21*, 226-227.
41. Richerson, D. W. Modern Ceramic Engineering, Properties, Processing, and Use in Design, 2<sup>nd</sup> ed., New York, Marcel Dekker, Inc., p378-381, **1992**.

42. Supawan, T.; Jinda, Y.; Jidong, L.; YiHua, M. Synthesis and Characterization of Sr and Fe Substituted LaGaO<sub>3</sub> Perovskites and Membranes. *Separation and Purification Technology*, **2003**, *32*, 319-326.
43. Zeng, Y.; Lin, Y. S. A Transient TGA Study on Oxygen Permeation Properties of Perovskite-type Ceramic Membrane. *Solid State Ionics* **1998**, *110*, 209-221.
44. Hu, J.; Hu, X.; Hao, H.; Guo, L.; Song, H.; Yang, D. A Transient Thermogravimetric Study on the Oxygen Permeation at High Temperature of the Superconducting material YBa<sub>2</sub>Cu<sub>3</sub>O<sub>7-δ</sub>. *Solid State Ionics*, **2005**, *176*, 487-494.
45. Dai, X. H.; Ng, F. C.; Au, T. C. The Catalytic Performance and Characterization of a Durable Perovskite-type Chloro-Oxide SrFeO<sub>3-δ</sub>Cl<sub>σ</sub> Catalyst Selective for the Oxidative Dehydrogenation of Ethane. *Catalysis Letters*, **1999**, *57*, 115-120.
46. Tong, J.; Yang, W.; Zhu, B.; Cai, R. Investigation of Ideal Zirconium-Doped Perovskite-type Ceramic Membrane Materials for Oxygen Separation. *Journal of Membrane Science*, **2002**, *203*, 175-189.
47. Tong, J.; Yang, W.; Cai, R.; Zhu, B.; Xiong, G. Investigation on the Structure Stability and Oxygen Permeability of Titanium-Doped Perovskite-type Oxide of BaTi<sub>0.2</sub>Co<sub>x</sub>Fe<sub>0.8-x</sub>O<sub>3-δ</sub> (x = 0.2-0.6). *Separation and Purification Technology*, **2003**, *32*, 289-299.
48. Jaroslav, C.; David, D.; Jaroslav, C. J.; Antonin, B.; Jan, V. Synthesis, Structure and Oxygen Thermally Programmed Desorption Spectra of La<sub>1-x</sub>Ca<sub>x</sub>Al<sub>y</sub>Fe<sub>1-y</sub>O<sub>3-δ</sub> Perovskites. *Journal of the European Ceramic Society*, **2006**.
49. Chen, T. Y.; Fung, K. Z. A and B-Site Substitution of the Solid Electrolyte LaGaO<sub>3</sub> and LaAlO<sub>3</sub> with the Alkaline-Earth Oxides MgO and SrO. *Journal of Alloys and compounds*, **2004**, *368*, 106-115.

## APPENDIX

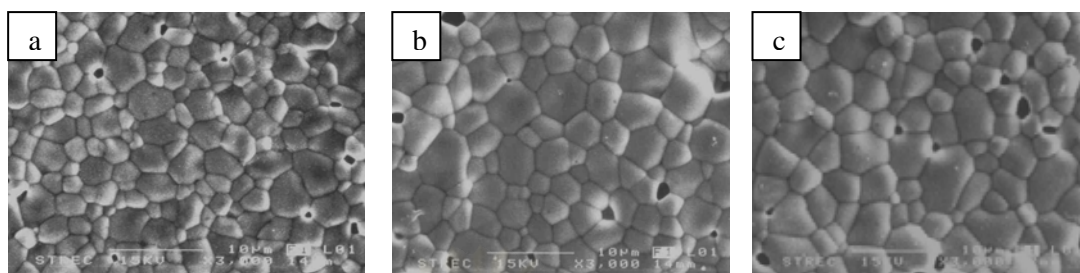


**Figure A-1** SEM pictures of LSAF-BSCF with ratio (a) 12:2, (b) 12:3 and (c) 12:4 after sintered at 1,300°C, 12 hr.

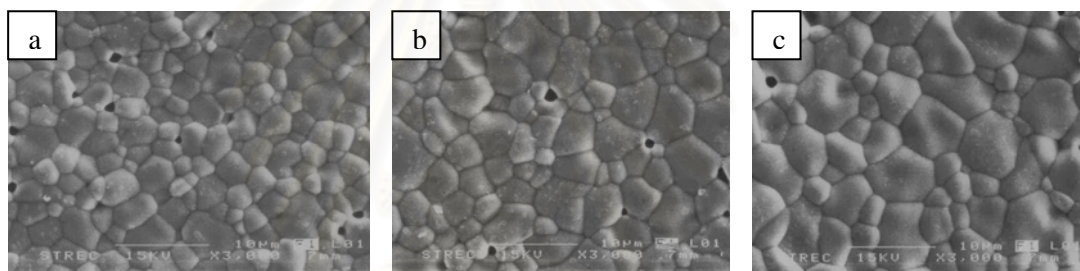


**Figure A-2** SEM pictures of LSAF-BSCF with ratio (a) 12:2, (b) 12:3 and (c) 12:4 after sintered at 1,300°C, 18 hr.

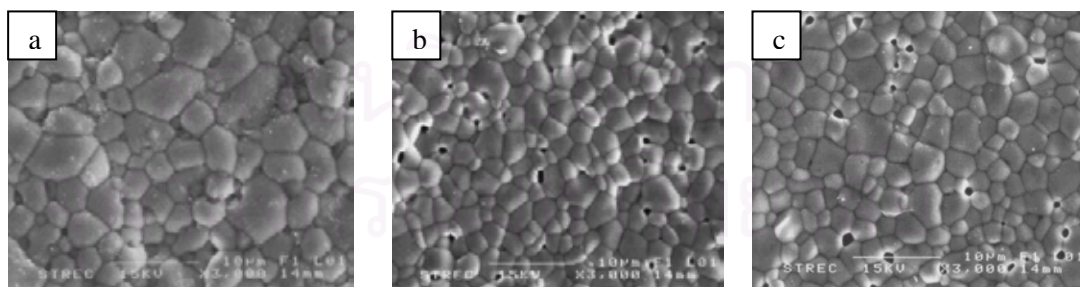


**Figure A-3** SEM pictures of LSAF-LSCF with ratio (a) 12:2, (b) 12:3 and (c) 12:4 after sintered at 1,300°C, 12 hr.

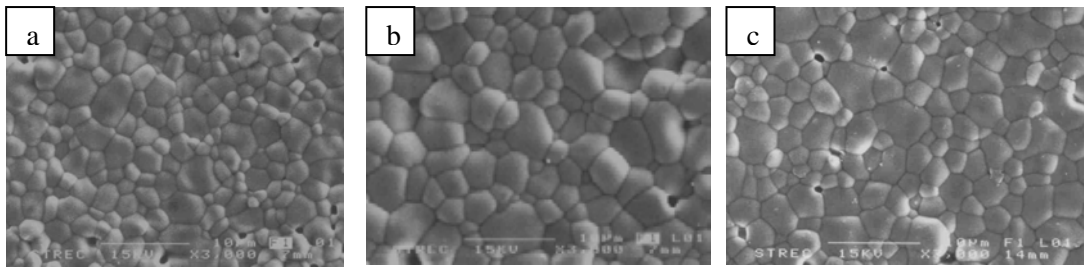


**Figure A-4** SEM pictures of LSAF-LSCF with ratio (a) 12:2, (b) 12:3 and (c) 12:4 after sintered at 1,300°C, 18 hr.

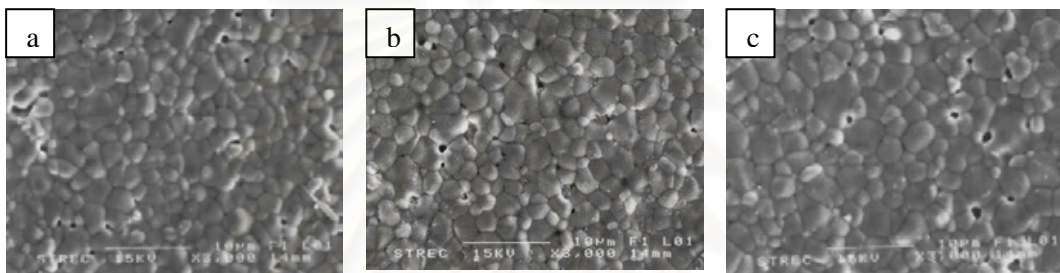


**Figure A-5** SEM pictures of LSAF-LSC with ratio (a) 12:2, (b) 12:3 and (c) 12:4 after sintered at 1,300°C, 12 hr.

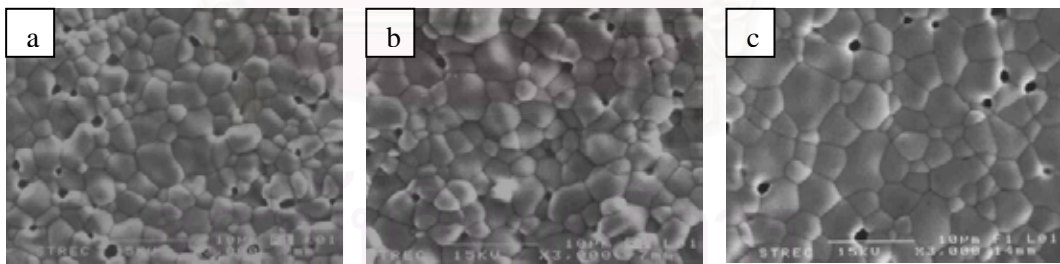


**Figure A-5** SEM pictures of LSAF-LSC with ratio (a) 12:2, (b) 12:3 and (c) 12:4 after sintered at 1,300°C, 18 hr.

## VITAE

Miss Itsarawadee Thipdaung was born on November 15, 1981 in Nakhonsithammarat, Thailand. She received B.Sc. Degree of in Chemistry at Mahidol University in 2004. Since then, she has been a graduate student studying in Program of Petrochemistry and Polymer Science at Faculty of Science, Chulalongkorn University.

Her present address in 98 Moo 6, Parknakorn, Muang, Nakhonsithammarat, 80000, Thailand. Tel 06-5138935, 075-379175.



สถาบันวิทยบริการ  
จุฬาลงกรณ์มหาวิทยาลัย